Understanding the crystallization of solution sheared metal-organic frameworks (MOFs) thin film

---

A Ph. D. Dissertation Presented to

The Faculty of the Department of Chemical Engineering

University of Virginia

In Partial Fulfillment
of the Requirements for the Degree
Doctor of Philosophy

By

Sangeun Jung

2022

APPROVAL SHEET

This Dissertation is submitted in partial fulfillment of the requirements for the degree of:

Doctor of Philosophy

Authored by:

Sangeun Jung

This Dissertation has been read and approved by the examining committee:

Gaurav Giri, PhD
Advisor

Joshua Choi, PhD
Committee Member

William Epling, PhD
Committee Member

Prasanna Balachandran, PhD
Committee Member

Rachel Letteri, PhD
Committee Member

Accepted for the School of Engineering and Applied Science:

Jennifer L. West, School of Engineering and Applied Science
May 2022

ABSTRACT

Metal-organic frameworks (MOFs) have emerged in the scientific community as a promising candidate in research interest due to their remarkable tunability and structural diversity as well as ultrahigh porosity. MOFs are highly-ordered porous crystalline materials that are formed via coordination bonding between metal ions or secondary building units (SBUs) as nodes and multitopic organic ligands as linkers. These characteristics enable MOFs for a wide range of applications such as sensor, gas separation and storage, membrane, and catalysis. To utilize MOFs in these applications, MOFs should be grown as thin films or membranes. Thin films can lower the mass transfer resistances, and the porous nature of MOF can increase its selective performance.

Among various thin film fabrication techniques, solution shearing is used to fabricate MOF thin films. Conventional MOF fabrication techniques, including solvothermal growth or layer-by-layer (LbL) growth, provide high-quality thin films, but they suffer from slow crystallization kinetics. On the other hand, solution shearing that belongs in the same class of the meniscus-guided coating techniques has been studied as a versatile as well as a concise approach that enables to fabricate thin film rapidly and control film thickness, crystal orientation, and film coverage. Therefore, this dissertation focuses on fabricating different types of MOF thin films and infiltrating guest molecules into their pores using solution shearing to observe the thin film property changes from the pristine MOF thin films.

In Chapter 2, solution shearing is used to fabricate a large area, continuous and insulating Cu(II)-based MOF, called HKUST-1, thin film. However, it is hard to synthesize a large area and continuous HKUST-1 thin film using solution shearing. Therefore, we found out that repeating solution shearing cycles enhance the film coverage. The initial solution shearing cycle is used to deposit HKUST-1 crystals, and the secondary crystallization may occur in the subsequent solution

shearing cycles on the substrate. The film coverage of the large-area and continuous HKUST-1 thin film is confirmed by incorporating a redox-active molecule, called 7,7,8,8-Tetracyanoquinodimethane (TCNQ). Upon TCNQ infiltration, the electrical conductivity of the thin film increases seven orders of magnitude electrical conductivity than the pristine HKUST-1. Furthermore, the active learning approach is applied in solution shearing parameters to find an optimized parameter that provides the thinnest fully covered HKUST-1 thin film. In this chapter, the solution shearing technique shows its feasibility that can be used as a large area and continuous MOF thin film.

Chapter 3 highlights that the zirconium 1,4-dicarboxybenzene MOF, UiO-66, can be fabricated using evaporative crystallization during solution shearing. Solution shearing parameters (type of solvent, coating speed, substrate temperature, and concentration of the precursor solution) are varied to observe the changes in the film thickness, coverage, and crystallinity. In addition, the oriented crystal structure of UiO-66 thin film is grown when dimethylformamide (DMF) is used as a solvent. Last, solution-sheared UiO-66 thin film is fabricated on the porous substrate (anodic alumina oxide, known as AAO) to use the thin film for separation applications. To the best of our knowledge, this is the first time that UiO-66 crystals are formed via solution shearing.

In Chapter 4, based upon what we have found in Chapter 3, the pores of UiO-66 are incorporated by polymer molecules. The polymer and the MOF composite, called polyMOF, are synthesized. In this study, the thin film composite of piezoelectric polymer, known as poly(vinyl difluoride) (PVDF), and UiO-66 is fabricated via solution shearing. Unlike the conventional polyMOF thin film fabrication process, the precursor solution that contains node, linker, and polymer is deposited as a thin film using solution shearing. By using the concept of secondary crystallization, a large area, continuous and freestanding thin film of PVDF@UiO-66 is fabricated

within a minute. Due to the addition of PVDF, the film coverage reaches up to 100% under the resolution of SEM, and its addition inside the UiO-66 pores is confirmed by observing the changes in piezoelectric performance. This is the first instance that shows the fabrication of polyMOF thin film using solution shearing. This dissertation provides the feasibility towards expanding the application of solution shearing in the MOF thin film field.

ACKNOWLEDGEMENTS

At first, I would like to thank my advisor, Professor Gaurav Giri. When I decided to join to UVA, his passion and vision for research are truly inspired. These last throughout my studies. Assigning him as my advisor in the graduate school is one of the best decisions that I have ever made in my life.

I would also appreciate my dissertation committees input on this dissertation. Thank Professor Joshua Choi, Professor William Epling, Professor Prasanna Balachandran, and Professor Rachel Letteri. Your feedback and advise were invaluable for my development as a researcher.

Thank you to my best Giri Group members, Dr. Arian Ghorbanpour, Dr. Stephanie Guthrie, Dr. Luke Huelsenbeck, Ashley Conley, Natalie Smith, Prince Verma, Ankit Dhakal, and Meagon Phister. When I had hard time on my research and my life in general, your support and advise helped me to be on the right track. What an incredible and fantastic group of people to work with. The time that we spent together will be unforgettable. Our group members are the key of success and let me realize how important the teamwork is. Last, special thanks to two of the greatest people in my life, Dr. Luke Huelsenbeck and Ashley Conley. You are my mentors, and I highly appreciate your guidance again. If I have not met you, I am not sure whether I can complete this degree or not.

Also, my undergraduates who helped me to complete this work. Emily Beyer, Sean Robinson, and Madison Stone. Watching all of you develop as researchers was such a pleasure. Congratulation to Emily Beyer, who accepted MIT graduate school program. I appreciate Sean Robinson and Madison Stone's input on this. Sean Robinson, I could not publish many papers if I have not met you.

Thank you to Professor Detlef Smilgies, and Dr. Kevin Stone for teaching me so much about synchrotron-based studies and the knowledge. Furthermore, many of these works are based on collaborations. A special thanks to Hongxi Luo for many inquisitive and insightful discussions. Even though we have not met together after the pandemic, I always remember your support and kindness. To Dr. Ning-Jiun Jan for valuable feedback and advice on image analysis. To Roberto Herrara del Valle and Professor Prasanna Balachandran for the optimization work on HKUST-1 Machine Learning. To Dr. Mallory DeCoster, and Professor Patrick Hopkins for the TCNQ, H_4-TCNQ, and F_4-TCNQ impregnation inside the HKUST-1 thin film. To Yongmin Baek and Professor Kyusang Lee for the polymer incorporation work into the UiO-66 thin film.

To ROK officers, “K”-friends and “A”-friends, the many smiles and warmth were much appreciated. Special thanks to the Colonel Kim, another Colonel Kim, Mr. Yoon, Mr. Choi, Ms. Choi, and Mr. Seo for many mental supports in my life. Every once when I feel homesick and have hard time, talking with you helped me out to relieve stress.

Thank you to my lovely family. I am forever grateful for the unconditional love and support given to me by my parents, Jung and Lee, and my American parents, Scott and Ronda. Ever since when I was 16 years old, I left alone in the U.S. Living in totally different culture was really hard. Even though my parents were also scared about the decision, they have always encouraged and not being afraid of the unknown. In addition, they gave up so many things that they want to do. From now on, I would like to give this back. Also, if Scott and Ronda Andersen did not take care of me in high school, I could not be here. And thank you to my only one brother, Taewoo, I cannot express enough gratitude for your support and love. I always feel sorry not to be with you ever since I moved to U.S. However, I always love you wherever I am at, and whenever it is. Last, I

would like to say thank you to my special one, Lily, who is so gorgeous, beautiful and smart woman. Your advice, support and smile are the greatest energy of my life.

At the end, I always feel how lucky I am. All people who I met affect to make decision in my life. Since I got so much support from them, I would also live rest of my life by helping others and being humble.

민들레가 어디서든 잘 자랄 수 있는 건
어디로 데려갈지 모르는 바람에
기꺼이 몸을 실을 수 있는
용기를 가졌지 때문이겠지

어디서든 예쁜 민들레를 피워낼 수 있는 건
좋은 땅에 닿을 거라는 희망을 품었고
바람에서의 여행도 즐길 수 있는
긍정을 가졌기 때문일거야

아직 작은 씨앗이기에
그리 조급해하지 않아도 괜찮아
그리 불안해하지 않아도 괜찮아

넌 머지않아 예쁜 꽃이 될 테니까

-박치성, 봄이에게

TABLE OF CONTENTS

Page

LIST OF TABLES

LIST OF FIGURES

abundance of Si seen in the region with a crack on the lower left of the image. This corresponds that HKUST-1 thin film is completely covered via multiple cycles of solution shearing. The dark spot in **C** and **D** occurs due to the rough film thickness which EDS detector cannot detect elements on the film.

Figure A2. 4. Due to the multiple solution shearing processes, HKUST-1 crystal shares their crystal plane with neighbor crystals as indicated by the red circles.

Figure A2. 5. The XRD peak comparison between solution sheared HKUST-1 and solvothermal HKUST-1. Solution sheared peaks match closely with the solvothermal HKUST-1.

Figure A2. 6. (A) – (B) SEM images of thermally activated 72 hrs and 168 hrs of TCNQ@HKUST-1. Numerous nanowire crystals appear on the surface of the HKUST-1 thin film after the substrate is soaked in TCNQ solution for 72 hours. These molecules represent the formation of the Cu(TCNQ) as a side product.

Figure A2. 7. The SEM image of the fully covered HKUST-1 film that the parameters were provided using active learning.

Figure 3. 1. (a) Conceptual diagram of solution shearing. The metal-oxo cluster and linker are present in the solution, and as the solvent evaporates a solid film of zirconium 1,4-dicarboxybenzene MOF (UiO-66) is grown on the substrate (gray area). (b) Chemical components of UiO-66. (c) The rectangular plot showing the operational range of each solution shearing parameter covered in this study.

Figure 3. 2. Influence of temperature on zirconium 1,4-dicarboxybenzene MOF (UiO-66) film synthesis. (a) Adjusted thickness as a function of temperature shows increasing thickness. (b) Grazing incidence wide-angle x-ray scattering patterns of the film synthesized at 100 ºC, 130 ºC, and 160 ºC. Films created using higher temperatures show higher diffraction intensities from the (111) plane. (c) – (e) Two-dimensional grazing incidence wide-angle x-ray scattering patterns used to obtain Figure 2(b). (f) – (h) Scanning electron microscope images of the film synthesized at (f) 100 ºC, (g) 130 ºC, and (h) 160 ºC. Scale bar is 20 microns. (i) – (k) Scanning electron microscope images of the film synthesized at (f) 100 ºC, (g) 130 ºC, and (h) 160 ºC. Scale bar is 2 microns. Other conditions: Dimethyl sulfoxide, 36.6% (v/v) acetic acid, 70 mM precursor concentration, 0.1 mm/s blade speed.

Figure 3. 3. Influence of blade speed on zirconium 1,4-dicarboxybenzene MOF (UiO-66) film synthesis. (a) Adjusted thickness as a function of speed shows decreasing thickness with increasing speed. (b) Integrated grazing incidence wide-angle x-ray scattering patterns of the film synthesized at 0.1 and 0.4 mm/s. Films created using higher speeds show lower diffraction intensities. (c) – (d) Two-dimensional grazing incidence wide-angle x-ray scattering patterns used to obtain Figure 3(b). (e) – (f) Scanning electron microscope images of the film synthesized at (e) 0.4 mm/s, and (f) 0.1 mm/s. Scale bar is 20 microns. (g) – (h) Scanning electron microscope images of the film synthesized at (g) 0.4 mm/s, and (h) 0.1 mm/s. Scale bar is 2 microns. Other conditions: Dimethyl sulfoxide, 36.6% (v/v) acetic acid, 70 mM precursor concentration, 130 ºC temperature.

Figure 3. 4. Influence of zirconium ion and linker concentration on zirconium 1,4-dicarboxybenzene MOF (UiO-66) film synthesis. (a) Adjusted thickness as a function of concentration shows increasing thickness. (b) Integrated grazing incidence wide-angle x-ray scattering patterns of the film synthesized at 39.2 mM and 70 mM zirconium ion concentration, with the linker concentration held stoichiometrically constant. (c) – (d) Two-dimensional grazing incidence wide-angle x-ray scattering patterns used to obtain Figure 4(b). (e) – (f) Scanning electron microscope images of the film synthesized at (e) 39.2 mM and (f) 70 mM. Scale bar is 20 microns. (g) – (h) Scanning electron microscope images of the film synthesized at (g) 39.2 mM and (h) 70 mM. Scale bar is 2 microns. Other conditions: Dimethyl sulfoxide, 36.6% (v/v) acetic acid, 130 ºC temperature, 0.1 mm/s blade speed.

Figure 3. 5. Influence of acetic acid modulator concentration on zirconium 1,4-dicarboxybenzene MOF (UiO-66) film synthesis. (a) Adjusted thickness as a function of modulator concentration shows decreasing thickness. (b) Integrated grazing incidence wide-angle x-ray scattering patterns of the film synthesized at 36.6 % (v/v) acetic acid and 50% (v/v) acetic acid. (c) – (d) Two-dimensional grazing incidence wide-angle x-ray scattering patterns used to obtain Figure 5(b). (e) – (f) Scanning electron microscope images of the film synthesized with 36.6 % (v/v) acetic acid and 50% (v/v) acetic acid. Scale bar is 20 microns. (g) – (h) Scanning electron microscope images of the film synthesized with 36.6 % (v/v) acetic acid and 50% (v/v) acetic acid. Scale bar is 2 microns. Other conditions: Dimethyl sulfoxide, 39.2 mM precursor concentration, 130 ºC temperature, 0.4 mm/s blade speed.

Figure 3. 6. Scanning electron microscope images of the (a), (d) Bare anodic alumina oxide membrane, (b), (e) zirconium 1,4-dicarboxybenzene MOF (UiO-66) film synthesized on anodic alumina oxide using 1 pass of solution shearing, and (c), (f) zirconium 1,4-dicarboxybenzene MOF (UiO-66) film synthesized on anodic alumina oxide using 6 passes of solution shearing. Scale bar is 20 microns in (a) – (c) and 5 microns in (d) – (e). Synthesis conditions: N,N-dimethylformamide, 36.6% (v/v) acetic acid, 14.4 mM reactant concentration, 130 ºC temperature, and 0.1 mm/s blade speed.

1 Introduction

1.1 Metal-Organic Frameworks (MOFs)

The field of metal-organic frameworks (MOFs) has drawn great attention in the last two decades. MOFs are highly ordered porous crystalline materials (**Figure 1. 1**), linking between metal ions or secondary building units (SBUs) as nodes and organic bridging ligands as linkers.[1–6] Compared to conventionally used microporous materials, i.e., zeolites and activated carbon, MOFs typically have not only a larger surface area but also tunable chemical functionality.[4–6] Numerous different combinations of MOFs that have unique physical and chemical characteristics can be realized by changing the metal nodes and the organic linkers.[7,8] This indicates that the pore size, the shape of the crystal, and the chemistry of MOFs can be controlled depending on the nodes and linkers are chosen in the synthesis. The specific surface area of MOFs ranges from 100 m^2/g to 8,000 m^2/g,[3,5,9] and the pore size of MOFs ranges from 5 Å to 40 Å.[10] These characteristics enable MOFs for a wide range of applications such as sensor, gas separation and storage, membrane, and catalysis.[3,11,12]

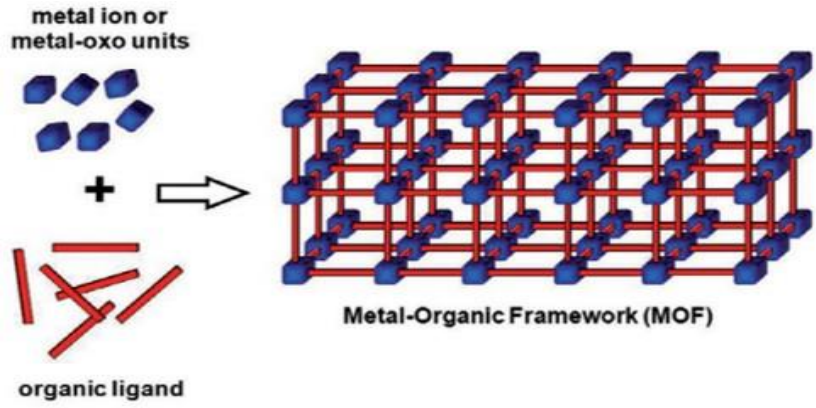

Figure 1. 1. Schematic of metal-organic Frameworks (MOFs). Metal clusters are joined with organic linkers to create a porous crystalline material. Used with permission from [2].

Ever since the MOFs were first reported around three decades ago, the field has focused on synthesizing a greater number of structures and utilizing their structures to expand their applications. Yaghi et al.[13] synthesized microporous solids that are analogous to zeolites by understanding the underlying geometric principles of nodes and linkers. The trend of past

studies was to demonstrate that the MOF can replace the application where zeolite and other microporous materials had been used by controlling their tunable pore size and chemical functionality.[12,14] For example, Long et al.[15] showed that the pores of the MOF Mg_2(dobdc) can capture CO_2 from coal-fired power plants, by showing that Mg^{2+} cation interacted with the CO_2 in the pores. In addition, Farha et al.[16] utilized computational design and simulation and successfully synthesized NU-100 that had an ultrahigh surface area (6,143 $m^2 \cdot g^{-1}$). NU-100 showed high excess H_2 storage capacity up to 70 bar at 77K (198 $mg \cdot g^{-1}$) due to its large pore volume (2.82 $cm^3 \cdot g^{-1}$) and the bulk phase density of H_2. Peikert et al.[17] published amino-substituted HKUST-1 that had the same crystal structure as HKUST-1. In particular, the amino-substituted HKUST-1 showed better NO gas storage than pristine HKUST-1 as NO bound to the amino group via chemisorption, as well as attached to the open copper sites in HKUST-1 via physisorption.[17] These studies highlight the collaboration of designing its chemical structure and utilizing physical structure of MOF pores for gas storage and separation.

1.2 Conductive Metal-Organic Frameworks

In recent years, electrically conductive MOFs have drawn attention due to the combination of charge transport and porosity, which can enable chemi-resistive sensing, transistors, solar cells, and electrocatalysts.[5,6,18,19–22] However, typical MOFs are insulators. The porous nature of MOFs inhibits the intermolecular contacts of the σ-bonded metal nodes and creates a large spatial gap between organic linkers.[19,20,23] In addition, the terminal group of the organic linkers in many MOFs is a carboxylate group. When the metals are bonded with the carboxylate-based linkers, they form coordination bonds that create a large energy bandgap.[19,20,23,24]

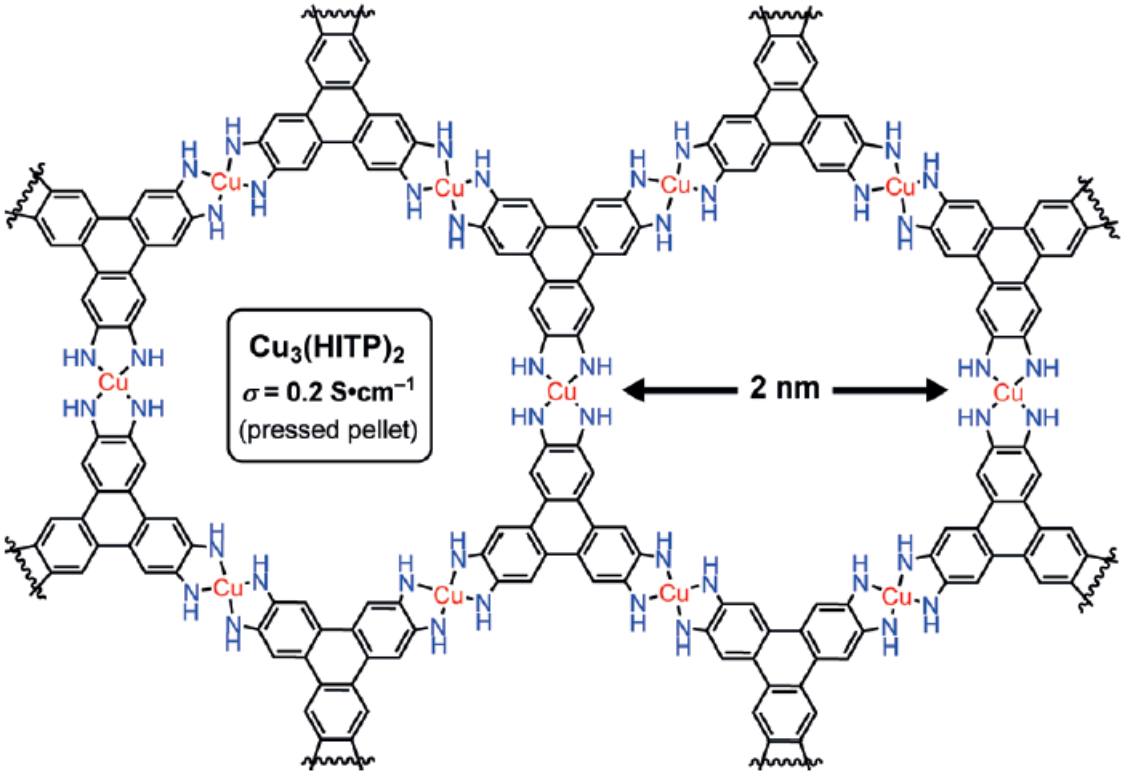

Figure 1. 2. The chemical structure of $Cu_3(HITP)_2$. The charge transfers in the MOF structure due to the redox-active aromatic cores in the linker molecules. Used with permission from [21].

Several research groups have overcome conductive limitations by allowing charge delocation via bonding and spatial interaction or by adding guest molecules into the pores. For example, Campbell et al.[21] synthesized conductive 2D Cu-based MOF, called $Cu_3(HITP)_2$ (HITP = 2,3,6,7,10,11-hexaiminotriphenylene). (**Figure 1. 2**) Due to the redox-active aromatic

cores in the linker molecule, the electrical conductivity of $Cu_3(HITP)_2$ is enhanced. In addition, Gandara et al.[25] also combined 1,2,3-triazolate with the divalent metal ions (Mg, Mn, Fe, Co, Cu, and Zn) by having coordination bonding and found the electrical conductivity of 7.7×10^{-5} S/m when Fe(1,2,3-triazolate)$_2$ was synthesized. Having the coordination bonding between electropositive linkers that contain sulfur or nitrogen-terminating groups and metal ions reduces the energy bandgap.[19,26,27]

Furthermore, electroactive aromatic linkers that have a high tendency for π-π interaction are also used to synthesize conductive MOFs. Depending upon the length of the space between linkers, the charge mobility of the MOFs changes. Xie et al.[28] reported the conductive MOF that consists of tetrathiafulvalene tetrabenzoate (TTFTB) as a linker and La^{3+} as a node. In this study, three different coordination bondings between TTFTB and La^{3+} occur depending upon the synthesis condition. The linkers of the three phases are stacked differently. It causes to change in the intensity of π-π overlap, leading the changes in electrical conductivity of all three phases. Furthermore, Chen et al.[29] constructed a Zr-based conductive MOF, called NNU-27. In this structure, long-range π-conjugation occurs in the anthracene-based linker by forming a zigzag chain along the c-axis so that the electrical conductivity of 0.13 S/m is achieved.

However, the electrical conductivity of MOFs that are composed of inherently conductive species varies significantly if the crystal morphology changes or grain boundaries form. Therefore, it is hard to achieve the desired electrical conductivity in MOFs because conductivity is highly dependent on crystalline and film properties.[19,23]

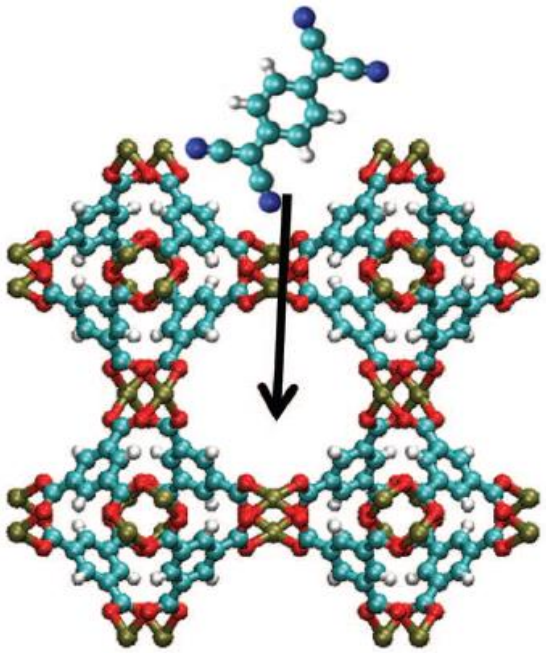

Figure 1. 3. Chemical structure of TCNQ@HKUST-1. The TCNQ moleculues are incorporated along with the HKUST-1 pores. Used with permission from [20].

On the other hand, a guest infiltration approach is a post-synthetic approach, so there is minimal disruption to the crystal structure, where a portion of the MOF porosity is sacrificed to obtain conductivity. A well-known redox-active guest-MOF system is TCNQ@HKUST-1, where Talin et al.[20] achieved six orders of magnitude higher electrical conductivity from the nominally insulating copper(II)-based MOF, HKUST-1, by infiltrating a redox-active molecule, 7,7,8,8-tetracyanoquinodimethane (TCNQ). (**Figure 1. 3**) HKUST-1 consists of Cu dimers as nodes and 1,3,5-benzenetricarboxylate (BTC) as linkers.[30,31] HKUST-1 is an insulating MOF, as the porous nature hinders the communication between the π-orbitals of BTC and d-orbitals of Cu(II) dimer, and BTC linkers are carboxylate-terminated molecules.[20,32–34] On the other hand, TCNQ incorporated HKUST-1 thin film, called TCNQ@HKUST-1, creates a continuous charge conduction pathway as TCNQ molecules bind to the open metal sites (OMS) along with the HKUST-1 pores.[20,30,35] TCNQ@HKUST-1 thin film shows stable electrical conductivity. Also, the electrical conductivity of thin film increases as more guest molecules bind to the HKUST-1.[20,36,37] However, as more guest molecules are loaded inside the pores, the available pore volume of MOFs decreases. Therefore, the electrical conductivity and accessible pore volume of guest-host MOFs should be optimized for a given application by balancing between the enhancement of electrical conductivity and the reduction of the pore volume.[20,24,36–40]

1.3 Polymer-Metal-Organic Frameworks Composite (PolyMOFs)

Including incorporating redox-active molecules into the MOF pores, polymer molecules can also be added into the MOF pores. This polymer-MOF hybrid composite is called polyMOFs. The polyMOFs contain the properties of both MOFs and polymers such as conductivity[41–43] and flexibility[44,45] from polymers and porosity and tunable as well as crystalline structure from the MOFs. Zhang et al.[46] synthesized the first polyMOF that has a similar chemical structure to IRMOF-1 by growing solvothermally between polyester-contained terephthalic acid linkers, called poly(1,4-benzenedicarboxylic acid), and zirconium (II) metal ions. Compared to conventional IRMOF-1, the polyMOF shows enhanced hydrophobicity and retained porosity of the MOF. Furthermore, Moghadam et al.[47] fabricated a flexible piezoelectric sensor device by forming a poly(vinylidene fluoride) (PVDF) and zirconium based MOF, called UiO-66, nanofiber composite. In this study, the phase of PVDF in the composite is controlled due to the hydrogen bonding interaction between COOH in UiO-66 and CF_2 in PVDF, leading to the enhanced piezoelectric performance of the composite.

These polyMOFs can be synthesized in either a physical or a chemical approach. In the physical approach, the MOFs are initially synthesized and stirred with the polymer solution so that the polymers can be loaded in the MOF pores via diffusion.[42,47] As mentioned previously, Moghadam et al.[48] fabricated PVDF@UiO-66 composite by dissolving UiO-66 particles that were grown solvothermally into the PVDF solution. Furthermore, Lu et al.[49] synthesized PVDF@UiO-66-NH_2 textiles by physically combining UiO-66 particles and PVDF fibers in N,N-dimethylformamide (DMF) for use in detoxification of chemical warfare agents. However, since two separate steps are required to synthesize the composite via the physical approach, it is inappropriate for the large-area application. In addition, large molecular weight polymers cannot be easily loaded into the MOF due to the entropic penalty.

On the other hand, the chemical approach first dissolves the polymers in solution with either the linker[46] or the node[41,50]. Once the polymer-contained linker or node units are in solution, the other component is added to synthesize the composite. Unlike the physical approach, the polymer incorporation of the composite using the chemical approach is determined by the rate of growth of MOFs. Li et al.[11] pre-coordinated negatively charged PEDOT:PSS with positively charged copper hydroxide nano strands (CHNs), and acidic linker was added to synthesize the composite, called PEDOT:PSS@HKUST-1. However, even though only one step is needed to synthesize the composite, the synthesis time of the composite still takes from hours to days as they are grown solvothermally.[41,42,44,47]

Even though many of these studies have been performed to expand the application of MOFs in the industry, the commercialization of MOFs is still at an early stage. Many studies are still required to commercialize such as scalability, and stability. Thus, it is instructive to know why MOF thin film is necessary and the current stage of MOF thin film fabrication processes.

1.4 Metal-Organic Frameworks (MOFs) Thin Film

For many applications, such as sensing, separations, and ion/charge transport, it is beneficial to create MOFs as thin films or membranes. Thin films can result in lowered mass transfer resistances while the presence of MOF pores can still result in selective performance, eg, for separation and sensing. For example, response time is one of the most important parameters that affect the performance of the sensor. It indicates how fast analyte molecules bind to the sensing materials. The response time of the sensor depends upon the diffusion rate of the analyte into the thin film. If the film is thicker, the response time of the sensor against a specific analyte takes longer to respond. However, if the film is thinner, when the analyte molecules diffuse into the thin film, the response time of the thinner film will be faster than

that of the thicker film. Depending upon the application, the thin film properties, including film coverage, thickness, grain boundaries, and crystal orientation affect the mass and charge transport of the thin film.[20,51–54] Therefore, to improve the mass, heat, and charge transport along with the MOFs thin film, it is necessary to fabricate MOF thin films that have continuous film coverage, thinner thickness, fewer grain boundaries and properly oriented towards the analyte.

1.5 Metal-Organic Frameworks (MOFs) Thin Film Fabrication Techniques

Numerous MOF thin film fabrication techniques have been explored over the past decade towards being scalable and controllable. As can be seen in **Figure 1. 4**, Hermes et al.[55] solvothermally synthesized MOF-5 thin film by soaking functionalized substrate into the precursor solution at a high temperature. Then, the thin film of MOFs has been grown on fibers and textiles through both solution-based and atomic layer deposition-based processes.[56–59] To improve the grafting of MOFs on any given substrate, carboxylic acid groups can be used to functionalize the substrate through the use of self-assembled monolayers (SAMs), which can have the added benefit of controlling MOF orientation or polymorphism.[60]

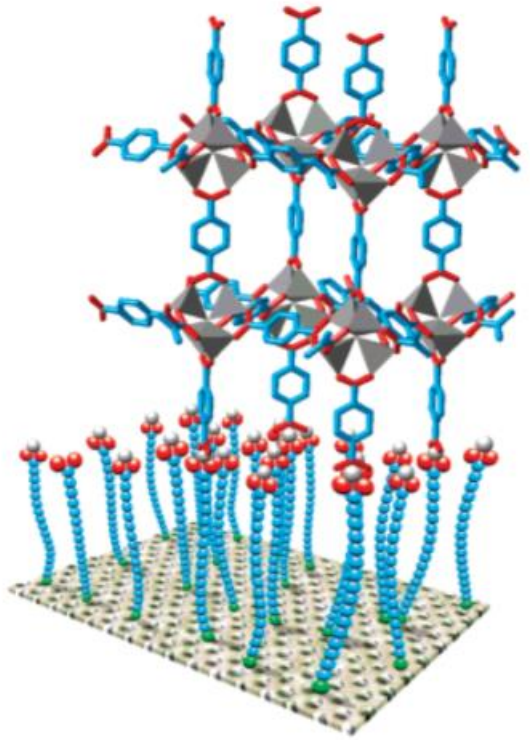

Figure 1. 4. Schematic of solvothermal MOF thin film growth. The MOFs synthesis is induced by heating the precursor solution containing both nodes and linkers. Used with permission from [55].

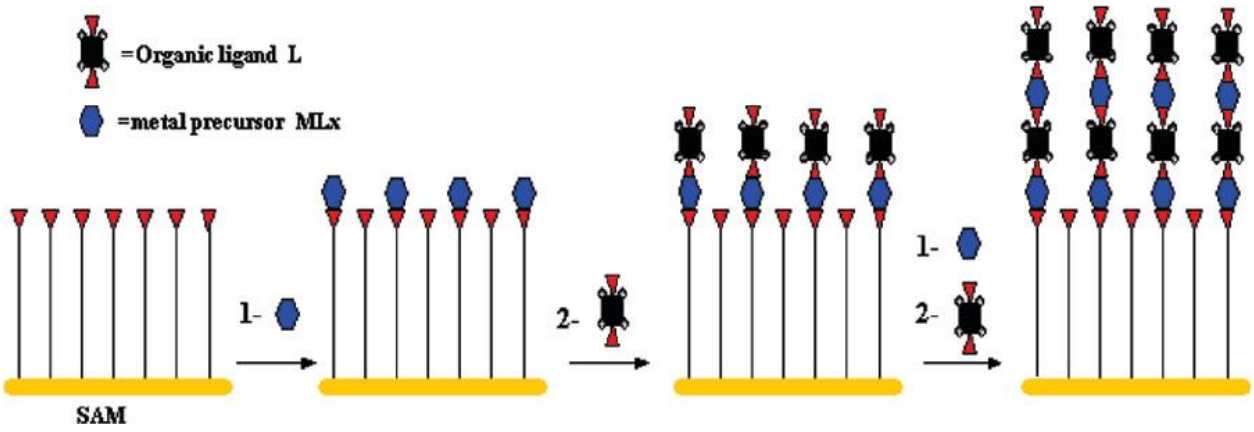

Figure 1. 5. Schematic of Layer-by-layer MOF thin film fabrication technique. MOF thin film is grown on the substrate that has created self assembled monolayer (SAM) by soaking into the the node and linker solution, respectively. Used with permission from [61].

In addition, the layer-by-layer or liquid phase epitaxy (LPE) technique has also been used to fabricate many MOF thin films.[61–67] According to Shekhah et al.[61], thin films of copper benzene-1,3,5-tricarboxylate MOF, also known as HKUST-1, can be fabricated at room temperature by repeatedly immersing the functionalized substrate into both a metal precursor solution and an organic ligand solution, respectively. (**Figure 1. 5**) The MOF thin films that were fabricated using the aforementioned techniques could control the film quality, including crystal orientation, film thickness, and roughness. However, these techniques utilize slow methods of film growth, where the growth of a film takes place in the order of hours to days. On the other hand, Huelsenbeck et al.[57] successfully synthesized several prototypical MOFs coated fabrics, including UiO-66, UiO-66-NH_2, ZIF-L, and HKUST-1, using a sequential dip coating (SQD) process. The MOF synthesis could be completed in less than a minute, and UiO-66-NH_2 showed

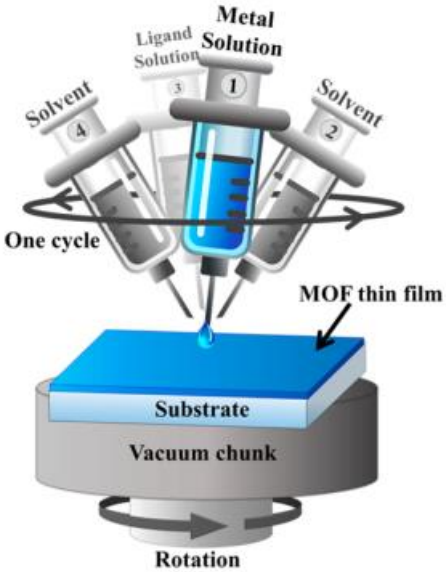

Figure 1. 6. Schematic of spin-coating MOF thin film. The synthesis takes a minute per cycle, but it is possible to produce crystal defects. Used with permission from [68].

attachment on the cotton fabrics. However, the film using this technique produces rough film, and the thickness is hard to control. Furthermore, Chernikova et al.[68] synthesized HKUST-1 thin film using spin coating deposition. (**Figure 1. 6**) By controlling spinning speed, the temperature of the substrate, and concentration of the precursor solution, uniformly distributed HKUST-1 thin film is fabricated within a minute. However, even though the synthesis takes a minute, using spin coating technique may produce crystal defects, and may not be applicable to produce large-area thin films. Thus, another fabrication technique that can control film quality and reduce fabrication time has been explored.

1.6 Meniscus-guided coating technique, solution shearing

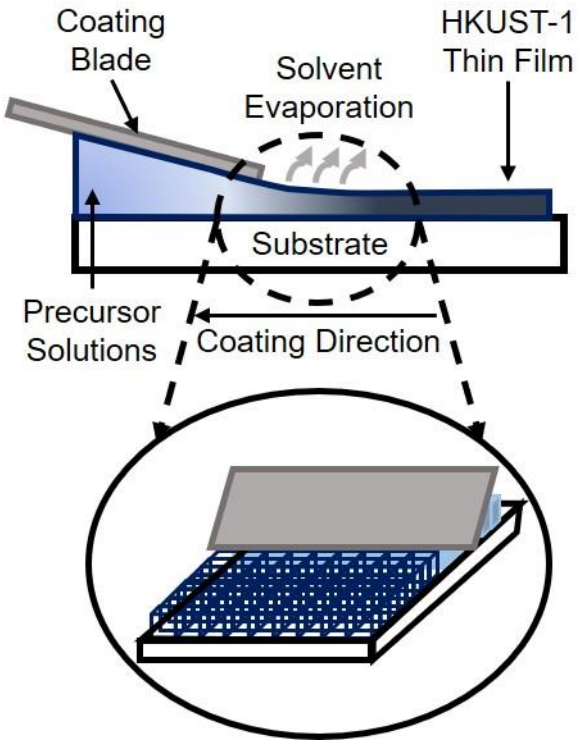

Figure 1. 7. Schematic of solution shearing. The thin film is deposited via evaporative crystallization as the coating blade moves along the substrate and solvent evaporates from the meniscus.

Recently, a meniscus-guided coating technique, called solution shearing, has drawn great attention as a technique for facile, rapid, and large area thin film fabrication (**Figure 1. 7**).[8,53,69–71] The solution shearing technique is commonly used to deposit organic semiconductors[72] and polymers[71,73]-based thin films and has been shown to be compatible with a wide range of materials such as pharmaceutical compounds[53] and carbon nanotubes.[54]

During solution shearing, the precursor solution that contains the solute of interest is injected between the translating blade and the heated substrate. As the blade moves across the substrate, the solvent evaporates, leading to supersaturation (or higher concentration causing solid phase formation in the case of a non-crystalline material) of the solute, and casts a thin film on the substrate. Thin films of numerous materials can be formed rapidly using solution shearing, and thus there is interest to study the applicability of this technique to form films of MOFs as well.[8,53,54,69,70,72,73] The substrate can be extended to be any given width since the evaporation front is invariant across the width of the substrate. In addition, continuous solution feeding during solution shearing to keep a

constant volume can be used to coat a substrate of any length. Therefore, large area thin film formation of MOFs is possible using solution shearing.

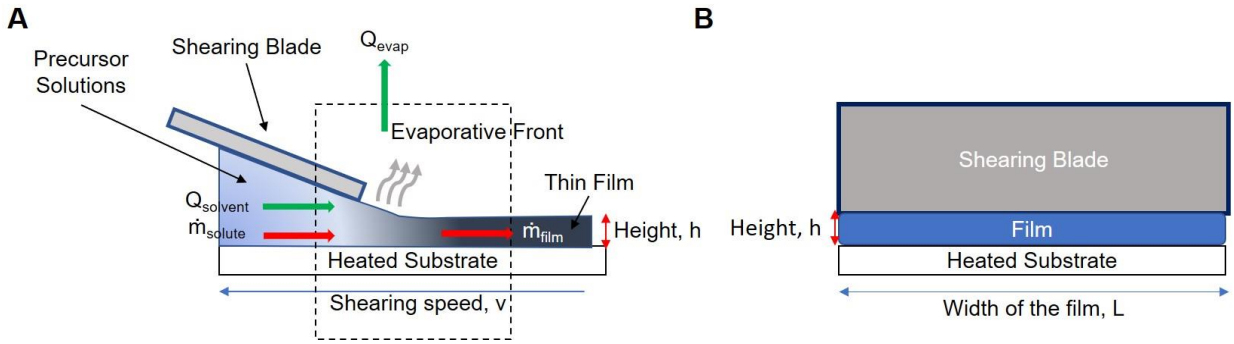

Figure 1. 8. Schematic of solution shearing for evaporative regime of the front view (left) and the side view (right).

Furthermore, solution shearing is a useful technique to control the thickness of the thin film, morphology, roughness, and orientation by varying several parameters, including blade speed, the temperature of the substrate, and the concentration of the precursor solution.[8,69] Baigl et al.[52] fabricated multilayer phospholipid thin film and controlled the thickness of the film by correlating film thickness to the blade speed. In this paper, two different regimes are observed based on the blade speed. The first regime is called the evaporation regime, where the film is deposited behind the meniscus. At the evaporation regime, the rate of solvent evaporation is similar to the rate of fluid deposition. This regime occurs at a slower blade speed. Therefore, the film thickness is determined by using a mass balance equation shown in **Figure 1. 8** and **Eq. 1.1**.

$$\dot{m}_{film} = \dot{m}_{solute}$$

$$\rho \times v \times L \times h = C \times Q_{solvent} = C \times Q_{evap} \qquad \textbf{Eq. 1.1}$$

Where ρ [g/mm^3] is the density of the solution, v [mm/s] is the blade speed, L [mm] is the width of the film, h [mm] is the film thickness, C [g/mm^3] is the concentration of solute in the solution, $Q_{solvent}$ [mm^3/s] is the rate of deposited solvent to the meniscus, Q_{evap} [mm^3/s] is the rate of solvent evaporation. It is assumed to be at a steady-state.

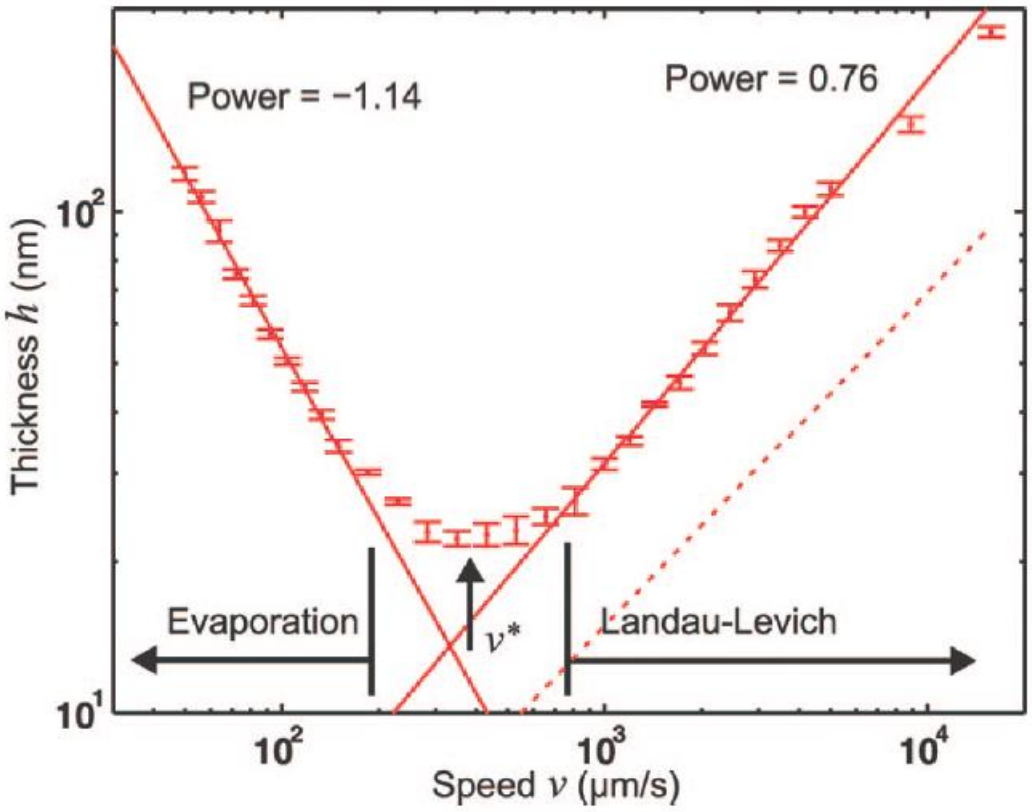

Figure 1. 9. The changes in film thickness with respect to the blade speed. At the evaporation regime, the film thickness is inversely proportional to the blade speed. On the other hand, the film thickness is proportional to the blade speed at the Landau-Levich regime. v^* is the transition speed Used with permission from [52].

As can be seen in **Eq. 1.1**, the film thickness is inversely proportional to the blade speed, indicating that the film is thicker when a slower blade speed is used, and vice versa. On the other hand, the second regime is called the Landau-Levich regime, where the film is formed after the solvent evaporates and the film deposition is dominated by viscous forces. The film deposition occurs as soon as the solvent evaporation occurs. If the blade speed is fast, a larger

amount of solution remains on the substrate, indicating that thicker film will be deposited. Therefore, the blade speed is proportional to the film thickness. (**Figure 1. 9**)

As shown in **Figure 1. 9**, the minimum thickness can be obtained at the transition regime, but the thickness of the thin film is hard to predict in this regime. Controlling the MOF film thickness using solution shearing is important as the film thickness may also impact other morphological properties such as coverage and size and shape of the crystals. Lee et al.[70] have synthesized a large area, solution sheared HKUST-1 thin film by relating the film formation to the supersaturation. In this study, the thin film properties were controlled by varying the blade speed and substrate temperature. However, the formation of a large area and continuous thin film by varying solution shearing parameters was not demonstrated. Thus, understanding the parameters of solution shearing and the effect of changes in these parameters to the thin film quality is necessary so that the solution shearing technique can be applied to form a large area and continuous MOF thin film in a rapid manner (within seconds to minutes) and allow for scalable applications as sensors and electronics.

1.7 Summary of Dissertation

In this dissertation, the formation and utilization of large-area and continuous metal organic frameworks thin films using solution shearing will be discussed. Producing large area thin films is an important technological milestone to create MOF-based thin film applications. Solution shearing is a promising technique that can scale up and control the MOF thin film properties by varying parameters such as the concentration of the precursor solution, coating speed, substrate temperature, and the type of substrate. However, fabricating a large area and continuous MOF thin film using solution shearing is limited.

In **Chapter 2**, the fabrication of large-area and continuous HKUST-1 thin film will be discussed. We hypothesized that multiple cycles of solution shearing on the same substrate would enhance the film coverage due to the secondary crystallization. Mao *et al*.[74] realized a continuous and well-intergrown HKUST-1 membrane within an hour by adhering HKUST-1 seeds on the substrate before the thin film was fabricated, using secondary crystallization to ensure full film coverage. We utilize the same understanding of secondary crystallization to obtain large area and continuous HKUST-1 thin films. The first solution shearing cycle results in the deposition of small HKUST-1 crystallites on the substrate, and subsequent solution shearing cycles lead to a combination of crystal nucleation and growth on the existing HKUST-1 crystallites so that a fully completed thin film is fabricated. Once the HKUST-1 thin film is fabricated, TCNQ molecules would be incorporated into the thin film to confirm the film coverage. Last, as an advancement of the proposed work by Dr. Luke Huelsenbeck, the pool-based active learning (PAL) and regression methods are utilized to optimize the solution shearing synthesis of fully covered HKUST-1 thin film with the minimum thickness. The active learning approach is adopted into solution shearing parameters. Among the millions of different combinations in solution shearing parameters, only one parameter set that provides the large

area, continuous as well as the thinnest HKUST-1 thin film is given. This approach can dramatically save the time to find an optimized parameter of solution sheared HKUST-1 thin film.

The previous study is focused on the crystallization of solution sheared HKUST-1 thin film only. However, there have been no previous reports of solution shearing based evaporative crystallization of zirconium-based MOFs, which have been widely studied for a range of applications, including separations, catalysis, sensing, and charge transport due to their enhanced chemical and thermal stability.[75] Thus, in **Chapter 3**, the zirconium 1,4-dicarboxybenzene MOF, UiO-66, is formed using solution shearing, and the effect of various parameters (modulator concentration, temperature, blade speed, and precursor concentration) is explored to determine its crystallinity. Therefore, this study shows that solution shearing is a promising thin film fabrication technique that can form thin films of a wide range of MOFs of interest for future applications.

In **Chapter 4**, many studies have been performed to incorporate polymers into the MOF pores and synthesize polymer@MOF composites. In the conventional synthesis of polymer@MOF, the polymer solution is stirred with synthesized MOFs. By mixing polymer and MOF crystals, the polymer is incorporated into the MOF pores. However, in this chapter, a polymer is impregnated into the pores while MOF is grown as thin films. Polyvinylidene fluoride (PVDF) is dissolved with the UiO-66 precursor solution. PVDF@UiO-66 thin film is fabricated using solution shearing. After PVDF@UiO-66 thin film is fabricated, its potential application is explored such as flexible gas sensor or electronics.

At the end of the dissertation, the thesis is concluded by discussing the feasible application of polymer@MOF composites to demonstrate the advantages of synthesizing polymer@MOF composites against pristine polymer and MOFs.

1.8 References

(1) Zheng, Y.; Zheng, S.; Xue, H.; Pang, H. Metal-Organic Frameworks/Graphene-Based Materials: Preparations and Applications. *Adv. Funct. Mater.* **2018**, *1804950*, 1804950. https://doi.org/10.1002/adfm.201804950.

(2) Gliemann, H.; Wöll, C. Epitaxially Grown Metal-Organic Frameworks. *Mater. Today* **2012**, *15* (3), 110–116. https://doi.org/10.1016/S1369-7021(12)70046-9.

(3) Furukawa, H.; Ko, N.; Go, Y. B.; Aratani, N.; Choi, S. B.; Choi, E.; Yazaydin, A. O.; Snurr, R. Q.; O'Keeffe, M.; Kim, J.; Yaghi, O. M. Ultrahigh Porosity in Metal-Organic Frameworks. *Science* **2010**, *329* (5990), 424–428. https://doi.org/10.1126/science.1192160.

(4) Bétard, A.; Fischer, R. A. Metal–Organic Framework Thin Films: From Fundamentals to Applications. *Chem. Rev.* **2012**, *112* (2), 1055–1083. https://doi.org/10.1021/cr200167v.

(5) Shekhah, O.; Liu, J.; Fischer, R. A.; Wöll, Ch. MOF Thin Films: Existing and Future Applications. *Chem. Soc. Rev.* **2011**, *40* (2), 1081. https://doi.org/10.1039/c0cs00147c.

(6) Zacher, D.; Shekhah, O.; Wöll, C.; Fischer, R. A. Thin Films of Metal–Organic Frameworks. *Chem. Soc. Rev.* **2009**, *38* (5), 1418. https://doi.org/10.1039/b805038b.

(7) Kreno, L. E.; Leong, K.; Farha, O. K.; Allendorf, M.; Van Duyne, R. P.; Hupp, J. T. Metal–Organic Framework Materials as Chemical Sensors. *Chem. Rev.* **2012**, *112* (2), 1105–1125. https://doi.org/10.1021/cr200324t.

(8) Ghorbanpour, A.; Huelsenbeck, L. D.; Smilgies, D.-M.; Giri, G. Oriented UiO-66 Thin Films through Solution Shearing. *CrystEngComm* **2018**, *20* (3), 294–300. https://doi.org/10.1039/C7CE01801K.

(9) Furukawa, H.; Cordova, K. E.; O'Keeffe, M.; Yaghi, O. M. The Chemistry and Applications of Metal-Organic Frameworks. *Science* **2013**, *341* (6149), 1230444–1230444. https://doi.org/10.1126/science.1230444.

(10) Furukawa, H.; Cordova, K. E.; O'Keeffe, M.; Yaghi, O. M. The Chemistry and Applications of Metal-Organic Frameworks. *Science* **2013**, *341* (6149), 1230444–1230444. https://doi.org/10.1126/science.1230444.

(11) Kreno, L. E.; Leong, K.; Farha, O. K.; Allendorf, M.; Duyne, R. P. Van; Hupp, J. T. Metal - Organic Framework Materials as Chemical Sensors. *Chem. Rev.* **2012**, *112*, 1105–1125. https://doi.org/10.1021/cr200324t.

(12) Zhou, H.-C.; Long, J. R.; Yaghi, O. M. Introduction to Metal–Organic Frameworks. *Chem. Rev.* **2012**, *112* (2), 673–674. https://doi.org/10.1021/cr300014x.

(13) Yaghi, O. M.; Li, H. Hydrothermal Synthesis of a Metal-Organic Framework Containing Large Rectangular Channels. *J. Am. Chem. Soc.* **1995**, *117* (41), 10401–10402. https://doi.org/10.1021/ja00146a033.

(14) Eddaoudi, M.; Kim, J.; Rosi, N.; Vodak, D.; Wachter, J.; O'Keeffe, M.; Yaghi, O. M. Systematic Design of Pore Size and Functionality in Isoreticular MOFs and Their Application in Methane Storage. *Science* **2002**, *295* (5554), 469–472. https://doi.org/10.1126/science.1067208.

(15) Kong, X.; Scott, E.; Ding, W.; Mason, J. A.; Long, J. R.; Reimer, J. A. CO_2 Dynamics in a Metal–Organic Framework with Open Metal Sites. *J. Am. Chem. Soc.* **2012**, *134* (35), 14341–14344. https://doi.org/10.1021/ja306822p.

(16) Farha, O. K.; Özgür Yazaydın, A.; Eryazici, I.; Malliakas, C. D.; Hauser, B. G.; Kanatzidis, M. G.; Nguyen, S. T.; Snurr, R. Q.; Hupp, J. T. De Novo Synthesis of a Metal–Organic Framework Material Featuring Ultrahigh Surface Area and Gas Storage Capacities. *Nat. Chem.* **2010**, *2* (11), 944–948. https://doi.org/10.1038/nchem.834.

(17) Peikert, K.; Hoffmann, F.; Fröba, M. Amino Substituted Cu3(Btc)2: A New Metal–Organic Framework with a Versatile Functionality. *Chem. Commun.* **2012**, *48* (91), 11196. https://doi.org/10.1039/c2cc36220a.
(18) Davis, M. E. Ordered Porous Materials for Emerging Applications. *Nature* **2002**, *417* (6891), 813–821. https://doi.org/10.1038/nature00785.
(19) Xie, L. S.; Skorupskii, G.; Dincă, M. Electrically Conductive Metal–Organic Frameworks. *Chem. Rev.* **2020**, acs.chemrev.9b00766. https://doi.org/10.1021/acs.chemrev.9b00766.
(20) Talin, A. A.; Centrone, A.; Ford, A. C.; Foster, M. E.; Stavila, V.; Haney, P.; Kinney, R. A.; Szalai, V.; El Gabaly, F.; Yoon, H. P.; Léonard, F.; Allendorf, M. D. Tunable Electrical Conductivity in Metal-Organic Framework Thin-Film Devices. *Science* **2014**, *343* (6166), 66–69. https://doi.org/10.1126/science.1246738.
(21) Campbell, M. G.; Sheberla, D.; Liu, S. F.; Swager, T. M.; Dincă, M. Cu $_3$ (Hexaiminotriphenylene) $_2$: An Electrically Conductive 2D Metal-Organic Framework for Chemiresistive Sensing. *Angew. Chem. Int. Ed.* **2015**, *54* (14), 4349–4352. https://doi.org/10.1002/anie.201411854.
(22) Hendon, C. H.; Tiana, D.; Walsh, A. Conductive Metal–Organic Frameworks and Networks: Fact or Fantasy? *Phys. Chem. Chem. Phys.* **2012**, *14* (38), 13120. https://doi.org/10.1039/c2cp41099k.
(23) Nidamanuri, N.; Maity, K.; Saha, S. Electrically Conductive Metal-Organic Frameworks. In *Series on Chemistry, Energy and the Environment*; WORLD SCIENTIFIC, 2018; Vol. 02, pp 655–686. https://doi.org/10.1142/9789813226739_0015.
(24) Schneider, C.; Ukaj, D.; Koerver, R.; Talin, A. A.; Kieslich, G.; Pujari, S. P.; Zuilhof, H.; Janek, J.; Allendorf, M. D.; Fischer, R. A. High Electrical Conductivity and High Porosity in a Guest@MOF Material: Evidence of TCNQ Ordering within Cu $_3$ BTC $_2$ Micropores. *Chem. Sci.* **2018**, *9* (37), 7405–7412. https://doi.org/10.1039/C8SC02471E.
(25) Gándara, F.; Uribe-Romo, F. J.; Britt, D. K.; Furukawa, H.; Lei, L.; Cheng, R.; Duan, X.; O'Keeffe, M.; Yaghi, O. M. Porous, Conductive Metal-Triazolates and Their Structural Elucidation by the Charge-Flipping Method. *Chem. - Eur. J.* **2012**, *18* (34), 10595–10601. https://doi.org/10.1002/chem.201103433.
(26) Nidamanuri, N.; Maity, K.; Saha, S. Electrically Conductive Metal-Organic Frameworks. In *Series on Chemistry, Energy and the Environment*; WORLD SCIENTIFIC, 2018; Vol. 02, pp 655–686. https://doi.org/10.1142/9789813226739_0015.
(27) Hendon, C. H.; Tiana, D.; Walsh, A. Conductive Metal–Organic Frameworks and Networks: Fact or Fantasy? *Phys. Chem. Chem. Phys.* **2012**, *14* (38), 13120. https://doi.org/10.1039/c2cp41099k.
(28) Xie, L. S.; Alexandrov, E. V.; Skorupskii, G.; Proserpio, D. M.; Dincă, M. Diverse π–π Stacking Motifs Modulate Electrical Conductivity in Tetrathiafulvalene-Based Metal–Organic Frameworks. *Chem. Sci.* **2019**, *10* (37), 8558–8565. https://doi.org/10.1039/C9SC03348C.
(29) Chen, D.; Xing, H.; Su, Z.; Wang, C. Electrical Conductivity and Electroluminescence of a New Anthracene-Based Metal–Organic Framework with π-Conjugated Zigzag Chains. *Chem. Commun.* **2016**, *52* (10), 2019–2022. https://doi.org/10.1039/C5CC09065B.
(30) Hendon, C. H.; Walsh, A. Chemical Principles Underpinning the Performance of the Metal-Organic Framework HKUST-1. *Chem. Sci.* **2015**, *6* (7), 3674–3683. https://doi.org/10.1039/c5sc01489a.

(31) Stephen, S.; Samuel, M.; Jonathan, P. H.; Orpen, A. G.; Ian, D. A Chemically Functionalizable Nanoporous Material [Cu3 (TMA) 2 (H2O) 3] n. **1999**, *3* (February), 1148–1151.
(32) Furukawa, H.; Cordova, K. E.; O'Keeffe, M.; Yaghi, O. M. The Chemistry and Applications of Metal-Organic Frameworks. *Science* **2013**, *341* (6149). https://doi.org/10.1126/science.1230444.
(33) Long, J. R. Introduction to Metal − Organic Frameworks. *Chem. Rev.* **2012**, *112*, 673–674. https://doi.org/10.1021/cr300014x.
(34) Stock, N.; Biswas, S.; Topologies, M. O. F.; Stock, N.; Biswas, S. Synthesis of Metal-Organic Frameworks (MOFs): Routes to Various. *Chem. Rev.* **2012**, *112* (2), 933–969. https://doi.org/10.1021/cr200304e.
(35) Kim, H. K.; Yun, W. S.; Kim, M.-B.; Kim, J. Y.; Bae, Y.-S.; Lee, J.; Jeong, N. C. A Chemical Route to Activation of Open Metal Sites in the Copper-Based Metal–Organic Framework Materials HKUST-1 and Cu-MOF-2. *J. Am. Chem. Soc.* **2015**, *137* (31), 10009–10015. https://doi.org/10.1021/jacs.5b06637.
(36) Thürmer, K.; Schneider, C.; Stavila, V.; Friddle, R. W.; Léonard, F.; Fischer, R. A.; Allendorf, M. D.; Talin, A. A. Surface Morphology and Electrical Properties of Cu_3BTC_2 Thin Films Before and After Reaction with TCNQ. *ACS Appl. Mater. Interfaces* **2018**, *10* (45), 39400–39410. https://doi.org/10.1021/acsami.8b15158.
(37) Goswami, S.; Ray, D.; Otake, K.; Kung, C.-W.; Garibay, S. J.; Islamoglu, T.; Atilgan, A.; Cui, Y.; Cramer, C. J.; Farha, O. K.; Hupp, J. T. A Porous, Electrically Conductive Hexa-Zirconium(IV) Metal–Organic Framework. *Chem. Sci.* **2018**, *9* (19), 4477–4482. https://doi.org/10.1039/C8SC00961A.
(38) Allendorf, M. D.; Foster, M. E.; Léonard, F.; Stavila, V.; Feng, P. L.; Doty, F. P.; Leong, K.; Ma, E. Y.; Johnston, S. R.; Talin, A. A. Guest-Induced Emergent Properties in Metal–Organic Frameworks. *J. Phys. Chem. Lett.* **2015**, *6* (7), 1182–1195. https://doi.org/10.1021/jz5026883.
(39) Rivera-Torrente, M.; Filez, M.; Schneider, C.; Wolkersdörfer, K.; Taffa, D. H.; Wark, M.; Fischer, R. A. Micro-Spectroscopy of KUST-1 Metal-Organic Framework Crystals Loaded with Tetracyanoquinodimethane: Effects of Water on Host- Guest Chemistry and Electrical Conductivity. 10.
(40) Allendorf, M. D.; Medishetty, R.; Fischer, R. A. Guest Molecules as a Design Element for Metal–Organic Frameworks. *MRS Bull.* **2016**, *41* (11), 865–869. https://doi.org/10.1557/mrs.2016.244.
(41) Li, Z.; Guo, Y.; Wang, X.; Ying, W.; Chen, D.; Ma, X.; Zhao, X.; Peng, X. Highly Conductive PEDOT:PSS Threaded HKUST-1 Thin Films. *Chem. Commun.* **2018**, *54* (98), 13865–13868. https://doi.org/10.1039/C8CC07591C.
(42) Lu, A. X.; McEntee, M.; Browe, M. A.; Hall, M. G.; DeCoste, J. B.; Peterson, G. W. MOFabric: Electrospun Nanofiber Mats from PVDF/UiO-66-NH_2 for Chemical Protection and Decontamination. *ACS Appl. Mater. Interfaces* **2017**, *9* (15), 13632–13636. https://doi.org/10.1021/acsami.7b01621.
(43) Shanahan, J.; Kissel, D. S.; Sullivan, E. PANI@UiO-66 and PANI@UiO-66-NH_2 Polymer-MOF Hybrid Composites as Tunable Semiconducting Materials. *ACS Omega* **2020**, *5* (12), 6395–6404. https://doi.org/10.1021/acsomega.9b03834.
(44) Lv, D.; Chen, W.; Shen, W.; Peng, M.; Zhang, X.; Wang, R.; Xu, L.; Xu, W.; Song, W.; Tan, R. Enhanced Flexible Room Temperature Ammonia Sensor Based on PEDOT: PSS

Thin Film with FeCl3 Additives Prepared by Inkjet Printing. *Sens. Actuators B Chem.* **2019**, *298*, 126890. https://doi.org/10.1016/j.snb.2019.126890.

(45) Zhang, Z.; Nguyen, H. T. H.; Miller, S. A.; Ploskonka, A. M.; DeCoste, J. B.; Cohen, S. M. Polymer–Metal–Organic Frameworks (PolyMOFs) as Water Tolerant Materials for Selective Carbon Dioxide Separations. *J. Am. Chem. Soc.* **2016**, *138* (3), 920–925. https://doi.org/10.1021/jacs.5b11034.

(46) Zhang, Z.; Nguyen, H. T. H.; Miller, S. A.; Cohen, S. M. PolyMOFs: A Class of Interconvertible Polymer-Metal-Organic-Framework Hybrid Materials. *Angew. Chem. Int. Ed.* **2015**, *54* (21), 6152–6157. https://doi.org/10.1002/anie.201502733.

(47) Moghadam, B. H.; Hasanzadeh, M.; Simchi, A. Self-Powered Wearable Piezoelectric Sensors Based on Polymer Nanofiber–Metal–Organic Framework Nanoparticle Composites for Arterial Pulse Monitoring. *ACS Appl. Nano Mater.* **2020**, *3* (9), 8742–8752. https://doi.org/10.1021/acsanm.0c01551.

(48) Moghadam, B. H.; Hasanzadeh, M.; Simchi, A. Self-Powered Wearable Piezoelectric Sensors Based on Polymer Nanofiber–Metal–Organic Framework Nanoparticle Composites for Arterial Pulse Monitoring. *ACS Appl. Nano Mater.* **2020**, *3* (9), 8742–8752. https://doi.org/10.1021/acsanm.0c01551.

(49) Lu, A. X.; McEntee, M.; Browe, M. A.; Hall, M. G.; DeCoste, J. B.; Peterson, G. W. MOFabric: Electrospun Nanofiber Mats from PVDF/UiO-66-NH2 for Chemical Protection and Decontamination. *ACS Appl. Mater. Interfaces* **2017**, *9* (15), 13632–13636. https://doi.org/10.1021/acsami.7b01621.

(50) Guo, Y.; Ying, Y.; Mao, Y.; Peng, X.; Chen, B. Polystyrene Sulfonate Threaded through a Metal-Organic Framework Membrane for Fast and Selective Lithium-Ion Separation. *Angew. Chem. Int. Ed.* **2016**, *55* (48), 15120–15124. https://doi.org/10.1002/anie.201607329.

(51) Achmann, S.; Hagen, G.; Kita, J.; Malkowsky, I.; Kiener, C.; Moos, R. Metal-Organic Frameworks for Sensing Applications in the Gas Phase. *Sensors* **2009**, *9* (3), 1574–1589. https://doi.org/10.3390/s90301574.

(52) Le Berre, M.; Chen, Y.; Baigl, D. From Convective Assembly to Landau−Levich Deposition of Multilayered Phospholipid Films of Controlled Thickness. *Langmuir* **2009**, *25* (5), 2554–2557. https://doi.org/10.1021/la803646e.

(53) Guthrie, S. M.; Smilgies, D.-M.; Giri, G. Controlling Polymorphism in Pharmaceutical Compounds Using Solution Shearing. *Cryst. Growth Des.* **2018**, *18* (2), 602–606. https://doi.org/10.1021/acs.cgd.7b01686.

(54) Park, S.; Pitner, G.; Giri, G.; Koo, J. H.; Park, J.; Kim, K.; Wang, H.; Sinclair, R.; Wong, H.-S. P.; Bao, Z. Large-Area Assembly of Densely Aligned Single-Walled Carbon Nanotubes Using Solution Shearing and Their Application to Field-Effect Transistors. *Adv. Mater.* **2015**, *27* (16), 2656–2662. https://doi.org/10.1002/adma.201405289.

(55) Hermes, S.; Schröder, F.; Chelmowski, R.; Wöll, C.; Fischer, R. A. Selective Nucleation and Growth of Metal−Organic Open Framework Thin Films on Patterned COOH/CF_3-Terminated Self-Assembled Monolayers on Au(111). *J. Am. Chem. Soc.* **2005**, *127* (40), 13744–13745. https://doi.org/10.1021/ja053523l.

(56) Dai, Z.; Lee, D. T.; Shi, K.; Wang, S.; Barton, H. F.; Zhu, J.; Yan, J.; Ke, Q.; Parsons, G. N. Fabrication of a Freestanding Metal Organic Framework Predominant Hollow Fiber Mat and Its Potential Applications in Gas Separation and Catalysis. *J. Mater. Chem. A* **2020**, *8* (7), 3803–3813. https://doi.org/10.1039/C9TA11701F.

(57) Huelsenbeck, L.; Luo, H.; Verma, P.; Dane, J.; Ho, R.; Beyer, E.; Hall, H.; Geise, G. M.; Giri, G. Generalized Approach for Rapid Aqueous MOF Synthesis by Controlling Solution PH. *Cryst Growth Des* **2020**, 9.

(58) Lee, D. T.; Jamir, J. D.; Peterson, G. W.; Parsons, G. N. Protective Fabrics: Metal-Organic Framework Textiles for Rapid Photocatalytic Sulfur Mustard Simulant Detoxification. *Matter* **2020**, *2* (2), 404–415. https://doi.org/10.1016/j.matt.2019.11.005.

(59) Yao, B.-J.; Ding, L.-G.; Li, F.; Li, J.-T.; Fu, Q.-J.; Ban, Y.; Guo, A.; Dong, Y.-B. Chemically Cross-Linked MOF Membrane Generated from Imidazolium-Based Ionic Liquid-Decorated UiO-66 Type NMOF and Its Application toward CO_2 Separation and Conversion. *ACS Appl. Mater. Interfaces* **2017**, *9* (44), 38919–38930. https://doi.org/10.1021/acsami.7b12697.

(60) Verma, P. K.; Huelsenbeck, L.; Nichols, A. W.; Islamoglu, T.; Heinrich, H.; Machan, C. W.; Giri, G. Controlling Polymorphism and Orientation of NU-901/NU-1000 Metal–Organic Framework Thin Films. *Chem. Mater.* **2020**, *32* (24), 10556–10565. https://doi.org/10.1021/acs.chemmater.0c03539.

(61) Shekhah, O.; Wang, H.; Kowarik, S.; Schreiber, F.; Paulus, M.; Tolan, M.; Sternemann, C.; Evers, F.; Zacher, D.; Fischer, R. A.; Wöll, C. Step-by-Step Route for the Synthesis of Metal−Organic Frameworks. *J. Am. Chem. Soc.* **2007**, *129* (49), 15118–15119. https://doi.org/10.1021/ja076210u.

(62) Yao, M.-S.; Lv, X.-J.; Fu, Z.-H.; Li, W.-H.; Deng, W.-H.; Wu, G.-D.; Xu, G. Layer-by-Layer Assembled Conductive Metal-Organic Framework Nanofilms for Room-Temperature Chemiresistive Sensing. *Angew. Chem.* **2017**, *129* (52), 16737–16741. https://doi.org/10.1002/ange.201709558.

(63) Kuhn, H.; Möbius, D. Systems of Monomolecular Layers-Assembling and Physico-Chemical Behavior. *Angew. Chem. Int. Ed. Engl.* **1971**, *10* (9), 620–637. https://doi.org/10.1002/anie.197106201.

(64) Decher, G. Fuzzy Nanoassemblies: Toward Layered Polymeric Multicomposites. *Science* **1997**, *277* (5330), 1232–1237. https://doi.org/10.1126/science.277.5330.1232.

(65) Ohara, H.; Yamamoto, S.; Kuzuhara, D.; Koganezawa, T.; Oikawa, H.; Mitsuishi, M. Layer-by-Layer Growth Control of Metal–Organic Framework Thin Films Assembled on Polymer Films. *ACS Appl. Mater. Interfaces* **2020**, *12* (45), 50784–50792. https://doi.org/10.1021/acsami.0c13016.

(66) Zhao, J.; Gong, B.; Nunn, W. T.; Lemaire, P. C.; Stevens, E. C.; Sidi, F. I.; Williams, P. S.; Oldham, C. J.; Walls, H. J.; Shepherd, S. D.; Browe, M. A.; Peterson, G. W.; Losego, M. D.; Parsons, G. N. Conformal and Highly Adsorptive Metal–Organic Framework Thin Films via Layer-by-Layer Growth on ALD-Coated Fiber Mats. *J. Mater. Chem. A* **2015**, *3* (4), 1458–1464. https://doi.org/10.1039/C4TA05501B.

(67) Nijem, N.; Fürsich, K.; Kelly, S. T.; Swain, C.; Leone, S. R.; Gilles, M. K. HKUST-1 Thin Film Layer-by-Layer Liquid Phase Epitaxial Growth: Film Properties and Stability Dependence on Layer Number. *Cryst. Growth Des.* **2015**, *15* (6), 2948–2957. https://doi.org/10.1021/acs.cgd.5b00384.

(68) Chernikova, V.; Shekhah, O.; Eddaoudi, M. Advanced Fabrication Method for the Preparation of MOF Thin Films: Liquid-Phase Epitaxy Approach Meets Spin Coating Method. *ACS Appl. Mater. Interfaces* **2016**, *8* (31), 20459–20464. https://doi.org/10.1021/acsami.6b04701.

(69) Jung, S.; Huelsenbeck, L.; Hu, Q.; Robinson, S.; Giri, G. Conductive, Large-Area, and Continuous 7,7,8,8-Tetracyanoquinodimethane@HKUST-1 Thin Films Fabricated Using

Solution Shearing. *ACS Appl. Mater. Interfaces* **2021**, *13* (8), 10202–10209. https://doi.org/10.1021/acsami.1c00640.
(70) Lee, J.-C.; Kim, J.-O.; Lee, H.-J.; Shin, B.; Park, S. Meniscus-Guided Control of Supersaturation for the Crystallization of High Quality Metal Organic Framework Thin Films. *Chem. Mater.* **2019**, *31* (18), 7377–7385. https://doi.org/10.1021/acs.chemmater.9b01996.
(71) Worfolk, B. J.; Andrews, S. C.; Park, S.; Reinspach, J.; Liu, N.; Toney, M. F.; Mannsfeld, S. C. B.; Bao, Z. Ultrahigh Electrical Conductivity in Solution-Sheared Polymeric Transparent Films. *Proc. Natl. Acad. Sci.* **2015**, *112* (46), 14138–14143. https://doi.org/10.1073/pnas.1509958112.
(72) Chen, M.; Peng, B.; Huang, S.; Chan, P. K. L. Understanding the Meniscus-Guided Coating Parameters in Organic Field-Effect-Transistor Fabrications. *Adv. Funct. Mater.* **2020**, *30* (1), 1905963. https://doi.org/10.1002/adfm.201905963.
(73) Shaw, L.; Hayoz, P.; Diao, Y.; Reinspach, J. A.; To, J. W. F.; Toney, M. F.; Weitz, R. T.; Bao, Z. Direct Uniaxial Alignment of a Donor–Acceptor Semiconducting Polymer Using Single-Step Solution Shearing. *ACS Appl. Mater. Interfaces* **2016**, *8* (14), 9285–9296. https://doi.org/10.1021/acsami.6b01607.
(74) Mao, Y.; Cao, W.; Li, J.; Liu, Y.; Ying, Y.; Sun, L.; Peng, X. Enhanced Gas Separation through Well-Intergrown MOF Membranes: Seed Morphology and Crystal Growth Effects. *J. Mater. Chem. A* **2013**, *1* (38), 11711. https://doi.org/10.1039/c3ta12402a.
(75) Winarta, J.; Shan, B.; Mcintyre, S. M.; Ye, L.; Wang, C.; Liu, J.; Mu, B. A Decade of UiO-66 Research: A Historic Review of Dynamic Structure, Synthesis Mechanisms, and Characterization Techniques of an Archetypal Metal–Organic Framework. *Cryst. Growth Des.* **2020**, *20* (2), 1347–1362. https://doi.org/10.1021/acs.cgd.9b00955.

2 Fabrication and Optimization of Conductive, Large-Area, and Continuous 7,7,8,8-Tetracyanoquinodimethane@HKUST-1 Thin Films Using Solution Shearing

2.1 The works of this chapter are published as:

S. Jung, L. Huelsenbeck, Q. Hu, S. Robinson, and G. Giri. "Conductive, Large-Area, and Continuous 7,7,8,8-Tetracyanoquinodimethane@HKUST-1 Thin Films Fabricated Using Solution Shearing." *ACS Appl. Mater. Interfaces* 2021, 13, 8, 10202-10209. https://doi.org/10.1021/acsami.1c00640
S. Jung, L. Huelsenbeck, R. Herrera del Valle, P. Balachandran, and G. Giri. "Accelerated HKUST-1 Thin Film Property Optimization Using Active Learning." ACS Appl. Mater. Interfaces, 2021, 13, 51, 61827-61837. https://doi.org/10.1021/acsami.1c20788

2.2 Abstract

Conventional MOF thin film fabrication techniques, such as solvothermal growth and layer-by-layer growth, have some technical limitations, including slow crystallization kinetics, poor control over crystal orientation, or uncontrolled film thickness. This chapter focus on fabricating Cu-based MOF (HKUST-1) thin film using a meniscus guided coating technique, called solution shearing. Solution shearing can fabricate MOF thin film within a minute and control crystal orientation and film thickness. Even though solution sheared HKUST-1 thin film enables to control the size of the crystals and the thickness of the thin film, it is hard to synthesize a large area and continuous HKUST-1 thin film. In this work, we hypothesize that repeating solution shearing cycles enhance the film coverage. The initial solution shearing cycle can be regarded as the deposition of the seed crystals, and subsequent solution shearing cycles may induce the secondary crystallization on the substrate. The film coverage of the large-area and continuous HKUST-1 thin film is confirmed by incorporating a redox-active molecule, called 7,7,8,8-

Tetracyanoquinodimethane (TCNQ). The TCNQ@HKUST-1 composite shows seven orders of magnitude higher electrical conductivity than the pristine HKUST-1. In addition, the active learning approach is adopted into solution shearing parameters. This approach can dramatically save the time to find an optimized parameter that fits the application in a large parameter space. Overall, the solution shearing technique may have the potential to be used as a high throughput MOF thin film fabrication technique, allowing MOF thin films to be used for scalable applications such as bio-sensors and electronics.

2.3 Introduction

Several MOF thin film fabrication techniques have been used to deposit MOF thin films such as solvothermal growth,[1–3] colloidal deposition growth,[4] layer-by-layer growth,[5] and gel-layer growth.[6] However, these techniques have several-drawbacks including slow crystallization kinetics, lack of film orientation control, rough film surface, or uncontrolled film thickness. Unlike these aforementioned techniques, solution shearing, which is a type of meniscus-guided coating technique, has been demonstrated as a versatile, yet simple approach to create film rapidly and control the film thickness and crystal orientation.[7–9] As depicted in **Figure 2. 1**, the precursor solution containing both the metal node and the organic linker is deposited on the heated substrate. The coating blade is dragged over the

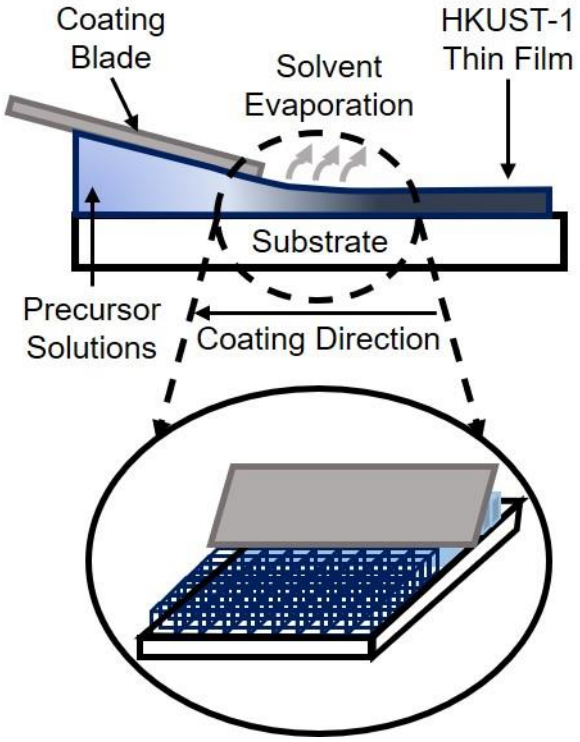

Figure 2. 1. Schematic of solution shearing technique. The thin film is deposited via evaporative crystallization as the coating blade moves along the substrate and solvent evaporates from the meniscus.

deposited solution, creating a meniscus where solvent evaporation occurs, resulting in thin film crystallization.[7,9,10] Lee *et al*.[9] demonstrated Cu (II)-based MOF, HKUST-1, thin film formation using meniscus-guided crystallization (MGC) with tunable shape patterns and uniform size and thickness by adjusting parameters such as blade speed and substrate temperature. However, synthesizing a large area and continuous thin film using solution shearing has not been accomplished.

Our first study of this chapter is focused on developing a large area (> cm^2) and continuous thin films of HKUST-1 thin film. HKUST-1 is one of the most well-studied MOFs due to its simple cubic structure and facile synthesis conditions.[11,12] It consists of Cu dimers as nodes and 1,3,5-benzenetricarboxylate (BTC) as linkers.[12,13] HKUST-1 is an insulating MOF, as the porous nature hinders the communication between the π-orbitals of BTC and d-orbitals of Cu(II) dimer, and BTC linkers are carboxylate-terminated molecules.[2,14–16]

The continuous thin film coverage of HKUST-1 is confirmed by incorporating highly conductive molecule (TCNQ) into the HKUST-1 pores to synthesize TCNQ@HKUST-1 composite. As mentioned previously, typical MOFs are inherently insulators. The porous nature of HKUST-1 creates a large spatial gap between organic linkers.[2,17,18] In addition, the terminal group of the linkers in HKUST-1 is a carboxylate group. When the metals are bonded with the carboxylate-based linkers, they form coordination bonds that create a large energy bandgap.[2,17–19] Therefore, if the TCNQ@HKUST-1 thin film is continuous, the charge transfer between electrodes would occur.

Although previous reports have shown the formation of TCNQ@HKUST-1 thin films, no previous publication has shown success in fabricating a large area and continuous

MOF thin film using solution shearing. Producing large area thin films is an important technological milestone to create MOF based electronic applications. Mao *et al*.[20] realized a continuous and well intergrown HKUST-1 membrane within an hour by adhering HKUST-1 seeds on the substrate before the thin film was fabricated, using secondary crystallization to ensure full film coverage. We utilize the same understanding of secondary crystallization to obtain large area and continuous HKUST-1 thin films. The first solution shearing cycle results in the deposition of small HKUST-1 crystallites on the substrate, and subsequent solution shearing cycles lead to a combination of crystal nucleation and growth on the existing HKUST-1 crystallites so that a fully completed thin film is fabricated. After impregnation with TCNQ after the pore activation, we can obtain a conductivity up to 2.4 X 10^{-2} S m^{-1} for the TCNQ@HKUST-1 films. We also find that the oxidation state of copper in HKUST-1 thin film after the solvent exchange process does not reduce to Cu(I). Therefore, these conditions minimize the formation of Cu(TCNQ) as a byproduct so that the pure electrical conductivity of TCNQ@HKUST-1 can be explored. These results show that multiple solution shearing cycles can be utilized to create a large area and continuous thin film MOFs, where the grain boundary between the crystals is lower than those formed by powder impaction. Therefore, multiple solution shearing cycles can be used to improve film coverage.

In addition, as an advancement of the project that is proposed by Dr. Luke Huelsenbeck, the pool-based active learning (PAL) and regression methods are utilized to efficiently guide the solution shearing synthesis of fully covered HKUST-1 thin film with the minimum thickness. The solution sheared HKUST-1 thin film follows deposition regimes relating film thickness, coverage, and crystal size to blade speed.[21,22] As such, by knowing solution concentration, temperature, and blade speed, the film thickness can be

reliably predicted by using models originally developed by Baigl *et al.*[23] However, it is not simple to predict what parameter combinations need to be utilized to fabricate the large area and void free thin films. In such a complex system, it is a daunting process to optimize thin film processing parameters by relying on the skills and experience of researchers. Therefore, by adopting PAL and regression methods, one parameter combination set that provides the fully covered HKUST-1 thin film with a minimum thickness is provided. To confirm its full film coverage, TCNQ is impregnated into the HKUST-1 thin film, and the resulting conductivity is measured to be similar to that of our previous results.[22] Thus, from the synergy between experiments and the PAL approach, we were able to rapidly map the quantitative relationship between the solution shearing coating parameters and HKUST-1 thin film crystallization kinetics by requiring a minimal amount of data collection.

2.4 Materials and Methods

Materials. Copper (II) nitrate hemi(pentahydrate) ($Cu_2(NO_3)\cdot 2.5H_2O$, 98 %), dimethyl sulfoxide (DMSO, 99.99 %), trimesic acid (H_3BTC, 95 %), methanol (≥ 99.9 %), acetone (99.9 %), toluene (99.9 %), anhydrous methylene chloride (≥ 99.8 %), 7,7,8,8-tetracyanoquinododimethane (TCNQ) and trichloro(octadecyl)silane (OTS, ≥ 90 %) were purchased from Sigma Aldrich and were used without additional modification. Glass substrates (1 mm thick), ethanol (200 proof), and isopropyl alcohol were purchased from Fisher Chemical. Silicon wafers, which have a 285 nm thick silicon dioxide layer, were purchased from University Wafer. Gold pellets were obtained from Kurt J. Lesker. The mask for thermal evaporation was manufactured from A-laser.

Substrate Preparation. Glass slides were purchased from Fisher Chemical and used as substrates. Glass slides were cut into approximately 0.5 ” x 1 ”. The glass slides were

sonicated in methanol for 15 minutes. After drying residual methanol from the glass slides by dry airflow, the glass slides were cleaned via UV-ozone for at least 10 minutes.

Coating Blade Fabrication. Silicon wafer was chosen as the coating blade. The wafer was rinsed with toluene, acetone, and isopropyl alcohol. Then, it was put into the UV-ozone cleaner for at least 10 minutes. The wafer was then immediately placed in the crystallization dish that was filled with 0.1 wt. % OTS in toluene. The crystallization dish was covered with the glass lid, and the solution was continued to stir at 50 ℃ overnight. Afterward, those wafers were removed from the dish and sonicated in acetone for 5 minutes. The contact angle of the wafer was checked via deionized water, resulting in a value between 95 ° - 100 °.

HKUST-1 thin film, TCNQ Solution, and TCNQ@HKUST-1 Preparation. Ameloot et al. describe the synthesis of the precursor solution of HKUST-1.[11] Briefly, copper (II) Nitrate hemi(pentahydrate) (5.25 mmol) was stirred with dimethyl sulfoxide (64.0 mmol) until the solution fully dissolved. Trimesic acid (2.76 mmol) was added to the solution and was mixed until it dissolved completely. Once the precursor solution of HKUST-1 was synthesized, HKUST-1 thin film was fabricated via solution shearing. Initially, the coating blade was rinsed with toluene, isopropyl alcohol, and acetone and dried. The blade was held in place with a top vacuum stage and the glass substrate was fixed to a bottom vacuum stage. In the meantime, the substrate stage was heated to the desired temperature. The blade angle and the height between the blade and the substrate were manually controlled by using a micro-manipulating assembly. The HKUST-1 precursor solution was well-mixed and 3 – 8 µL of the precursor solution was injected into the gap between the blade and the substrate. The HKUST-1 thin film was fabricated on the glass substrate as the coating blade moved along the substrate. TCNQ solution was prepared by dissolving TCNQ (60 mg) in

anhydrous dichloromethane (20 mL) under a moisture-free nitrogen-charged glovebox. In the thermal treatment process, the thin film was transferred to the vacuum oven and heated at 120 °C for 10 hours and at 180 °C for two hours afterward. On the other hand, in the solvent treatment process, the thin film was soaked in pure anhydrous dichloromethane for 20 hours and washed the thin film again with another pure anhydrous dichloromethane for four hours. Then, the thin film was heated at 40 °C for two hours to remove the solvent residue. After either treatment, HKUST-1 thin films were immediately transferred to the TCNQ solution and soaked into the TCNQ solution for the desired periods.

Multiple cycles of solution shearing. The solution shearing system was set up using the same procedure as for the first cycle of the HKUST-1 thin film fabrication. After the first solution shearing cycle, the substrate was left on the heated stage for 60 s to allow for the solvent to evaporate. The coating blade was moved to its original position, and 3 - 8 μL of the solution was injected into the gap between the blade and the substrate. The blade was then translated over the substrate again to obtain the second (and subsequent) passes.

Characterizations. XRD patterns were carried out using a Multipurpose PANalytical Empyrean diffractometer (from Malvern Panalytical). An X-ray was generated via Cu K-α radiation that was accelerated by 45 kV and 40 mA. SEM and EDS images were taken by using an FEI Quanta 650 scanning electron microscope. The film thickness was measured using a Bruker Dektak XT Profilometer with a measurement range of 65.5 μm, scan length of 800 μm, duration of 90 s, and stylus force of 10 mg. Film coverage and crystal size of the HKUST-1 thin films with the different processing conditions were observed by using a Zeiss Microscope Axio Scope.A1. The thin film was placed on the stage where condensed light focused on the thin film. Images were taken with 5x, 20x, and 50x objective lenses with the bright field mode. The taken images were quantified by using an image processing

program (Fiji). FT-IR spectra were obtained from a Perkin Elmer Frontier MIR/NIR. PHI Versaprobe III XPS instrument provided Cu 2p peaks of thin films. An X-ray was generated from Al K-α radiation.

Electrical Conductivity Characterizations. Metal evaporation was performed in a glovebox that was produced at LC Technology Solution Inc. Gold metal pellets were thermally evaporated through a shadow mask. 50 nm of the gold layer was deposited as an electrode onto the substrate at a rate of between 1 Å s^{-1} and 1.5 Å s^{-1} at a chamber pressure below 5×10^{-5} mbar inside the glovebox. The channel length was 100 μm, and the electrode width and length were 600 μm and 200 μm, respectively. The current vs. voltage was measured via Keithley 2450 Source Measure Unit (SMU).

Advanced Work from Dr. Luke Huelsenbeck

Pool-based Active Learning (PAL). The objective of active learning is to produce highly accurate classifiers using fewer training data points. This is accomplished by iteratively selecting critical data points from the vast parameter space through the interaction with the solution shearing experiment and optical micrograph characterization. In the PAL methodology, we have an abundance of unlabeled data points. But, labeling these data points is hard, time-consuming, or expensive. In each iteration, the PAL will select a *batch* of data points from the vast, unknown solution shearing parameter space. In this work, our selection criteria for PAL depends on two factors: (1) Uncertainty based on query-by-committee and (2) Diversity based on maximum space-filling design. We first identify data points in the 11 million virtual parameter space that have the predicted probability score (η) between 0.5 and 0.67. The η criterion corresponds to predictions that the thin films are *likely fully covered*. We then use the maximin space-filling design criterion that uses the distance

that maximizes the minimum distance between the training data and the 11 million virtual data points to select a diverse set of 18 data points for experimental validation and feedback.

Classification Learning. The support vector machine (SVM) is a classification learning algorithm that learns to assign labels through the examples given to it.[24] It creates a hyper-plane based on the idea of large margin separation, where it seeks to maximize the distance between the decision boundary and the correctly classified points closest to this boundary. In this work, the SVM models are trained to predict the binary classification learning problem of full coverage vs lack of full coverage for each data point. The important factors in SVM are the hyperplane, kernel, and hyperparameters. The hyperplane is the dividing barrier between conditions that have led to full coverage and lack of full coverage. The hyperplane can be mathematically described in classification learning as,

$$f(x) = sign(\langle \boldsymbol{w}, \phi(\boldsymbol{x}) \rangle + \boldsymbol{b}) \text{ (Equation. 2)}$$

where **x** is a vector of input descriptors (solution shearing parameters), **w** are weight coefficients that fit the training data, and $\mathbf{b} \in \mathbb{R}$ is the intercept. The kernel function (κ) allows to apply mathematical operations on the hyperplane to better situate it according to the training data points. For our classification learning, we used a Gaussian radial basis kernel function as shown below.

$$\kappa(x, x') = \exp(-\|x - x'\|^2 / 2\boldsymbol{\sigma^2}) \quad \text{(Equation. 3)}$$

Finally, the other factors important in constructing these models are hyperparameters, which control how the model considers the support vectors. We have two hyperparameters to optimize: (1) The $\boldsymbol{C}$ -parameter (cost) evaluates penalty. A larger $\boldsymbol{C}$ -value will assign a higher penalty to errors. (2) The $\boldsymbol{\sigma}$-parameter evaluates how much each support vector influences the surrounding space. We determined the hyperparameters, $\boldsymbol{C}$, and $\boldsymbol{\sigma}$, by cross-

validation (CV) from the training data to balance the bias-variance tradeoff. The hyperparameters that minimize the CV error are used for the final model. We performed this hyperparameter tuning procedure each time when we built an SVM model.

Regression. We employ the support vector regression (SVR) as our ML method for regression to predict the thickness of fully covered thin films.[25] In general, an SVR is of the form

$$f(\mathbf{x}) = \langle \mathbf{w}, \mathbf{x} \rangle + \mathbf{b}, \quad \text{(Equation. 4)}$$

where **x** is a vector of descriptors, **w** are coefficients that fit the training data, and **b** is the intercept, derived via the following optimization routine:

$$\min \frac{1}{2} \|\mathbf{w}\|^2 + \mathbf{C} \sum_{i=1}^{n} (\boldsymbol{\xi}_i + \boldsymbol{\xi}_i^*) \qquad \text{(Equation. 5)}$$

$$\text{subject to } \begin{cases} f(\mathbf{x}) - \langle \mathbf{w}, \mathbf{x}_i \rangle - \mathbf{b} \leq \in + \boldsymbol{\xi}_i \\ \langle \mathbf{w}, \mathbf{x}_i \rangle + \mathbf{b} - \boldsymbol{f}(\mathbf{x}) \leq \in + \boldsymbol{\xi}_i^* \\ \boldsymbol{\xi}_i, \boldsymbol{\xi}_i^* \geq \mathbf{0} \end{cases}$$

where $\mathbf{C}$ is the regularization term, *n* is the total number of data points, $\in$ is the insensitive tube around the target values that provides the magnitude of the amount of permitted error (only those target values greater than $\in$ are penalized by the optimization), $\boldsymbol{\xi}_i, \boldsymbol{\xi}_i^*$ are the nonnegative slack variables that permit a certain level of violation of the $\in$-tube bounds, and $\mathbf{x}_i$ is the descriptor for the i^{th} training data. The regularization term $\mathbf{C}$ balances the model complexity and training error (large $\mathbf{C}$ and small $\mathbf{C}$ can lead to overfitting and underfitting, respectively). For a linear SVR, the kernel function, $\langle \mathbf{w}, \mathbf{x} \rangle$, is a dot product of **x** and $\mathbf{x}_i$, leading to a $\boldsymbol{f}(\mathbf{x})$ that is linear in **x**. In this work, we use the nonlinear Gaussian radial basis function of the form:

$$\boldsymbol{\kappa}(\mathbf{x}, \mathbf{x}') = exp\left(-\frac{\|\mathbf{x}-\mathbf{x}'\|^2}{2\boldsymbol{\sigma}^2}\right) \quad \text{(Equation. 6)}$$

We determined the hyperparameters, $\mathbf{C}$, and $\boldsymbol{\sigma}$, by 10-fold CV.

Bootstrap resampling. Since our training data sets (for both classification learning and regression) were only a small sample of the population, we lack complete information on the probability distribution of model parameters. This introduces uncertainty in quantifying the model output distribution. Therefore, estimating the error rate (or error bar) for each prediction is as important as estimating the mean prediction itself. We utilized the bootstrap resampling method for uncertainty quantification, which is especially suited for problems with small training data.[26] The idea behind the bootstrap resampling method is to randomly draw *samples with replacement* from the training set to generate a large number of "pseudo training sets." Certain observations may appear multiple times (due to sampling with replacement), whereas other observations may not appear at all in the pseudo training sets. These data points are referred to as out-of-bag samples. An ensemble of ML models will then be trained using the pseudo training sets generated by the bootstrap method. The performance of the trained ensemble of models is evaluated on the out-of-bag samples. In the case of SVM, the probability score, η, is used as a metric for uncertainty. In the case of SVR, the mean and standard deviation of the predictions from the ensemble of models is then used as an estimate of the expected thickness and its associated uncertainty, respectively.

2.5 RESULTS AND DISCUSSION

2.5.1 Fabrication of a large area and continuous HKUST-1 thin film via solution shearing

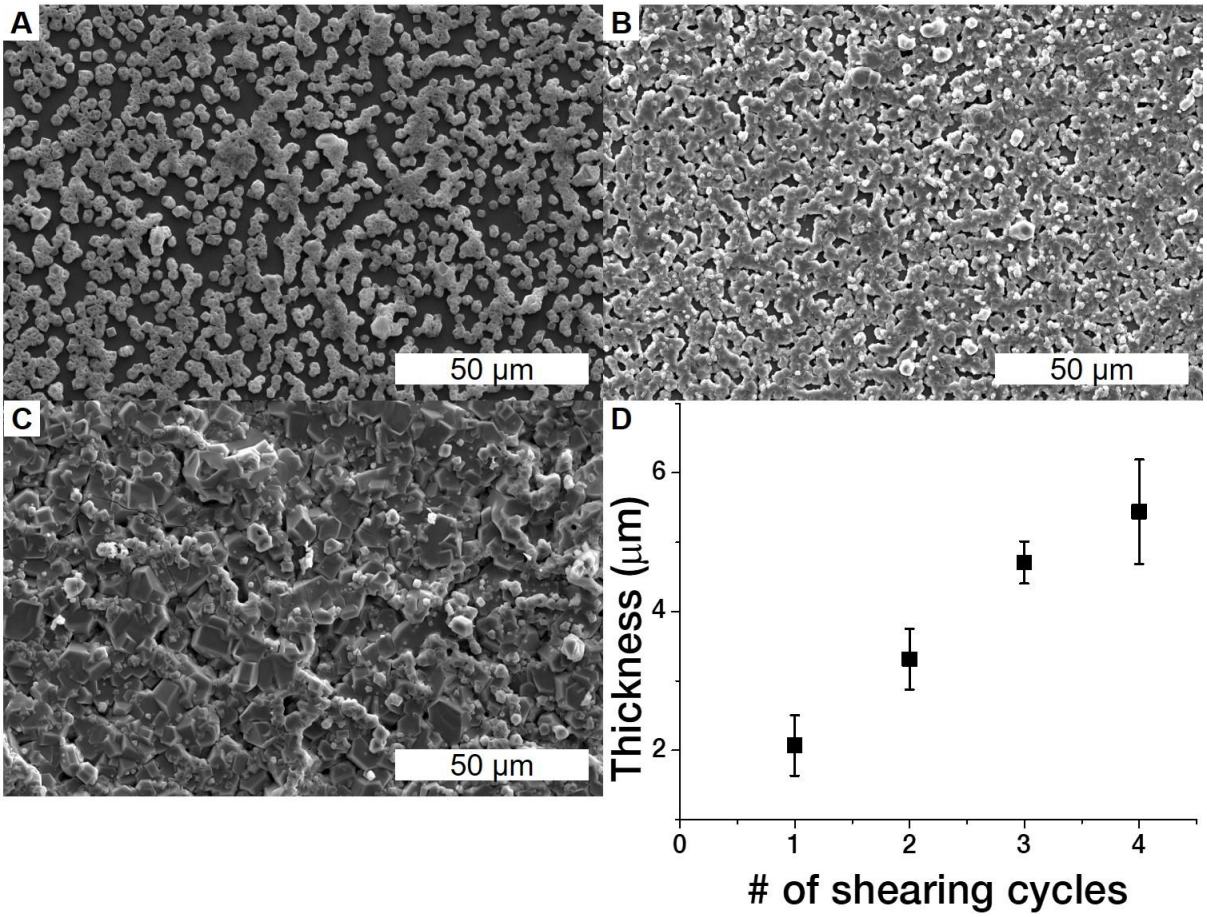

Figure 2. 2. SEM images of **(A)** 1st, **(B)** 2nd and **(C)** 4th solution-shearing cycles of HKUST-1. Increasing the number of solution-shearing cycle results in increasing the film coverage of HKUST-1on the substrate. After the 4th cycle, we observed complete film coverage. The darker backgrounds that are shown in the 1st and 2nd cycles represent the substrate. The darker background in the 4th cycle is observed due to the color contrast, originating from the stacked HKUST-1 crystals that are grown from previous solution shearing cycles. (**D)** The film thickness of solution-sheared HKUST-1 increases with the number of solution-shearing cycle (n = 3).

During the solution shearing process, the HKUST-1 thin film was cast at 160 °C with a coating speed of 0.5 mm s^{-1}, with dimethylsulfoxide (DMSO) as the solvent.[11] These parameters were utilized because they provided a thin film with high film coverage and uniform crystal size distribution in one cycle (**Figure A2. 1)**. As the coating speed increases or the temperature of the substrate decreases, the HKUST-1 thin film coverage decreases. However, as shown in **Figure 2. 2A**, the HKUST-1 thin film that is fabricated after one

solution shearing cycle is a not fully covered thin film since neither the nucleation rate nor the growth rate of HKUST-1 is enough to fully cover the substrate (**Figure A2. 2)**. As mentioned earlier, obtaining a continuous thin film is chosen as the most important parameter to increase the electrical conductivity of the TCNQ@HKUST-1 over large areas, as grain boundaries and pinholes can cause orders of magnitude reduction in charge transport.[27,28]

To fabricate continuous HKUST-1 thin films, we performed multiple cycles of solution shearing. We hypothesize that HKUST-1 seed crystals form on the substrate after the first solution shearing cycle, and in the subsequent shearing cycle, secondary crystallization and crystal growth occurs on these crystals, and new nuclei also form on the substrate, leading the HKUST-1 thin film to be fully covered on the substrate (**Figure A2. 3 and Figure A2. 4**).

Subsequent solution shearing cycles were performed after the remaining precursor solution evaporated from the substrate (60 seconds between each pass). Due to the large parameter space afforded by solution shearing, the time between solution shearing passes, or the shearing speed of each pass, was not varied.

The film coverage was quantified using an image processing program (Fiji) as depicted in **Table A2. 1**. Increasing the number of solution shearing cycles monotonically increases the area of thin film coverage, reaching a value of 99 ± 0.6 % at the 4^{th} solution shearing cycle.

As the coverage increases, we also see evidence of intergrowth between crystal domains indicating fewer grain boundaries (**Figure A2. 4**). New crystal growth occurs from the surface of previous HKUST-1 crystals present on the substrate. These secondary crystallization events are advantageous as the two or more crystals share a crystal plane,

ensuring that no void-like grain boundaries exist at that interface. These shared crystal planes morphologies occur due to multiple solution shearing cycles. Typically, when the solvent of the precursor solution contacts the thin film for more than 5 minutes, the thin film can dissolve. However, as the crystallization of the HKUST-1 thin film using solution shearing occurs within a minute, minimal dissolution was observed from the previous HKUST-1 on the substrate due to the rapid solvent evaporation.[9,29] The rapid evaporation leads to rapid primary and secondary nucleation and crystal growth, leading to the formation of intergrown HKUST-1 crystals and an increase in the film coverage. No void regions are observed down to the resolution of the Scanning Electron Microscope (SEM) and EDS (**Figure 2. 2C and Figure A2. 3**).

As indicated in **Figure A2. 5**, X-ray diffraction (XRD) shows that solution sheared HKUST-1 matches closely with the solvothermal HKUST-1 and retains its crystallinity even if multiple solution shearing cycles are performed. The film thickness also evolves with multiple cycles (**Figure 2. 2D**). The thickness of the HKUST-1 thin film after the 1st solution shearing cycle, which is 2.1 ± 0.4 µm, is similar to that of the reported value from

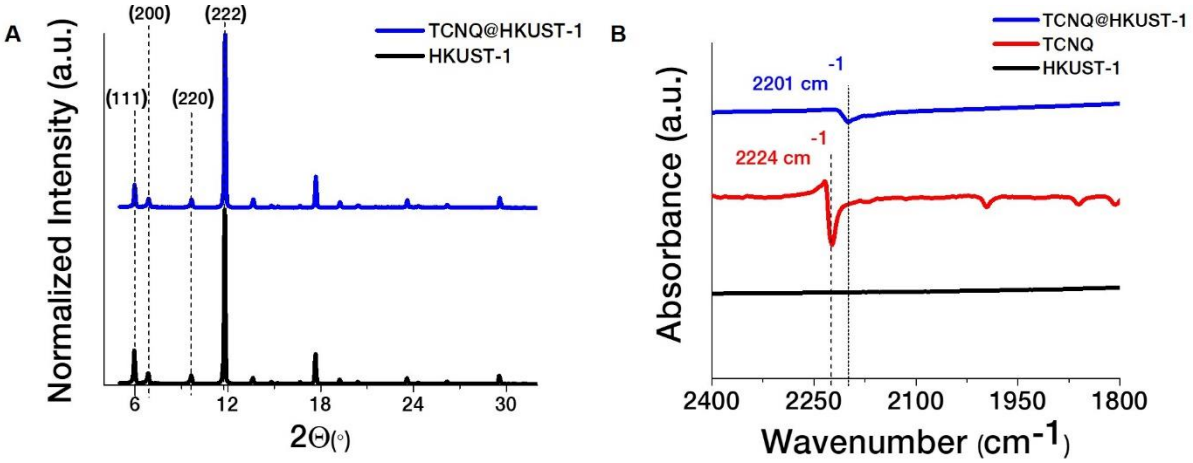

Figure 2. 3. A. X-ray diffraction (XRD) pattern shows the crystal structure remains consistent even if the TCNQ molecules are loaded on the solution sheared HKUST-1 thin film. **B.** Fourier Transform-Infrared (FT-IR) spectra of TCNQ@HKUST-1, TCNQ, and HKUST-1. The peak that represents nitrile group is shifted from 2,224 cm^{-1} to 2201 cm^{-1} due to the bonding between OMS and nitrile group.

Lee *et al*.[9] which is in the range of 2 μm – 4 μm. After the 4th solution shearing cycle, the average thickness of the HKUST-1 film is 5.4 ± 0.8 μm, increasing by an average of 1.2 μm per cycle. Given that the four cycles provided full coverage, we used these films as the platform to measure the electrical conductivity of films with different TCNQ loading times.

2.5.2 TCNQ Infiltration on the Continuous HKUST-1 Thin Film

TCNQ@HKUST-1 samples were created by soaking HKUST-1 thin films in a saturated TCNQ solution, dissolved in anhydrous dichloromethane (CH_2Cl_2), as performed in previous reports.[2] Before the HKUST-1 thin film was soaked into TCNQ solution, the film was washed by soaking in pure CH_2Cl_2 to remove solvent residue and to evacuate the HKUST-1 pores, creating the OMS inside the HKUST-1 pores. **Figure 2. 3A** shows the XRD patterns of TCNQ@HKUST-1 as well as the pristine HKUST-1 synthesized using solution shearing. Schneider *et al*.[30] demonstrated that Cu(TCNQ) may form on the HKUST-1 surface during TCNQ loading. As shown in **Figure 2. 3A**, XRD patterns stay consistent even after TCNQ loading, and no unique peaks characteristic of Cu(TCNQ) appear, indicating that TCNQ is loaded into the HKUST-1 thin film without forming Cu(TCNQ), down to the resolution of XRD. Recently, Kim *et al*.[1] demonstrated that anhydrous methylene chloride (CH_2Cl_2) can remove solvent residue and water molecules inside HKUST-1 pores without applying heat. This solvent exchange showed comparable activation performance to the thermal treatment, and the copper reduction to Cu(I) was not observed. We hypothesize that the solvent activation process limits the formation of Cu(TCNQ) in our system.

TCNQ binding to the OMS in the HKUST-1 thin film is confirmed by using Fourier-Transform Infrared spectroscopy (FT-IR). As shown in **Figure 2. 3B**, a nitrile stretch peak in TCNQ is observed at 2,224 cm^{-1}, but the nitrile peak in TCNQ@HKUST-1 is shifted to 2,201 cm^{-1}.[2] This peak shift occurs due to the bonding between the lone pair of the nitrile group in TCNQ and the OMS in the HKUST-1 thin film.

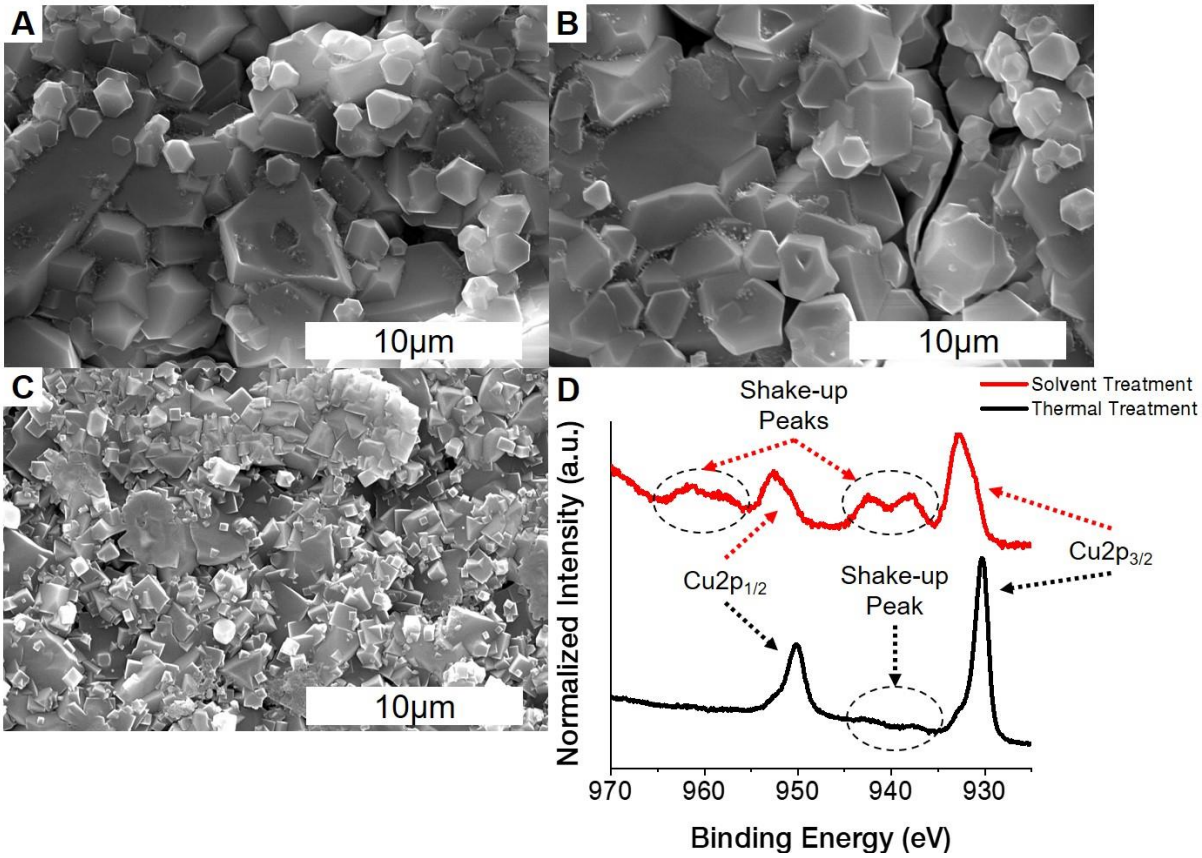

Figure 2. 4. SEM images of **(A)** Pristine HKUST-1, **(B) – (C)** 24hrs and 168hrs TCNQ@HKUST-1, respectively. The crystal morphology of HKUST-1 is preseved without forming a worm-shaped byproduct, Cu(TCNQ). **D.** XPS of solvent treated and thermal treated TCNQ@HKUST-1. Thermally treated HKUST-1 thin film reduces the oxidation state of copper as shown by the lack of shake up peaks. Cu (II) is dominated in the solvent exchanged HKUST-1 by showing strong satellite shake-up peaks as indicated by circles.

According to Schneider *et al.*[19], thermal treatment to remove solvent residue and water molecules in the HKUST-1 pores causes the surface morphology of HKUST-1 to change as Cu(II) in HKUST-1 reduces to Cu(I). The presence of Cu(I) atoms causes the formation of Cu(TCNQ) as a byproduct when the HKUST-1 thin film is soaked in TCNQ. Crystals with worm-shaped morphology represent the formation of Cu(TCNQ) (**Figure A2.**

6). According to Schneider et al[31], these nanowires indicate the formation of Cu(TCNQ) phase I as a byproduct. Due to the formation of Cu(TCNQ), which has two different phases, the pure effect of the electrical conductivity of TCNQ@HKUST-1 is hard to determine. The Cu(TCNQ) formation hinders the electrical conductivity of TCNQ@HKUST-1. Heintz et al.[33] demonstrated that Cu(TCNQ) phase 1 is the semiconducting material with an electrical conductivity of 25 S m^{-1}. On the other hand, the electrical conductivity of phase 2 is close to 0.0013 S m^{-1}.[33] To avoid this convoluting effect, solvent treatment using CH_2Cl_2 was used to minimize the formation of Cu(TCNQ).[1] As depicted in **Figure 2. 4**, the crystal morphology of solvent exchanged TCNQ@HKUST-1 does not show the worm-like morphology that indicates the formation of Cu(TCNQ).

Scanning X-ray photoelectron spectrometry (XPS) was used to observe the oxidation state of the TCNQ@HKUST-1 thin film. The oxidation state of copper in Cu(TCNQ) is Cu(I) while that of copper in TCNQ@HKUST-1 is Cu(II). **Figure 2. 4D** shows the Cu 2p peak of pristine HKUST-1 under a solvent treatment and a thermal treatment. The existence of satellite features in the Cu 2p peak represents a ligand-metal charge transfer. These satellite peaks are called "shake-up" peaks, and they are key peaks that determine the oxidation state of copper since Cu(I) and Cu(II) exhibit different strengths and shapes of the "shake-up" peak.[34,35] As seen in **Figure 2. 4D**, thermally treated pristine HKUST-1 reduces the oxidation state from Cu(II) to Cu(I) and removes the shake-up peaks. These features match closely with the XPS peak of Cu(I).[36] However, since the average depth of the XPS measurement is around 5 nm, the entire copper metals in the HKUST-1 thin film may not be reduced to Cu(I). On the other hand, the XPS spectrum of solvent exchanged HKUST-1 is shifted by 2 eV, and there are two strong satellites observed around 945 eV, and another strong satellite is observed around 965 eV. These three satellites show that

Cu(II) in TCNQ@HKUST-1 does not reduce to Cu(I). Therefore, the formation of Cu(TCNQ) may be minimized when TCNQ is loaded on the solvent exchanged HKUST-1 thin film.

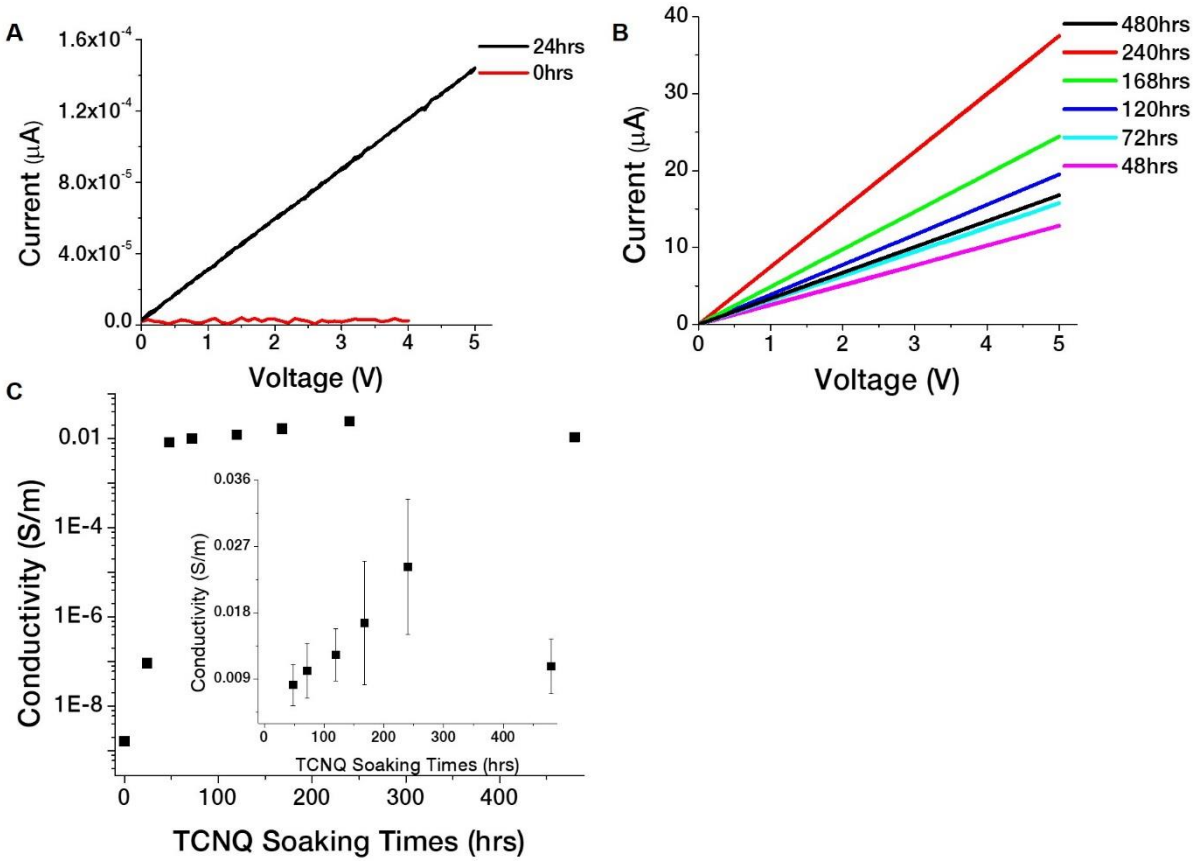

Figure 2. 5. A-B. I-V curve of TCNQ@HKUST-1 with different TCNQ soaking time. As the soaking time increases, more TCNQ molecules have higher chance to bind to the HKUST-1 which increases the current of TCNQ@HKUST-1. **C.** The electrical conductivity of TCNQ@HKUST-1 with different TCNQ soaking time. As the TCNQ soaking time increases, the electrical conductivity of TCNQ@HKUST-1 increases up to seven orders of magnitude. Inset shows conductivity data after TCNQ was soaked for 48 hours (n=4).

Current-voltage (I-V) measurements of TCNQ@HKUST-1 films with different TCNQ loading times up to 480 hours were used to obtain the conductivity (**Figure 2. 5A - B).** The pristine HKUST-1 does not exhibit any current response due to its insulating nature.[18,19,37,38] As the TCNQ infiltration time increases, the current of TCNQ@HKUST-1 increases with a linear I-V curve. The electrical conductivity is shown in **Figure 2. 5C**. The electrical conductivity increases seven orders of magnitude as the TCNQ soaking time increases. Previously, Talin *et al.*[2] calculated 7 S m^{-1} of electrical conductivity after

HKUST-1 thin film was exposed to TCNQ solution. Compared with this value, solution sheared TCNQ@HKUST-1 under the same TCNQ loading time has two orders of magnitude lower electrical conductivity. We hypothesize that the low electrical conductivity in solution sheared TCNQ@HKUST-1 occurs due to the higher film thickness of solution sheared TCNQ@HKUST-1. Since solution sheared HKUST-1 thin films are thicker than solvothermal grown HKUST-1 thin films, it takes longer for TCNQ to diffuse into solution sheared HKUST-1 thin films, leading to the lack of well-coordinated TCNQ in the OMS of the solution sheared HKUST-1 thin film. However, solution sheared TCNQ@HKUST-1 thin film has higher electrical conductivity than the pressed TCNQ@HKUST-1 pellet as solution sheared TCNQ@HKUST-1 thin film has less grain boundaries than the pressed pellet.[19] The conductivity increased with TCNQ soaking time up to 240 hrs but decreased after the film was soaked for 480 hours, owing to HKUST-1 thin film degradation, resulting from long TCNQ soaking.

2.5.3 Optimization of the Large-area and Continuous HKUST-1 Thin Film Using Active Learning

In addition, as an advancement of the project that is proposed by Dr. Luke Huelsenbeck, TCNQ was impregnated to further demonstrate the utility of the machine learning (ML) guided film optimization approach. Briefly, 11 million virtual parameter space was identified using the PAL approach. Among these large parameter spaces, we explored the combination parameter sets that provide a fully covered HKUST-1 thin film (**Figure A2. 7**) and determined one parameter set with having minimum film thickness as well as showing a full coverage. 6 passes and 3.5 mm/s for a copper concentration of 1 M, metal to linker ratio of 1.8, and substrate temperature of 165 ℃ is the parameter

combination that provides a full film coverage with a minimum film thickness of 2.2 ± 0.3 μm. The optimized thickness value determined by the PAL process is approximately 2.5 less than the experimentally optimized thickness. Furthermore, we compared the electrical performance of TCNQ@HKUST-1 films optimized experimentally and by the ML model. **Figure 2. 6A and B** show the I-V response of the thin films and the conductivity of the films, respectively. We found the conductivity of the ML optimized film matched that of the experimentally optimized film at 2.1 ± 1.5 x 10^{-2} S/m and 2.4 ± 0.9 x 10^{-2} S/m, respectively (**Figure 2. 6B**). Maintaining conductivity while reducing film thickness shows the conservation of film continuity without the introduction of void spaces in the ML optimized film, as grain boundaries have been shown to reduce the conductivity of crystalline thin films.[39] We hypothesize that the maintained conductivity and 2.5 fold reduction in thickness will yield accelerated response times for sensor applications while the fully covered film can act as a separations barrier or as a selective coating.

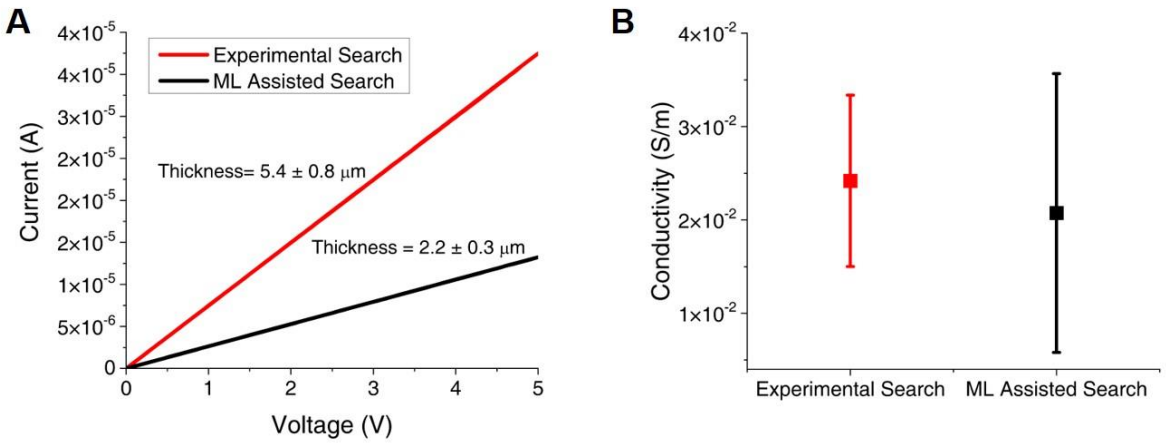

Figure 2. 6. A. I-V curve showing electrical performance of SVR minimized thickness film and experimentally minimized thickness film and **B.** conductivity of these films (n =6).

2.6 Conclusion

In summary, solution shearing with multiple cycles can rapidly fabricate large area HKUST-1 thin films with consistent thin film thickness and no pinholes due to a secondary crystallization event. The XRD pattern of solution sheared HKUST-1 thin films shows that multiple solution shearing cycles do not affect the chemical structure of HKUST-1. By incorporating TCNQ molecules into the OMS inside the HKUST-1 pores, a conductive composite called TCNQ@HKUST-1 can be created. SEM images and XPS spectra of TCNQ@HKUST-1 confirm that solvent treatment can activate the pores of HKUST-1 without reducing the oxidation state of copper, which corresponds to the minimization of Cu(TCNQ) formation. Furthermore, I-V measurements indicate that the electrical conductivity of TCNQ@HKUST-1 reaches up to seven orders of magnitude higher than that of pristine HKUST-1.

In addition, by leveraging the PAL method, we synthesize a HKUST-1 thin film that has fully covered and minimum film thickness. The thickness of the thin film using this approach is 2.5 times smaller than the minimum thickness obtained by an experimentally optimized thin film. To confirm its full coverage, TCNQ molecules are incorporated into the HKUST-1 thin film. If the film is continuous, a linear current-voltage curve would be obtained. If not, the electrical characteristic of the thin film would be shown an insulating character. The electrical conductivity of the films using the PAL approach matched that of the previously obtained TCNQ@HKUST-1 film by us, indicating that the electrical conductivity can be preserved while making thinner films. To the best of our knowledge, this is the first instance of using active learning techniques to fabricate MOF thin films, and this finding expands the applicability of MOF thin films that are fabricated via flow coating techniques such as chemresistive sensors or electrodes in supercapacitors.

2.7 Chapter 2 Appendices

Determination of the solution shearing parameters that affect the film coverage

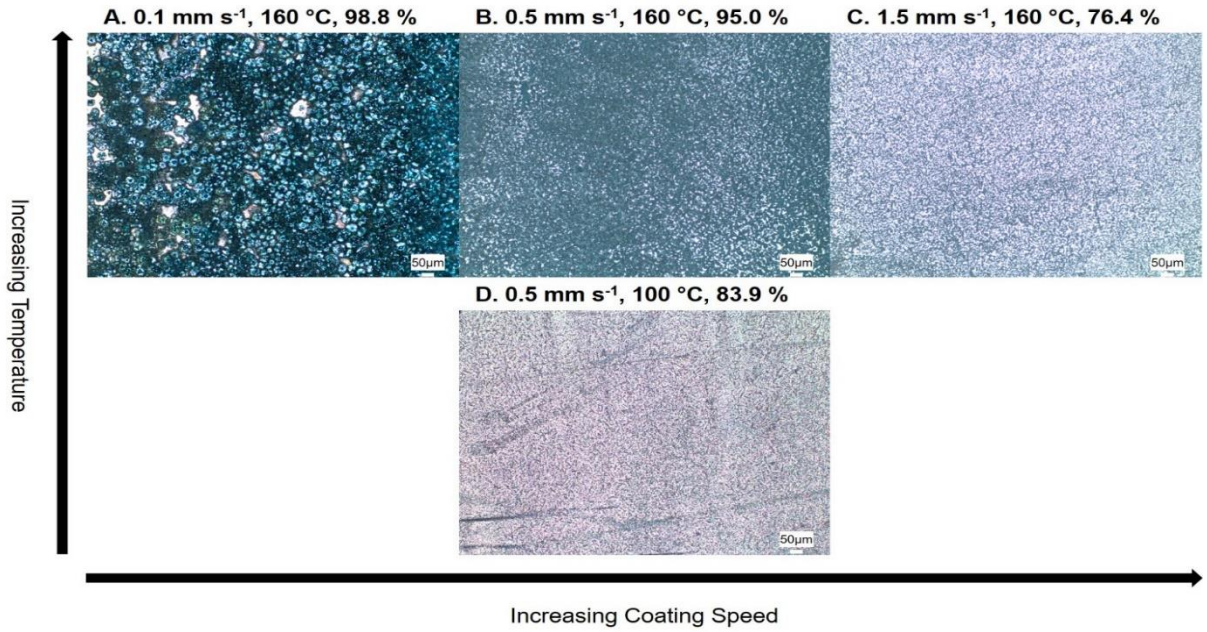

Figure A2. 1. The optical images and the percentages that represent the film coverage with varying the heated substrate temperature and the coating speed. As the speed increases and temperature decreases, the size of the HKUST-1 and film coverage decreases. The white background represents the substrate and the film coverage was quantified using Fiji.

Energy Dispersive Spectroscopy (EDS) image between 1st and 4th solution sheared HKUST-1 thin film

- **1st Solution sheared HKUST-1 thin film**

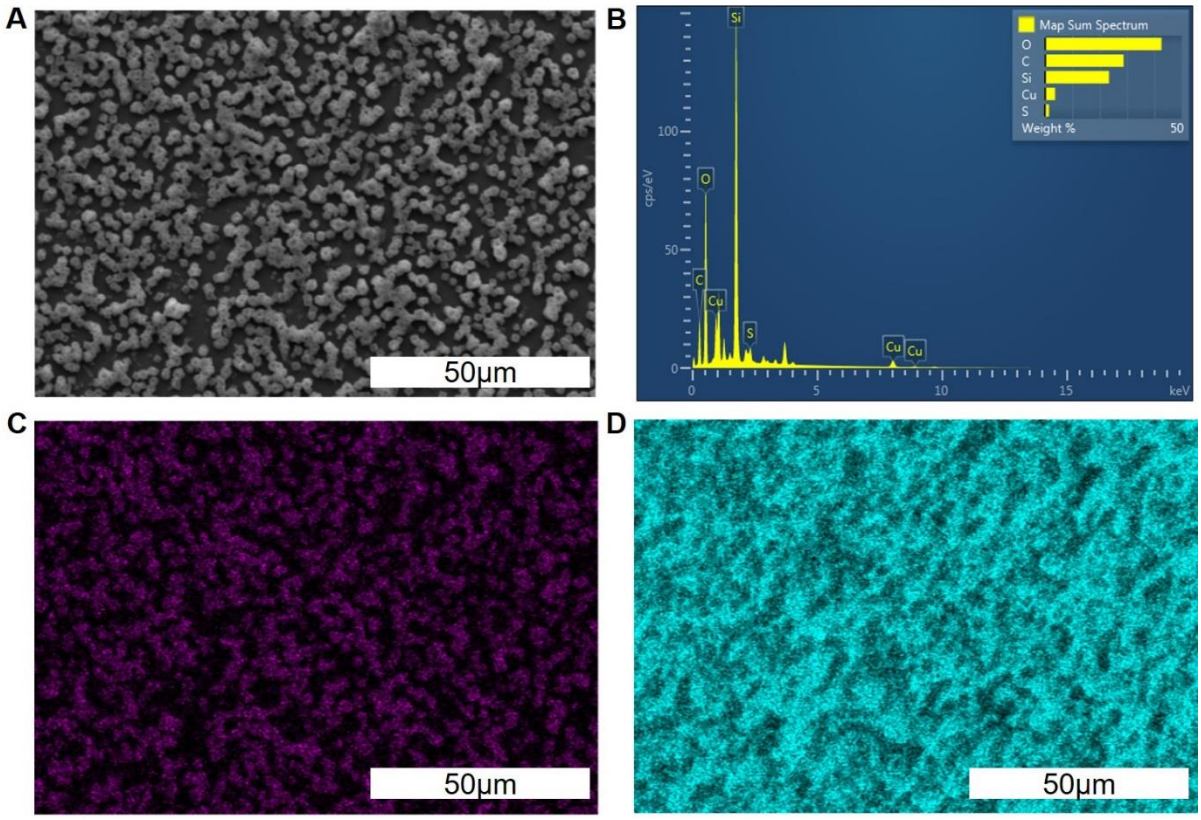

Figure A2. 2. A. SEM image of 1st solution sheared HKUST-1 thin film. **B.** The elemental composition of 1st solution sheared HKUST-1 thin film. **C.** Copper (Cu) atom distribution in the HKUST-1 thin film. **D.** Silicon (Si) atom distribution in the HKUST-1 thin film. As can be seen in this image, the composition of Si is higher than that of Cu.

- **4th Solution sheared HKUST-1 thin film**

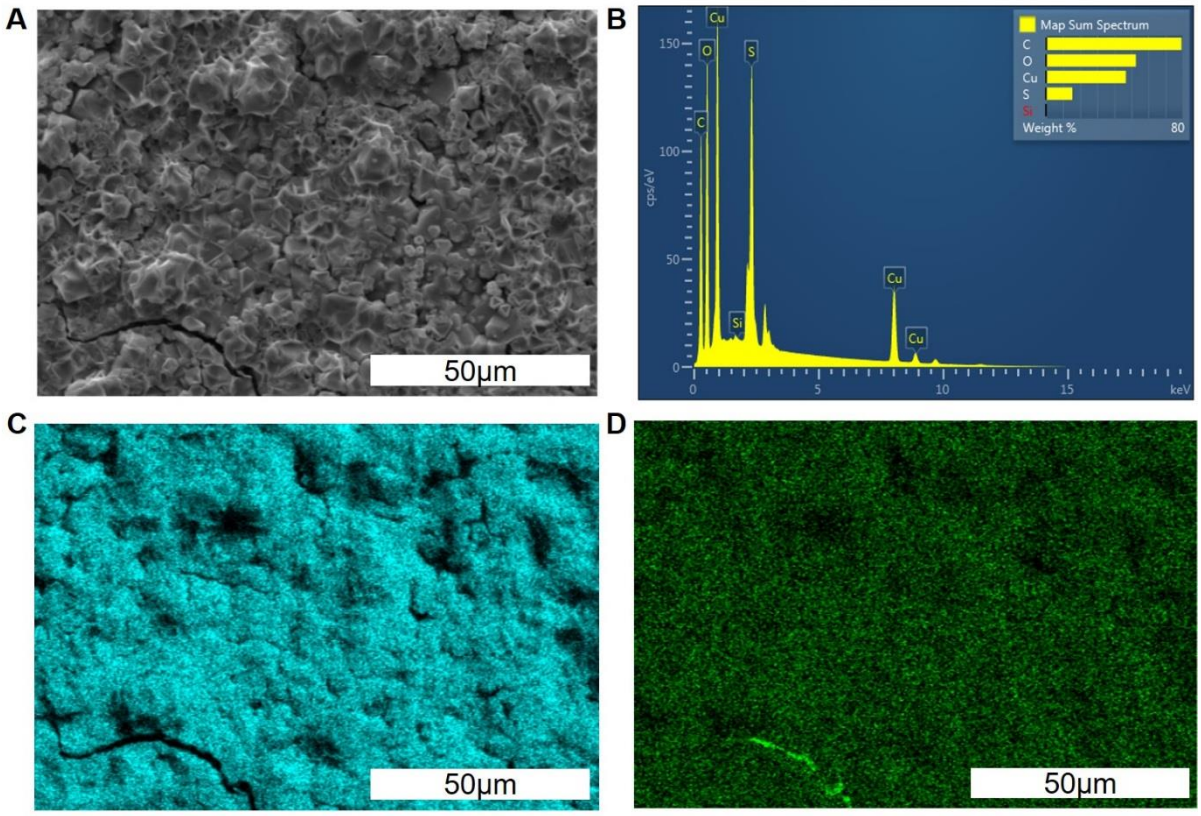

Figure A2. 3. A. SEM image of 4th solution sheared HKUST-1 thin film. **B.** The elemental composition of 1st solution sheared HKUST-1 thin film. **C.** Copper (Cu) atom distribution in the HKUST-1 thin film. **D.** Silicon (Si) atom distribution in the HKUST-1 thin film. As can be seen in this image, the composition of Si is low, compared to the abundance of Si seen in the region with a crack on the lower left of the image. This corresponds that HKUST-1 thin film is completely covered via multiple cycles of solution shearing. The dark spot in **C** and **D** occurs due to the rough film thickness which EDS detector cannot detect elements on the film.

Intergrown HKUST-1 crystals that are originated from the multiple cycles of solution shearing

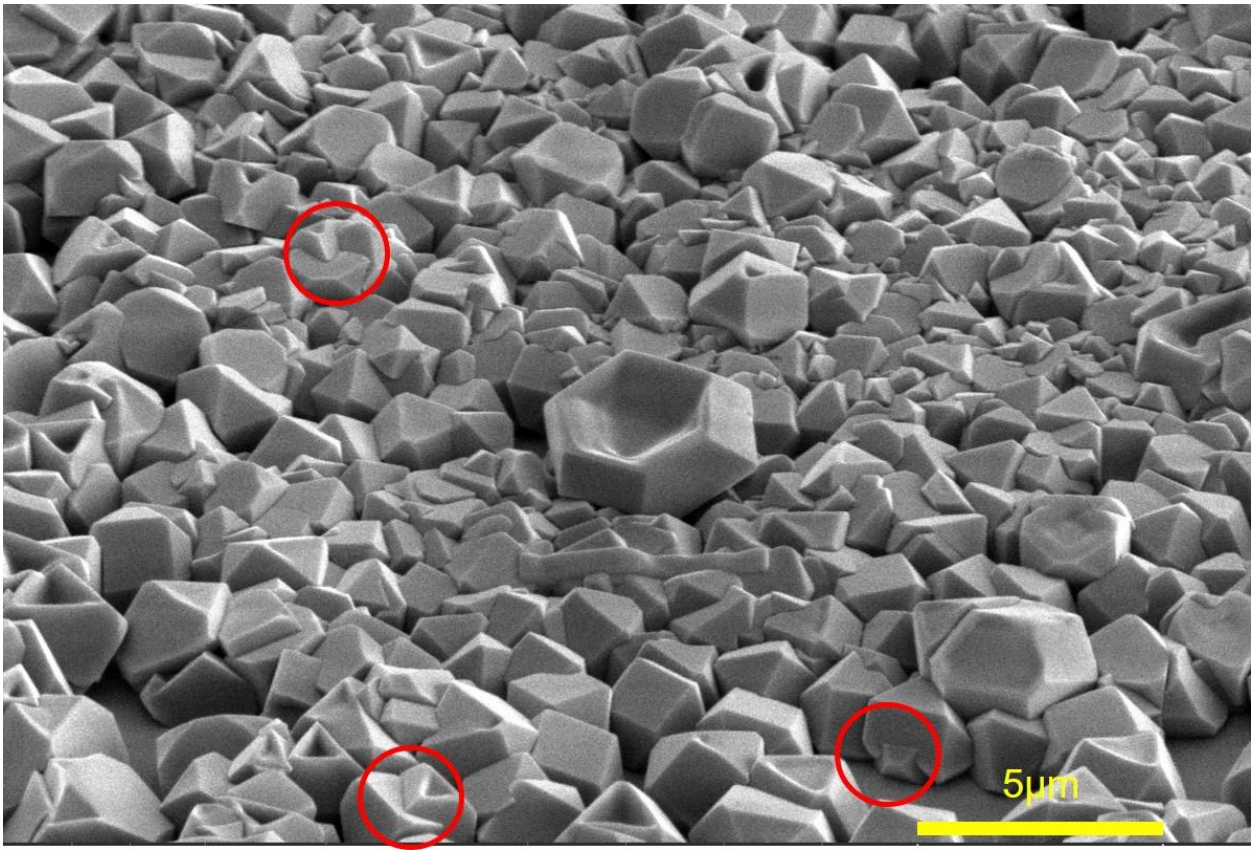

Figure A2. 4. Due to the multiple solution shearing processes, HKUST-1 crystal shares their crystal plane with neighbor crystals as indicated by the red circles.

Film coverage quantification

Table A2. 1. Quantified film coverage with the different number of solution shearing cycles. As the number of solution shearing cycle increases, the film coverage increases. When the solution shearing process was performed four times, the film coverage nearly reaches to 100%.

Number of Solution Shearing Cycle	Film Coverage (%)
1st Cycle	60 ± 1.1
2nd Cycle	80 ± 0.9
3rd Cycle	89 ± 0.7
4th Cycle	99 ± 0.6

XRD patterns of solvothermal HKUST-1 and solution sheared HKUST-1 to confirm the formation of HKUST-1

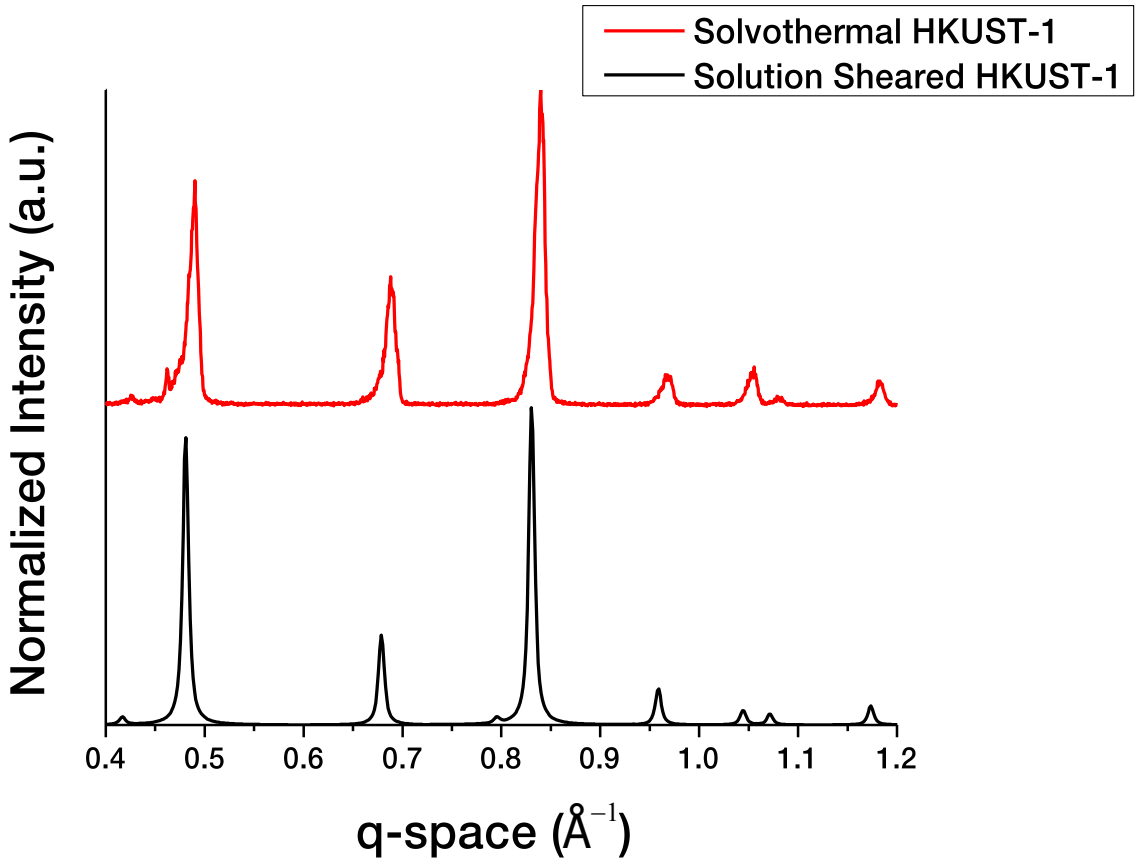

Figure A2. 5. The XRD peak comparison between solution sheared HKUST-1 and solvothermal HKUST-1. Solution sheared peaks match closely with the solvothermal HKUST-1.

Change in surface morphology of TCNQ@HKUST-1 thin film when the HKUST-1 thin film is removed its impurity by applying heat

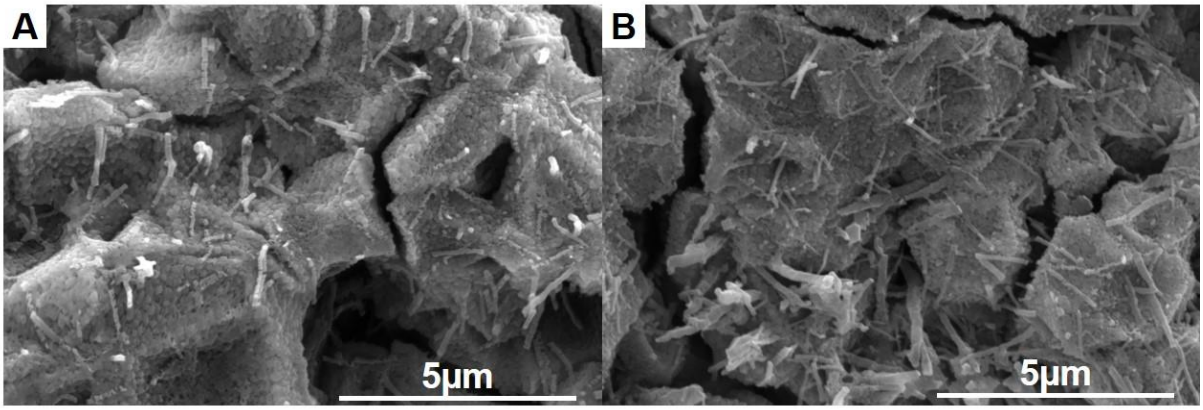

Figure A2. 6. (A) – (B) SEM images of thermally activated 72 hrs and 168 hrs of TCNQ@HKUST-1. Numerous nanowire crystals appear on the surface of the HKUST-1 thin film after the substrate is soaked in TCNQ solution for 72 hours. These molecules represent the formation of the Cu(TCNQ) as a side product.

Surface morphology of fully covered and solution sheared HKUST-1 thin film that is created by using active learning

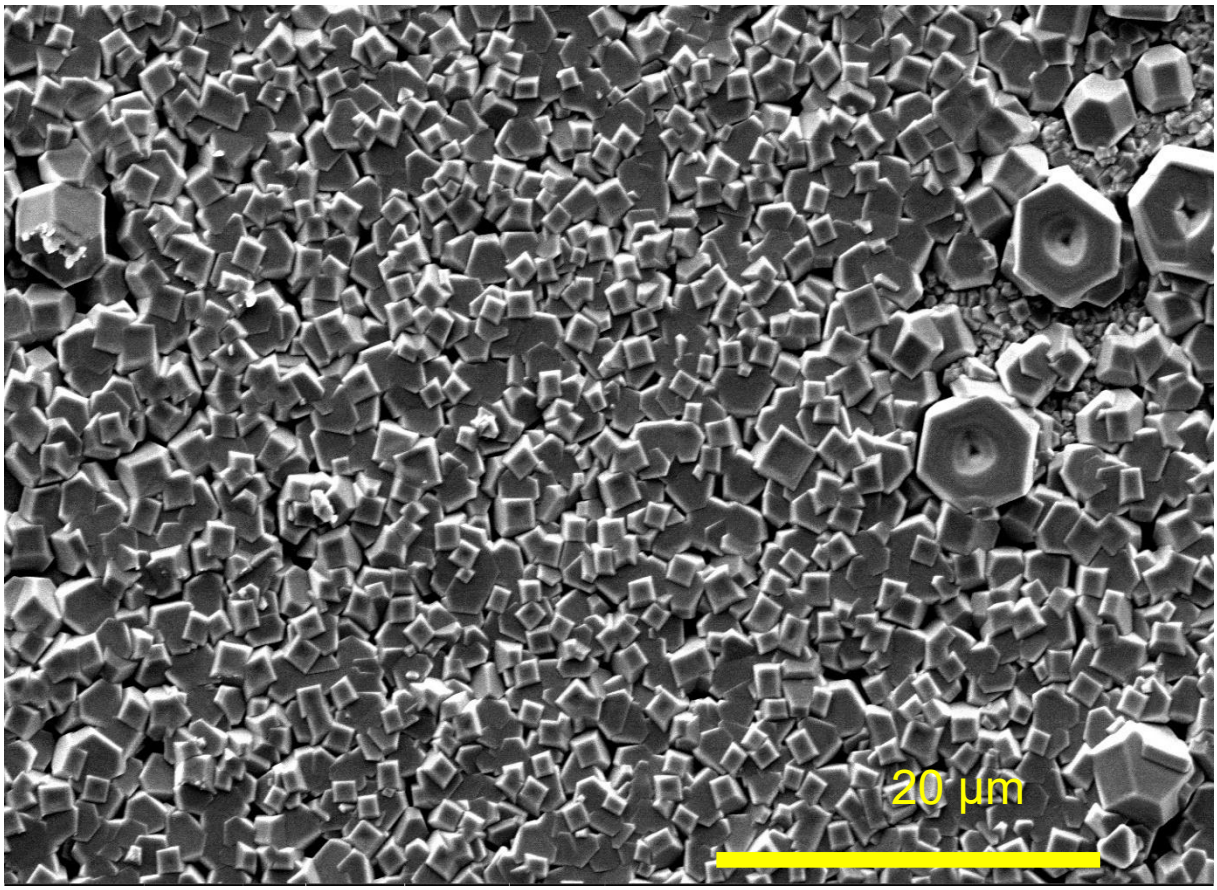

Figure A2. 7. The SEM image of the fully covered HKUST-1 film that the parameters were provided using active learning.

2.8 References

(1) Kim, H. K.; Yun, W. S.; Kim, M.-B.; Kim, J. Y.; Bae, Y.-S.; Lee, J.; Jeong, N. C. A Chemical Route to Activation of Open Metal Sites in the Copper-Based Metal–Organic Framework Materials HKUST-1 and Cu-MOF-2. *J. Am. Chem. Soc.* **2015**, *137* (31), 10009–10015. https://doi.org/10.1021/jacs.5b06637.

(2) Talin, A. A.; Centrone, A.; Ford, A. C.; Foster, M. E.; Stavila, V.; Haney, P.; Kinney, R. A.; Szalai, V.; El Gabaly, F.; Yoon, H. P.; Léonard, F.; Allendorf, M. D. Tunable Electrical Conductivity in Metal-Organic Framework Thin-Film Devices. *Science* **2014**, *343* (6166), 66–69. https://doi.org/10.1126/science.1246738.

(3) Hermes, S.; Schröder, F.; Chelmowski, R.; Wöll, C.; Fischer, R. A. Selective Nucleation and Growth of Metal−Organic Open Framework Thin Films on Patterned COOH/CF_3-Terminated Self-Assembled Monolayers on Au(111). *J. Am. Chem. Soc.* **2005**, *127* (40), 13744–13745. https://doi.org/10.1021/ja053523l.

(4) Horcajada, P.; Serre, C.; Grosso, D.; Boissière, C.; Perruchas, S.; Sanchez, C.; Férey, G. Colloidal Route for Preparing Optical Thin Films of Nanoporous Metal-Organic Frameworks. *Adv. Mater.* **2009**, *21* (19), 1931–1935. https://doi.org/10.1002/adma.200801851.

(5) Shekhah, O.; Wang, H.; Kowarik, S.; Schreiber, F.; Paulus, M.; Tolan, M.; Sternemann, C.; Evers, F.; Zacher, D.; Fischer, R. A.; Wöll, C. Step-by-Step Route for the Synthesis of Metal−Organic Frameworks. *J. Am. Chem. Soc.* **2007**, *129* (49), 15118–15119. https://doi.org/10.1021/ja076210u.

(6) Schoedel, A.; Scherb, C.; Bein, T. Oriented Nanoscale Films of Metal-Organic Frameworks By Room-Temperature Gel-Layer Synthesis. *Angew. Chem. Int. Ed.* **2010**, *49* (40), 7225–7228. https://doi.org/10.1002/anie.201001684.

(7) Ghorbanpour, A.; Huelsenbeck, L. D.; Smilgies, D. M.; Giri, G. Oriented UiO-66 Thin Films through Solution Shearing. *CrystEngComm* **2017**, *20* (3), 294–300. https://doi.org/10.1039/c7ce01801k.

(8) Smilgies, D. M.; Li, R.; Giri, G.; Chou, K. W.; Diao, Y.; Bao, Z.; Amassian, A. Look Fast: Crystallization of Conjugated Molecules during Solution Shearing Probed in-Situ and in Real Time by X-Ray Scattering. *Phys. Status Solidi - Rapid Res. Lett.* **2013**, *7* (3), 177–179. https://doi.org/10.1002/pssr.201206507.

(9) Lee, J.-C.; Kim, J.-O.; Lee, H.-J.; Shin, B.; Park, S. Meniscus-Guided Control of Supersaturation for the Crystallization of High Quality Metal Organic Framework Thin Films. *Chem. Mater.* **2019**, *31* (18), 7377–7385. https://doi.org/10.1021/acs.chemmater.9b01996.

(10) Diao, Y.; Tee, B. C. K.; Giri, G.; Xu, J.; Kim, D. H.; Becerril, H. A.; Stoltenberg, R. M.; Lee, T. H.; Xue, G.; Mannsfeld, S. C. B.; Bao, Z. Solution Coating of Large-Area Organic Semiconductor Thin Films with Aligned Single-Crystalline Domains. *Nat. Mater.* **2013**, *12* (7), 665–671. https://doi.org/10.1038/nmat3650.

(11) Ameloot, R.; Gobechiya, E.; Uji-i, H.; Martens, J. A.; Hofkens, J.; Alaerts, L.; Sels, B. F.; De Vos, D. E. Direct Patterning of Oriented Metal-Organic Framework Crystals via Control over Crystallization Kinetics in Clear Precursor Solutions. *Adv. Mater.* **2010**, *22* (24), 2685–2688. https://doi.org/10.1002/adma.200903867.

(12) Hendon, C. H.; Walsh, A. Chemical Principles Underpinning the Performance of the Metal-Organic Framework HKUST-1. *Chem. Sci.* **2015**, *6* (7), 3674–3683. https://doi.org/10.1039/c5sc01489a.
(13) Stephen, S.; Samuel, M.; Jonathan, P. H.; Orpen, A. G.; Ian, D. A Chemically Functionalizable Nanoporous Material [Cu3 (TMA) 2 (H2O) 3] n. **1999**, *3* (February), 1148–1151.
(14) Furukawa, H.; Cordova, K. E.; O'Keeffe, M.; Yaghi, O. M. The Chemistry and Applications of Metal-Organic Frameworks. *Science* **2013**, *341* (6149). https://doi.org/10.1126/science.1230444.
(15) Long, J. R. Introduction to Metal − Organic Frameworks. *Chem. Rev.* **2012**, *112*, 673–674. https://doi.org/10.1021/cr300014x.
(16) Stock, N.; Biswas, S.; Topologies, M. O. F.; Stock, N.; Biswas, S. Synthesis of Metal-Organic Frameworks (MOFs): Routes to Various. *Chem. Rev.* **2012**, *112* (2), 933–969. https://doi.org/10.1021/cr200304e.
(17) Xie, L. S.; Skorupskii, G.; Dincă, M. Electrically Conductive Metal–Organic Frameworks. *Chem. Rev.* **2020**, acs.chemrev.9b00766. https://doi.org/10.1021/acs.chemrev.9b00766.
(18) Nidamanuri, N.; Maity, K.; Saha, S. Electrically Conductive Metal-Organic Frameworks. In *Series on Chemistry, Energy and the Environment*; WORLD SCIENTIFIC, 2018; Vol. 02, pp 655–686. https://doi.org/10.1142/9789813226739_0015.
(19) Schneider, C.; Ukaj, D.; Koerver, R.; Talin, A. A.; Kieslich, G.; Pujari, S. P.; Zuilhof, H.; Janek, J.; Allendorf, M. D.; Fischer, R. A. High Electrical Conductivity and High Porosity in a Guest@MOF Material: Evidence of TCNQ Ordering within Cu_3BTC_2 Micropores. *Chem. Sci.* **2018**, *9* (37), 7405–7412. https://doi.org/10.1039/C8SC02471E.
(20) Mao, Y.; Cao, W.; Li, J.; Liu, Y.; Ying, Y.; Sun, L.; Peng, X. Enhanced Gas Separation through Well-Intergrown MOF Membranes: Seed Morphology and Crystal Growth Effects. *J. Mater. Chem. A* **2013**, *1* (38), 11711. https://doi.org/10.1039/c3ta12402a.
(21) Lee, J.-C.; Kim, J.-O.; Lee, H.-J.; Shin, B.; Park, S. Meniscus-Guided Control of Supersaturation for the Crystallization of High Quality Metal Organic Framework Thin Films. *Chem. Mater.* **2019**, *31* (18), 7377–7385. https://doi.org/10.1021/acs.chemmater.9b01996.
(22) Jung, S.; Huelsenbeck, L.; Hu, Q.; Robinson, S.; Giri, G. Conductive, Large-Area, and Continuous 7,7,8,8-Tetracyanoquinodimethane@HKUST-1 Thin Films Fabricated Using Solution Shearing. *ACS Appl. Mater. Interfaces* **2021**, acsami.1c00640. https://doi.org/10.1021/acsami.1c00640.
(23) Le Berre, M.; Chen, Y.; Baigl, D. From Convective Assembly to Landau−Levich Deposition of Multilayered Phospholipid Films of Controlled Thickness. *Langmuir* **2009**, *25* (5), 2554–2557. https://doi.org/10.1021/la803646e.
(24) Hastie, T.; Tibshirani, R.; Friedman, J. H. *The Elements of Statistical Learning: Data Mining, Inference, and Prediction*, 2nd ed.; Springer series in statistics; Springer: New York, NY, 2009.
(25) Smola, A. J.; Schölkopf, B. A Tutorial on Support Vector Regression. *Stat. Comput.* **2004**, *14* (3), 199–222. https://doi.org/10.1023/B:STCO.0000035301.49549.88.
(26) Efron, B. The Bootstrap and Modern Statistics. *J. Am. Stat. Assoc.* **2000**, *95* (452), 1293–1296. https://doi.org/10.1080/01621459.2000.10474333.
(27) Hirose, M.; Tsunemi, E.; Kobayashi, K.; Yamada, H. Influence of Grain Boundary on Electrical Properties of Organic Crystalline Grains Investigated by Dual-Probe Atomic

Force Microscopy. *Appl. Phys. Lett.* **2013**, *103* (17), 173109. https://doi.org/10.1063/1.4826582.
(28) Shao, Y.; Fang, Y.; Li, T.; Wang, Q.; Dong, Q.; Deng, Y.; Yuan, Y.; Wei, H.; Wang, M.; Gruverman, A.; Shield, J.; Huang, J. Grain Boundary Dominated Ion Migration in Polycrystalline Organic–Inorganic Halide Perovskite Films. *Energy Environ. Sci.* **2016**, *9* (5), 1752–1759. https://doi.org/10.1039/C6EE00413J.
(29) Le Berre, M.; Chen, Y.; Baigl, D. From Convective Assembly to Landau−Levich Deposition of Multilayered Phospholipid Films of Controlled Thickness. *Langmuir* **2009**, *25* (5), 2554–2557. https://doi.org/10.1021/la803646e.
(30) Schneider, C.; Mendt, M.; Pöppl, A.; Crocellà, V.; Fischer, R. A. Scrutinizing the Pore Chemistry and the Importance of Cu(I) Defects in TCNQ-Loaded Cu $_3$ (BTC) $_2$ by a Multitechnique Spectroscopic Approach. *ACS Appl. Mater. Interfaces* **2020**, *12* (1), 1024–1035. https://doi.org/10.1021/acsami.9b16663.
(31) Schneider, C.; Mendt, M.; Pöppl, A.; Crocellà, V.; Fischer, R. A. Scrutinizing the Pore Chemistry and the Importance of Cu(I) Defects in TCNQ-Loaded Cu3BTC2 by a Multi-Technique Spectroscopic Approach. 20.
(32) Sun, W.; Li, Y.; Liu, H.; Jiang, L. Controlled Synthesis of Three Dimensionally Oriented Charge Transfer Salts Nanowires Arrays. *Mol. Divers. Preserv. Int. MDPI* **2006**, *Vol.8* (No.6), P.39.
(33) Heintz, R. A.; Zhao, H.; Ouyang, X.; Grandinetti, G.; Cowen, J.; Dunbar, K. R. New Insight into the Nature of Cu(TCNQ): Solution Routes to Two Distinct Polymorphs and Their Relationship to Crystalline Films That Display Bistable Switching Behavior. *Inorg. Chem.* **1999**, *38* (1), 144–156. https://doi.org/10.1021/ic9812095.
(34) Hu, L.; Shi, L.; Hong, H.; Li, M.; Bao, Q.; Tang, J.; Ge, J.; Lu, J.; Cao, X.; Gu, H. Catalytic Epoxidation of Stilbene with FePt@Cu Nanowires and Molecular Oxygen. *Chem. Commun.* **2010**, *46* (45), 8591. https://doi.org/10.1039/c0cc03204b.
(35) Major, G. H.; Fairley, N.; Sherwood, P. M. A.; Linford, M. R.; Terry, J.; Fernandez, V.; Artyushkova, K. Practical Guide for Curve Fitting in X-Ray Photoelectron Spectroscopy. *J Vac Sci Technol A* 23.
(36) Kang, C.; Lee, Y.; Kim, I.; Hyun, S.; Lee, T. H.; Yun, S.; Yoon, W.-S.; Moon, Y.; Lee, J.; Kim, S.; Lee, H.-J. Highly Efficient Nanocarbon Coating Layer on the Nanostructured Copper Sulfide-Metal Organic Framework Derived Carbon for Advanced Sodium-Ion Battery Anode. *Materials* **2019**, *12* (8), 1324. https://doi.org/10.3390/ma12081324.
(37) Thu, K.; Schneider, C.; Stavila, V.; Friddle, R. W.; Fischer, R. A.; Allendorf, M. D.; Talin, A. A. Surface Morphology and Electrical Properties of Cu 3 BTC 2 Thin Films Before and After Reaction with TCNQ. **2018**. https://doi.org/10.1021/acsami.8b15158.
(38) Rivera-Torrente, M.; Filez, M.; Schneider, C.; Wolkersdörfer, K.; Taffa, D. H.; Wark, M.; Fischer, R. A. Micro-Spectroscopy of KUST-1 Metal-Organic Framework Crystals Loaded with Tetracyanoquinodimethane: Effects of Water on Host- Guest Chemistry and Electrical Conductivity. 10.
(39) Velioglu, S.; Keskin, S. Simulation of H2/CH4 Mixture Permeation through MOF Membranes Using Non-Equilibrium Molecular Dynamics. *J. Mater. Chem. A* **2019**, *7* (5), 2301–2314. https://doi.org/10.1039/C8TA10167A.

3 Exploration of the solution sheared Zr-based MOF thin film crystallization

3.1 The work of this chapter is published as:

S. Jung, P. Verma, S. Robinson, E. Beyer, H. Hall, L. Huelsenbeck, K. Stone, and G. Giri. "Meniscus Guided Coating and Evaporative Crystallization of UiO-66 Metal Organic Framework Thin Films." Ind. Eng. Chem. Res, 2021, 60, 48, 17585 – 17595

3.2 Abstract

In the previous chapter, a large-area and continuous HKUST-1 thin film is fabricated using multiple cycles of solution shearing. The previous study focused on the crystallization of solution sheared HKUST-1 thin film only. There have been no previous reports of solution shearing based evaporative crystallization of zirconium-based MOFs, which have been widely studied for a range of applications, including separations, catalysis, sensing, and charge transport. In this work, for the first time, we show that the Zirconium 1,4-dicarboxybenzene MOF, UiO-66, can be formed using evaporative crystallization during solution shearing and that a wide range of parameters can be tuned to control the film thickness, coverage, and crystallinity. Furthermore, we show that under certain solvents (dimethylformamide), oriented growth of UiO-66 crystals on the substrate is possible. Finally, we bring the solution shearing technique closer to separation applications by growing a full film of UiO-66 crystals up to the resolution of SEM, on anodic alumina oxide (AAO). This is the first instance of UiO-66 crystals being formed using an evaporative crystallization-based flow coating method, and the solution shearing technique shows the promise to be applicable to form large-area zirconium-based MOF crystals rapidly (within seconds to minutes).

3.3 Introduction

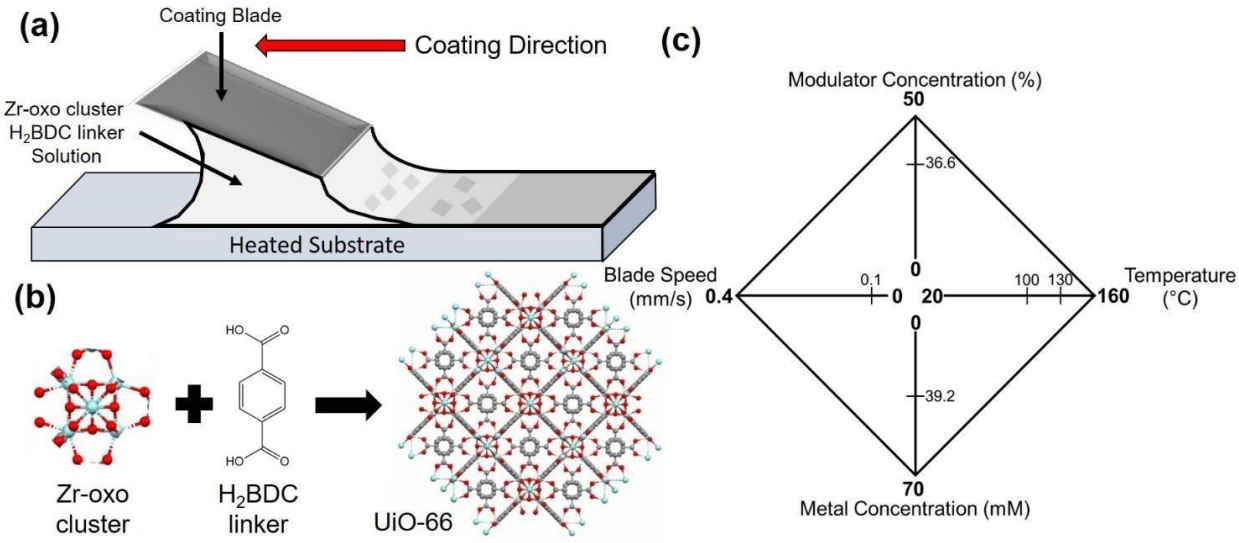

Figure 3. 1. (a) Conceptual diagram of solution shearing. The metal-oxo cluster and linker are present in the solution, and as the solvent evaporates a solid film of zirconium 1,4-dicarboxybenzene MOF (UiO-66) is grown on the substrate (gray area). (b) Chemical components of UiO-66. (c) The rectangular plot showing the operational range of each solution shearing parameter covered in this study.

The solution shearing technique is commonly used to deposit organic semiconductors[1] and polymers[2,3]-based thin films and is compatible with a wide range of materials such as pharmaceutical compounds[4] and carbon nanotubes[5]. In the previous chapter, we also have shown that the solution shearing technique can also fabricate facile, rapid, and large area HKUST-1 thin film (**Figure 3. 1**).[2,4,6–8] Therefore, there is interest to study the applicability of this technique to form films of other MOFs as well. The substrate can be extended to be any given width since the evaporation front is invariant across the width of the substrate. In addition, continuous solution feeding during solution shearing to keep a constant volume can be used to coat a substrate of any length. Therefore, large area thin film formation of MOFs is possible using solution shearing. Ghorbanpour et al.[7] have previously fabricated large area thin films of the zirconium 1,4-dicarboxybenzene MOF, called UiO-66 hereafter, using solution shearing. Here, the UiO-66 crystal was first

synthesized solvothermally, and the suspension was cast as a thin film. However, there is more interest in fabricating thin films of MOFs grown during the solution shearing process itself, in order to better control the film properties and reduce the time required to create the thin film. To this end, Lee et al.[8] have synthesized a large area, solution sheared HKUST-1 thin film by controlling the blade speed and substrate temperature. In addition, Jung et al.[6] have also shown continuous and large area solution sheared HKUST-1 thin film by using the concept of secondary crystallization. A fully covered and large area thin film was created by repeating solution shearing on the same substrate, termed passes, which showed a lack of pinholes and improved charge transport properties. However, all these studies are focused on the solution shearing of HKUST-1 as a thin film, and HKUST-1 synthesis is relatively simple due to the dimeric copper node.

Zirconium-oxo cluster (Zr-oxo) based MOFs are of interest to researchers due to their excellent thermal, chemical, and aqueous stability, and multiple papers have shown the capability of Zr-oxo based MOFs, such as UiO-66 (**Figure 3. 1. b**), for separations and sensing applications.[9–12] Most techniques of creating Zr-oxo MOFs are slow, taking hours to days, due to the complexity of the Zr-oxo cluster, which requires the coordination of six Zr atoms. Huelsenbeck et al.[13] have previously shown that the stabilization of the Zr-oxo cluster can be utilized to rapidly enhance the UiO-66 formation during aqueous-based synthesis, but this study was done for bulk crystallization and not for evaporative crystallization as a thin film. To the best of our knowledge, no studies have been performed that show evaporative crystallization of UiO-66 as a thin film. In this work, we demonstrate the solution shearing of UiO-66 for the first time, and utilize solution shearing to create thin films (**Figure 3. 1**).

There are multiple parameters that can affect the formation of crystalline MOF thin films during solution shearing, including substrate temperature, blade speed, reactant concentration, and modulator concentration (**Figure 3. 1. c**).[14] We study the impact of these parameters on the films of UiO-66 created, studying the film thickness, coverage, UiO-66 crystallinity, and crystalline orientation as a function of solution shearing parameters. We find that increasing the substrate temperature enhances the film coverage, but can increase or decrease the crystallinity of UiO-66 crystals depending on the reactant concentration. Increasing the blade speed makes thinner films, but does not show a significant change in the crystallinity. Increasing the reactant concentrations increase the film thickness and the UiO-66 crystallinity, and increasing the modulator concentration decreases the film thickness, but increases the UiO-66 crystallinity. In addition, switching the solvent to N,N-dimethylformamide (DMF) also provides similar results. We explain the results by understanding the MOF crystallization processes that occur during solution shearing and show the formation of fully covered thin films on porous substrates with the use of multiple passes up to the resolution of SEM.

3.4 Materials and Methods

Materials. Acetone (99.9 %), toluene (99.9 %), trichloro(octadecyl)silane (OTS, ≥90%), methanol (≥99.9%), zirconium(IV) propoxide solution (70 wt.% in 1-proponal) [$Zr(O\mathit{n}Pr)_4$] , acetic acid (AA, ≥99%), terephthalic acid (H_2BDC, 98%), dimethyl sulfoxide (DMSO, 99.99%), and N,N-dimethylformamide (DMF, 99.8%) were purchased from Sigma Aldrich. Isopropyl alcohol was purchased from Fisher Scientific. Silicon wafers, with a 285 nm thick silicon dioxide layer, were obtained from University Wafer. Anodic

alumina oxide (AAO) membranes with a pore size of 20 nm and a diameter of 13 mm were purchased from Sterlitech Corporation.

Substrate Preparation. Silicon wafer was cut into approximately 1 cm x 1 cm substrates. The silicon wafer was rinsed with toluene, acetone, and isopropyl alcohol, respectively. The wafer was dried using dry airflow.

Solution Shearing Blade Fabrication. Silicon wafer was used as the coating blade. The wafer was cleaned in the UV-ozone cleaner for 10 minutes. The wafer was immediately put into a crystallization dish that was filled with a solution that contained 0.1 wt.% OTS in toluene. The crystallization dish was covered with a glass lid, and the solution was kept stirring at 40 - 45 °C for 3 hours. Afterward, the wafer was sonicated in acetone for 5 minutes. A water contact angle of 95 ° - 100 ° was obtained to use the substrate as the shearing blade.

UiO-66 Precursor Solution Synthesis. Synthesis conditions were adapted from DeStefano et al.[15] In a 20 mL glass vial, $Zr(O\textit{n}Pr)_4$ and acetic acid were added to DMSO or DMF. The solution was sonicated for 5 minutes and heated at 130 °C for 2 hours. The solution was then cooled to room temperature. H_2BDC was then dissolved into the solution and the precursor solution was used for the film synthesis.

UiO-66 Thin Film Fabrication. The parameter set used for solution shearing was determined by varying reactant ($Zr(O\textit{n}Pr)_4$ and H_2BDC) concentration, blade speed, substrate temperature, and modulator concentration. The reactant concentration was varied from 39.2 mM to 70 mM for DMSO, and from 7.2 mM to 14.4 mM for DMF. The range of the solution shearing speed was from 0.05 mm/s to 0.4 mm/s, and the substrate temperature was varied from 100 °C to 160 °C. The solution shearing speed and the

substrate temperature were controlled using software (LabView). Last, the modulator concentration was varied from 36.6 % to 50 % v/v acetic acid. After the precursor solution of UiO-66 was synthesized, solution shearing was used to fabricate the UiO-66 thin film. The blade was held under a top vacuum stage. The substrates (silicon wafer and AAO) were kept on the bottom vacuum stage. The substrate stage was heated based upon the processing condition. The blade angle and its height were controlled relative to the horizontal substrate stage, respectively. Less than 10 µL of the UiO-66 precursor solution was injected into the gap between the blade and the substrate. The coating blade was moved along with the substrate to fabricate UiO-66 thin films.

Characterization. Scanning electron microscopy (SEM) images were taken via a FEI Quanta 650 scanning electron microscope. The coverage of the thin film was quantified using Fiji, an image processing program. The film thickness was measured using a Bruker Dektak XT Profilometer with a scan length of 800 µm. The X-ray Wide Angle Scattering (GIWAXS) of solution sheared UiO-66 thin films was measured at the 11-3 station of the Stanford Linear Accelerator Center (SLAC) National Accelerator Laboratory. The station provides a two-dimensional Rayonix MX225 CCD area detector. The beam energy was 12.896 KeV, the incident beam angle was 0.15 °, and the sample-to-detector distance (SDD) was 320.955 mm. The 2D GIWAXS image was analyzed using the GIXSGUI, provided by Jiang.[16]

3.5 Results and Discussion

During solution shearing, the UiO-66 precursor solution is sandwiched between a heated bottom substrate and a top moving blade as depicted in **Figure 1a**. Solvent evaporation from the meniscus leads to supersaturation of the reactants, thus inducing nucleation and growth of the UiO-66 crystals. A study conducted by Huelsenbeck et al.[13] has shown that stabilizing the Zr-oxo clusters before MOF synthesis can decrease the time scale required for MOF formation. Therefore, we synthesized UiO-66 films by stabilizing the Zr-oxo clusters first in the solution. The H_2BDC linker was dissolved into the Zr-oxo clusters solution and the solution was injected in-between the heated substrate and the blade. High temperatures and solvent evaporation promote the reaction between Zr-oxo clusters and H_2BDC linkers to form UiO-66 crystals, and the blade coating process creates UiO66 thin films. We study the UiO-66 film properties (coverage, thickness, crystallinity, and crystal orientation) by varying the temperature, blade speed, reactant concentration, modulator concentration, and solvent (**Figure 3. 1. c**).

3.5.1 Impact of Temperature on UiO-66 Film Formation:

Creating fully covered MOF films is important due to the dependence of separation, filtration and transport performance of MOF-based membranes and sensors on MOF thin film coverage.[17,18] It has been previously shown in the literature that increasing the solution shearing temperature provides better coverage of the substrate for HKUST-1.[6] Higher substrate temperature increases the solvent evaporation rate, which results in a larger amount of the solute being deposited on the substrate as a film. As we are not able to form a fully covered thin film with only one pass of solution shearing, an adjusted thickness is used, defined as the product of the film thickness and the surface coverage (**Figure 3. 2.**

a). In almost all cases, the thickness increases with higher temperatures or is within a standard deviation of the lower and higher temperatures. Grazing incidence wide angle X-ray scattering (GIWAXS) also showed that the intensity of the diffraction from the (111) crystal plane is enhanced as a function of temperature (**Figures 3. 2. b-e**). The film coverage was less impacted than the film thickness, as seen through the SEM images (**Figures 3. 2. f–k**). Here, lower magnification images seem to show full coverage of the film for the cast at 130 °C and 160 °C under the resolution of SEM, but a lack of full coverage is observed at higher magnification.

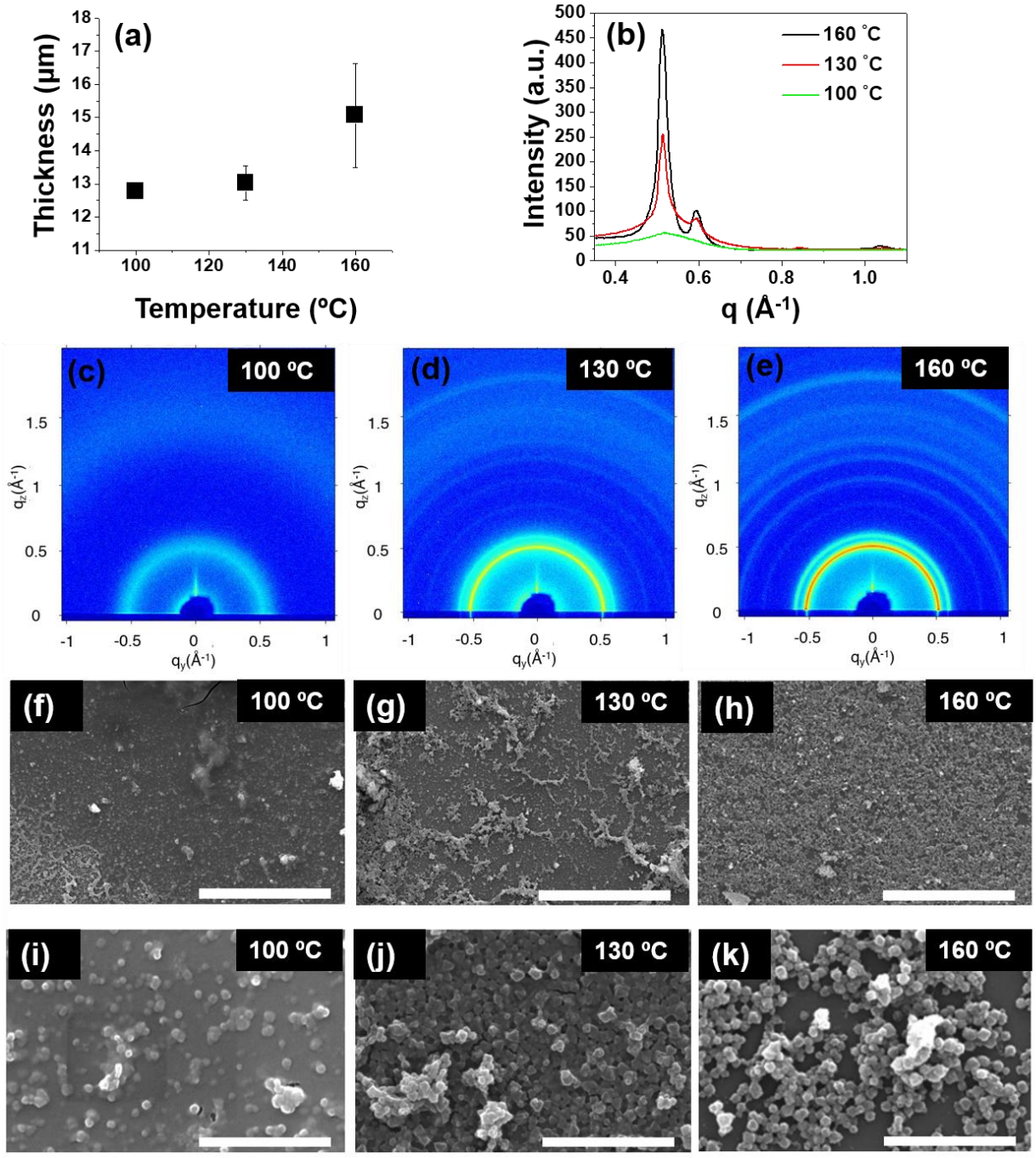

Figure 3. 2. Influence of temperature on zirconium 1,4-dicarboxybenzene MOF (UiO-66) film synthesis. (a) Adjusted thickness as a function of temperature shows increasing thickness. (b) Grazing incidence wide-angle x-ray scattering patterns of the film synthesized at 100 ºC, 130 ºC, and 160 ºC. Films created using higher temperatures show higher diffraction intensities from the (111) plane. (c) – (e) Two-dimensional grazing incidence wide-angle x-ray scattering patterns used to obtain Figure 2(b). (f) – (h) Scanning electron microscope images of the film synthesized at (f) 100 ºC, (g) 130 ºC, and (h) 160 ºC. Scale bar is 20 microns. (i) – (k) Scanning electron microscope images of the film synthesized at (f) 100 ºC, (g) 130 ºC, and (h) 160 ºC. Scale bar is 2 microns. Other conditions: Dimethyl sulfoxide, 36.6% (v/v) acetic acid, 70 mM precursor concentration, 0.1 mm/s blade speed.

Table 3. 1. Solution shearing parameters used in this study and their effects on film properties (coverage, adjusted thickness, and coherence length).

Solvent	Modulator Conc. (%) (v/v)	Reactant Conc. (mM)	Blade Speed (mm/s)	Temperature (°C)	Coverage	Adjusted thickness (µm)	Standard Deviation (µm)	Coherence Length (Å)
DMSO	36.6	39.2	0.1	130	0.67	11.60	0.38	142
DMSO	36.6	39.2	0.1	160	0.76	14.65	1.57	2a09
DMSO	36.6	39.2	0.4	130	0.75	13.52	1.78	127
DMSO	36.6	39.2	0.4	160	0.74	10.02	0.83	189
DMSO	36.6	70	0.1	100	0.75	12.78	0.09	154
DMSO	36.6	70	0.1	130	0.78	13.03	0.52	291
DMSO	36.6	70	0.1	160	0.75	15.07	1.57	262
DMSO	36.6	70	0.4	130	0.81	10.81	2.33	321
DMSO	36.6	70	0.4	160	0.75	7.88	0.51	209
DMSO	50	39.2	0.1	130	0.85	9.30	0.52	173
DMSO	50	39.2	0.4	100	0.69	7.92	0.14	115
DMSO	50	39.2	0.4	130	0.77	9.75	2.66	187
DMSO	50	39.2	0.4	160	0.85	9.85	0.73	199

We also determine the crystallinity of MOF particles by measuring the full width at half maximum (FWHM) of the integrated intensity of the diffraction from the (111) Bragg peak and then obtaining the coherence length through the Scherrer equation, where higher values of the Scherrer width indicates higher crystallinity.[19] Increasing the substrate temperature from 100 ºC to 130 ºC increases the Scherrer width as represented in **Table 3. 1,** demonstrating better crystallinity of UiO-66 particles at higher temperatures. This result holds true for all conditions tested in the study. DeStefano et al.[15] also found similar results where they demonstrated the decrease in defect density of UiO-66 crystals with increasing temperature. They hypothesize that the lability of the modulator increases with temperature, thus resulting in less defect density. However, increasing the temperature from 130 ºC to 160 ºC results in a slightly lower coherence distance in some cases, while the Scherrer width is increased in other cases (**Table 3. 1**). Upon closer examination, the results where Scherrer width decreases with increasing temperature are originated from the conditions where 70 mM of starting Zr-oxo cluster and linker concentration is utilized.

The faster rate of crystallization that occurs during solution shearing, due to the higher concentration of the Zr-oxo clusters and linkers, can lead to more defect formation, which reduces the crystal coherence length.

3.5.2 Impact of Blade Speed on UiO-66 Film Formation:

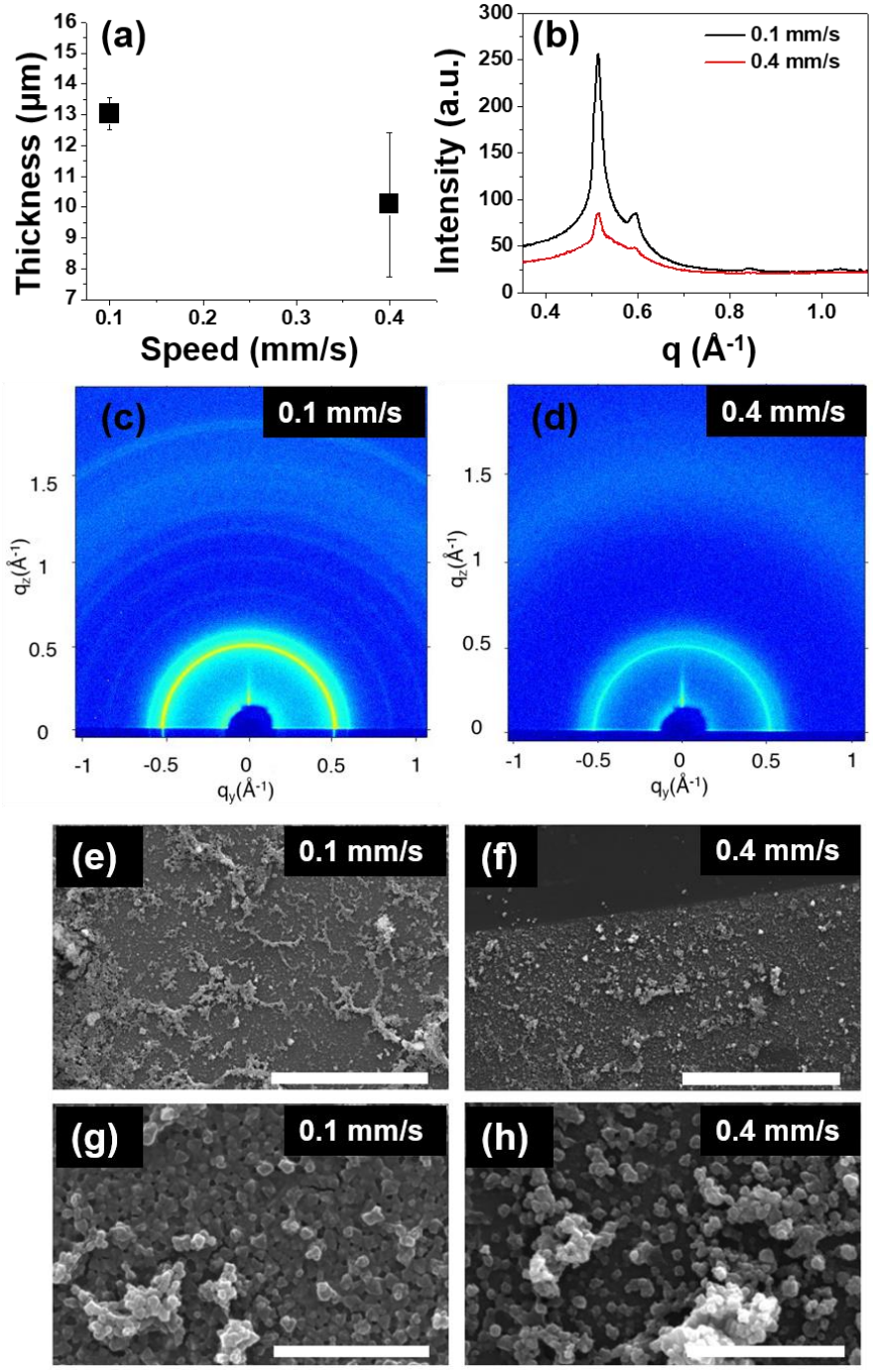

Figure 3. 3. Influence of blade speed on zirconium 1,4-dicarboxybenzene MOF (UiO-66) film synthesis. (a) Adjusted thickness as a function of speed shows decreasing thickness with increasing speed. (b) Integrated grazing incidence wide-angle x-ray scattering patterns of the film synthesized at 0.1 and 0.4 mm/s. Films created using higher speeds show lower diffraction intensities. (c) – (d) Two-dimensional grazing incidence wide-angle x-ray scattering patterns used to obtain Figure 3(b). (e) – (f) Scanning electron microscope images of the film synthesized at (e) 0.4 mm/s, and (f) 0.1 mm/s. Scale bar is 20 microns. (g) – (h) Scanning electron microscope images of the film synthesized at (g) 0.4 mm/s, and (h) 0.1 mm/s. Scale bar is 2 microns. Other conditions: Dimethyl sulfoxide, 36.6% (v/v) acetic acid, 70 mM precursor concentration, 130 ºC temperature.

The blade coating speed also changes the thin film morphology and thickness. In solution shearing, two different regimes of fluid deposition have been observed, the evaporative regime and the Landau-Levich regime.[14] In the evaporative regime, the rate of evaporation occurs on the same time scale as the blade translation, leading to evaporation and solid thin film deposition at the same time.

Conversely, in the Landau-Levich regime, the blade movement occurs faster than the evaporation rate. In this case, a liquid film is first deposited, after which the solvent evaporates and the solid film is formed. From previous literature, the evaporative conditions and the blade speed used in this study indicate that the film formation occurs in the evaporative regime.[20] In all cases, where parameters are constant except for blade speed, the adjusted film thickness is either lower or within the standard deviation of the measurements (**Table 3. 1**, **Figure 3. 3. a**). This expectation is further supported by GIXD intensities as the integration of the (111) peak intensity decreases with blade speed (**Figure 3. 3. b–d**), and SEM images show thicker films at lower blade speed (**Figure 3. 3. e–h**).

On the other hand, blade speed has a negligible effect on the Scherrer width of the UiO-66 crystallites. In all paired conditions, **Table 3. 1** shows a slight variation in the crystal coherence length with increasing blade speed. However, the relative change in Scherrer width was less than 20% for all cases, indicating that the solution shearing temperature has a larger effect on the crystallinity of the UiO-66 particles compared to the blade speed. As the blade speed does not change the evaporation rate or the reaction rate of MOF formation, it is expected that there is a less significant effect of the speed on the UiO-66 crystallinity.

3.5.3 Impact of Reactant Concentration on UiO-66 Film Formation:

We also study the impact of the chemicals used during the solution shearing process, including the concentration of the zirconium reagent and linker (while maintaining the stoichiometric ratio) and the acetic acid modulator. Increasing the precursors (zirconium propoxide and H_2BDC linker) concentrations increases the film coverage as there is more solute to crystallize, yielding more crystals and higher adjusted film thickness. In all cases with all other parameters held constant, higher reagent concentration during solution shearing resulted in a film that is as thick or thicker than the films created with a lower concentration, except for films formed at 160 °C and 0.4 mm/s (**Table 3. 1, Figure 3. 4. a**). **Figure 3. 4. b-d** illustrates the increase in the integrated (111) peak intensity as precursor concentration increases, indicating the formation of more crystals, which is further supported by SEM images as the film synthesized at 39.2 mM (**Figure 3. 4. e, g**) exhibits lower coverage than 70 mM film (**Figure 3. 4. f, h**). In addition to a higher amount of crystal formation, increasing the reagent concentration also increased the coherence length of the UiO-66 crystals for all conditions tested.

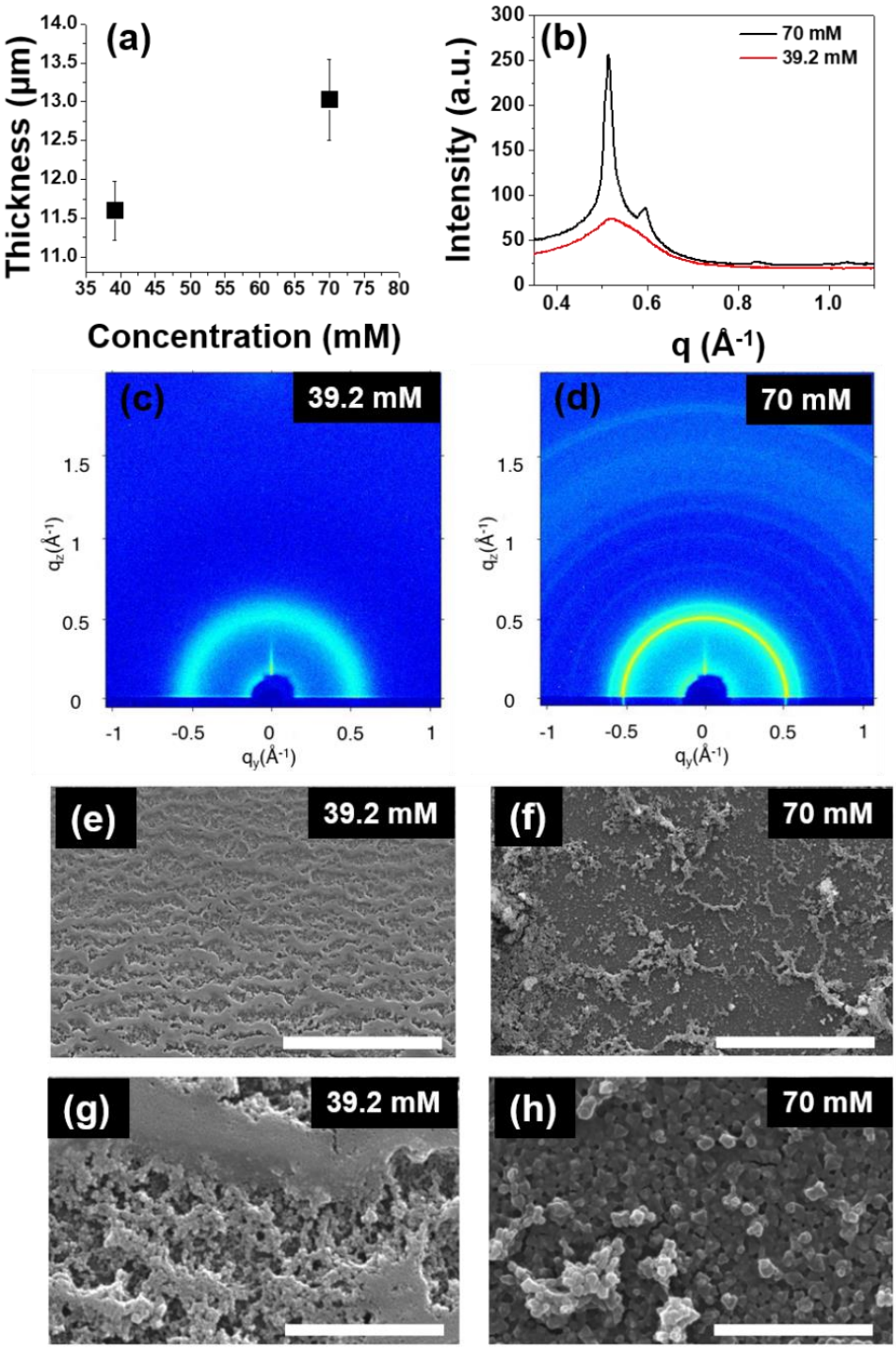

Figure 3. 4. Influence of zirconium ion and linker concentration on zirconium 1,4-dicarboxybenzene MOF (UiO-66) film synthesis. (a) Adjusted thickness as a function of concentration shows increasing thickness. (b) Integrated grazing incidence wide-angle x-ray scattering patterns of the film synthesized at 39.2 mM and 70 mM zirconium ion concentration, with the linker concentration held stoichiometrically constant. (c) – (d) Two-dimensional grazing incidence wide-angle x-ray scattering patterns used to obtain Figure 4(b). (e) – (f) Scanning electron microscope images of the film synthesized at (e) 39.2 mM and (f) 70 mM. Scale bar is 20 microns. (g) – (h) Scanning electron microscope images of the film synthesized at (g) 39.2 mM and (h) 70 mM. Scale bar is 2 microns. Other conditions: Dimethyl sulfoxide, 36.6% (v/v) acetic acid, 130 ºC temperature, 0.1 mm/s blade speed.

Increasing the modulator (acetic acid) concentration causes a decrease in the adjusted film thickness for all cases where other parameters are held constant (**Table 3. 1, Figure 3. 5. a**). The range of the modulator concentration is chosen by balancing zirconium cluster formation and organic linker dissolution. It has been hypothesized previously in the literature that the modulator competitively binds with the Zr-oxo ions, so that a higher modulator concentration indicates less binding of the linker, leading to a lower film thickness during solution shearing.[7] However, the integration of the peak intensity from GIWAXS shows that there is an increase in (111) peak intensity, as illustrated in **Figure 3. 5. b-d.** This result is further corroborated by the SEM images as the film synthesized at 36.6% (v/v) acetic acid exhibits fewer crystals (**Figure 3. 5. e, g**) than 50% (v/v) acetic acid film (**Figure 3. 5. f, h**). Additionally, we see that increasing the modulator concentration increases the Scherrer width as measured from the FWHM of (111) peak. This unexpected result occurs due to the slower nucleation and growth kinetics of MOF formation, yielding more crystalline UiO-66 particles. Similarly, Schaate et al.[21] observed the increase in coherence length of UiO-66 crystals with increasing modulator concentration during solvothermal synthesis. Therefore, increasing the modulator concentration during solution shearing causes a lower adjusted film thickness, but the crystallinity is higher. The changes in the thickness and crystallinity of the thin film when each parameter is varied while other parameters stay constant are summarized in **Table 3. 2**. Therefore, depending on the film thickness and crystallinity desired, different parametric handles can influence the crystallization process during solution shearing to control the thin film formation.

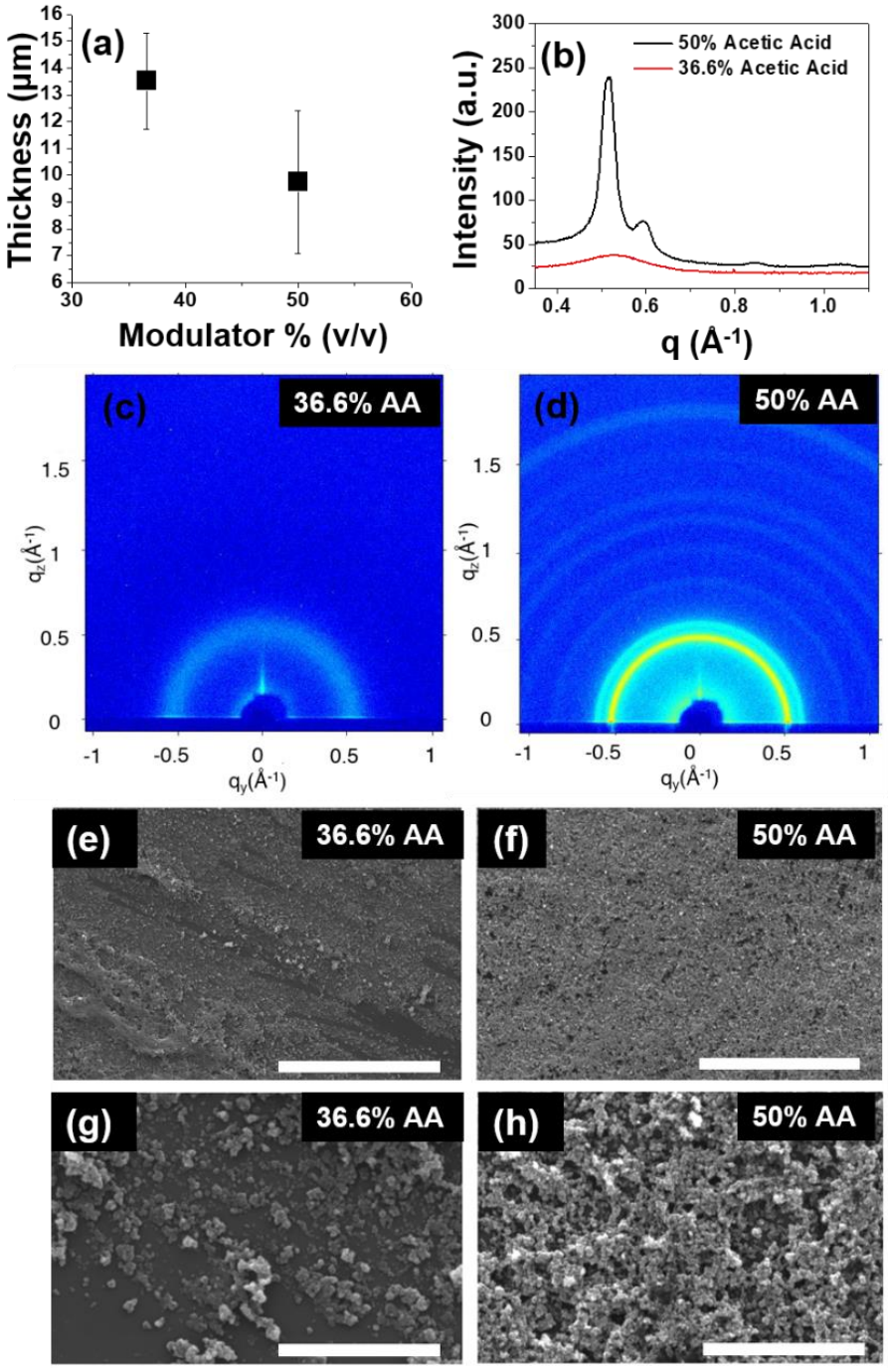

Figure 3. 5. Influence of acetic acid modulator concentration on zirconium 1,4-dicarboxybenzene MOF (UiO-66) film synthesis. (a) Adjusted thickness as a function of modulator concentration shows decreasing thickness. (b) Integrated grazing incidence wide-angle x-ray scattering patterns of the film synthesized at 36.6 % (v/v) acetic acid and 50% (v/v) acetic acid. (c) – (d) Two-dimensional grazing incidence wide-angle x-ray scattering patterns used to obtain Figure 5(b). (e) – (f) Scanning electron microscope images of the film synthesized with 36.6 % (v/v) acetic acid and 50% (v/v) acetic acid. Scale bar is 20 microns. (g) – (h) Scanning electron microscope images of the film synthesized with 36.6 % (v/v) acetic acid and 50% (v/v) acetic acid. Scale bar is 2 microns. Other conditions: Dimethyl sulfoxide, 39.2 mM precursor concentration, 130 ºC temperature, 0.4 mm/s blade speed.

Table 3. 2. Summary of the parameters influencing various film properties

Parameter	Adjusted Thickness (H)	Coherence Length (L)
Temperature (°C, T) ↑	H ↑	L ↑
Blade Speed (mm/s, V) ↑	H ↓	L ↓
Precursor Concentration (mM, C) ↑	H ↑	L ↑
Modulator Concentration % (v/v, A) ↑	H ↓	L ↑

3.5.4 Solvent Effect:

In addition to precursor concentration, modulator concentration, blade speed, and temperature, the solvent also affects the MOF formation.[22,23] Therefore, we study the evaporative crystallization of UiO-66 using DMF as the solvent. However, due to the limited solubility of zirconium propoxide in DMF, the maximum concentration of precursors used is 14.4 mM when dissolved in DMF. As this restriction impacts the crystal nucleation and growth rates, it was impossible to straightforwardly compare the results obtained between DMF and DMSO.

We studied the effects of temperature, blade speed, and precursor concentration on film coverage and UiO-66 crystallinity using DMF as a solvent. We find that the relationship described in **Table 3. 2** is valid for DMF as well (**Table A3. 1 and Figure A3. 1 - 3**). Additionally, we observed the faceted UiO-66 crystals in DMF, similar to previous studies (**Figure A3. 4**).[7,24–26]

3.5.5 Shearing on Anodic Alumina Oxide (AAO) membrane:

To demonstrate the versatility of the solution shearing method for evaporative crystallization of MOFs for membranes, we fabricated a UiO-66 thin film on a porous AAO membrane. Previous studies have reported UiO-66 films on AAO membranes using

solvothermal synthesis.[27,28] However, a longer synthesis time (24 h - 72 h) is undesired for industrial applications. Here, we synthesize UiO66 films on AAO using solution shearing within minutes using DMF as the solvent (36.6% (v/v) acetic acid, 14.4 mM precursor concentration, 130 ºC temperature, and 0.1 mm/s blade speed). We choose DMF as the solvent for this synthesis as DMF rendered faceted crystals. **Figure 3. 6** represents the SEM images of bare AAO (**Figure 3. 6. a, d**) and UiO-66-AAO (**Figure 3. 6. b, c, e, f**) membranes. With one pass of solution shearing, the presence of UiO-66 crystal can be observed on the AAO membrane, but the film is not fully covered (**Figure 3. 6. b, e**). To obtain full coverage, we used our previous understanding of HKUST-1 growth during solution shearing, where multiple coating passes can be used to create a fully covered film.[4] By using 6 passes of solution shearing, we are able to form a fully covered film on the AAO substrate (**Figure 3. 6. c, f**) under the resolution of SEM.

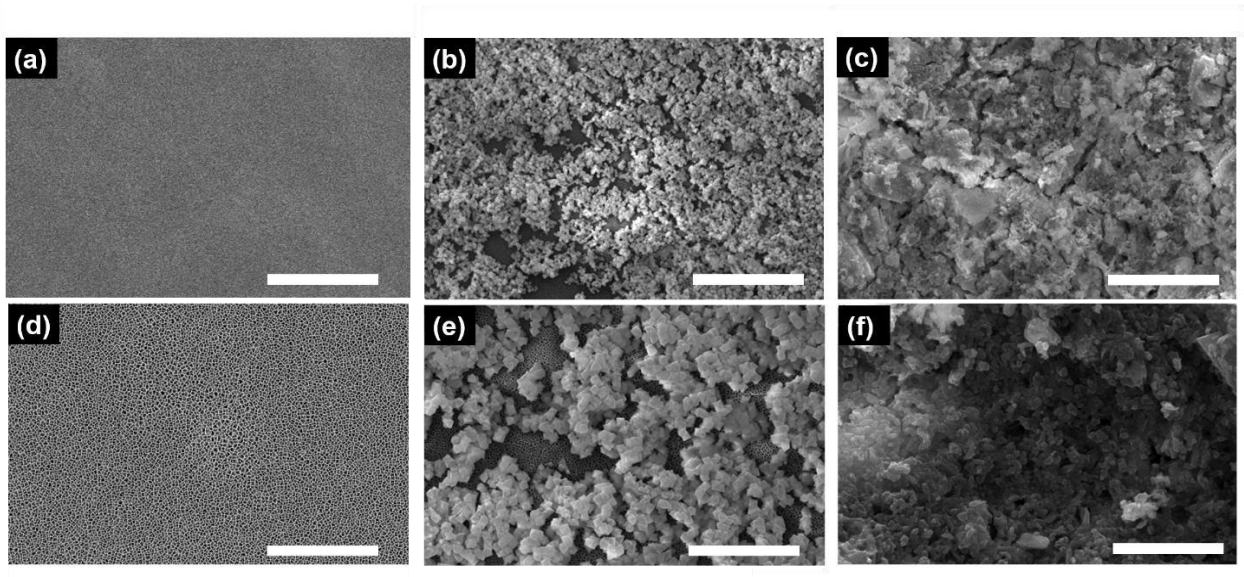

Figure 3. 6. Scanning electron microscope images of the (a), (d) Bare anodic alumina oxide membrane, (b), (e) zirconium 1,4-dicarboxybenzene MOF (UiO-66) film synthesized on anodic alumina oxide using 1 pass of solution shearing, and (c), (f) zirconium 1,4-dicarboxybenzene MOF (UiO-66) film synthesized on anodic alumina oxide using 6 passes of solution shearing. Scale bar is 20 microns in (a) – (c) and 5 microns in (d) – (e). Synthesis conditions: N,N-dimethylformamide, 36.6% (v/v) acetic acid, 14.4 mM reactant concentration, 130 ºC temperature, and 0.1 mm/s blade speed.

3.6 Conclusion

In this chapter, we demonstrate that the solution shearing process can rapidly fabricate zirconium 1,4-dicarboxybenzene MOF (UiO-66) thin films, with the possibility of being able to be used for large area formation. The solution shearing parameters (precursor concentration, modulator concentration, solvent, blade speed, and substrate temperature) are varied to observe changes in coverage, crystallinity, and crystal orientation of the thin films. The UiO-66 film coverage on the substrate is confirmed via profilometry and SEM images. The crystallinity of UiO-66 with different solution shearing conditions is analyzed by comparing the coherence length of the crystals present in the thin films. We find that increasing the precursor concentration and substrate temperature render higher adjusted thickness and better crystallinity of UiO-66 thin films. Additionally, blade speed and modulator concentration have inverse effects on the adjusted thickness, and higher crystallinity of UiO-66 crystals is achieved with decreasing blade speed and increasing modulator concentration. Therefore, higher concentrations of precursor and modulator, higher substrate temperatures, and lower blade speeds are required to fabricate UiO-66 films with better-adjusted thickness and crystallinity of UiO-66 crystals. In addition, this trend is also observed when DMF is used as a solvent. These results, for the first time, show that evaporative crystallization of Zr-oxo MOF films can be performed, and thin films of Zr-oxo MOFs can also be created in a rapid manner that is compatible with large-area production. These results will expand the large-area application possibilities of MOF thin films such as catalysis, sensing, and separation.

3.7 Chapter 3 Appendices

Table A3. 1. Solution shearing parameters used in the study and their effects on film properties (coverage, adjusted thickness, and coherence length), using DMF as the solvent.

Solvent	Modulator Conc. (%) (v/v)	Reactant Conc. (mM)	Blade Speed (mm/s)	Temperature (°C)	Coherence Length (Å)
DMF	36.6	7.2	0.1	100	143
DMF	36.6	7.2	0.1	130	176
DMF	36.6	7.2	0.1	160	276
DMF	36.6	7.2	0.4	160	221
DMF	36.6	14.4	0.05	130	234
DMF	36.6	14.4	0.1	100	192
DMF	36.6	14.4	0.1	130	249
DMF	36.6	14.4	0.1	160	334
DMF	36.6	14.4	0.4	130	175
DMF	36.6	14.4	0.4	160	302

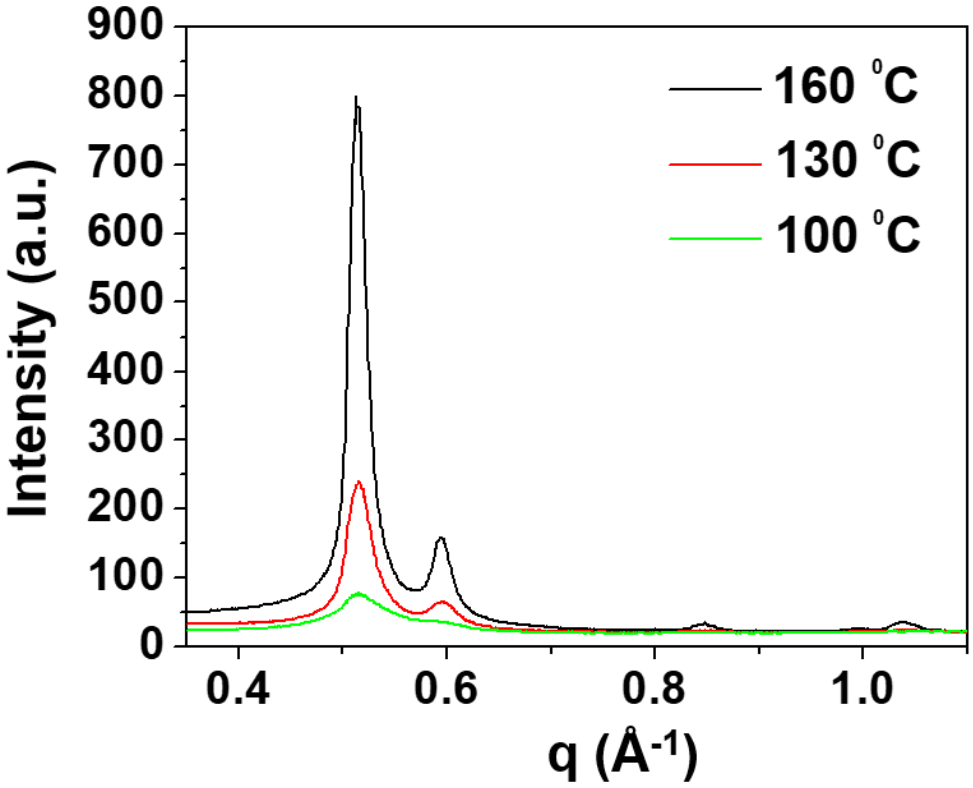

Figure A3. 1. Influence of temperature on UiO-66 film synthesis. Films created using higher temperature show higher diffraction intensities from the (111) plane. Other conditions: DMF, 36.6% (v/v) acetic acid, 14.4 mM precursor concentration, 0.1 mm/s blade speed.

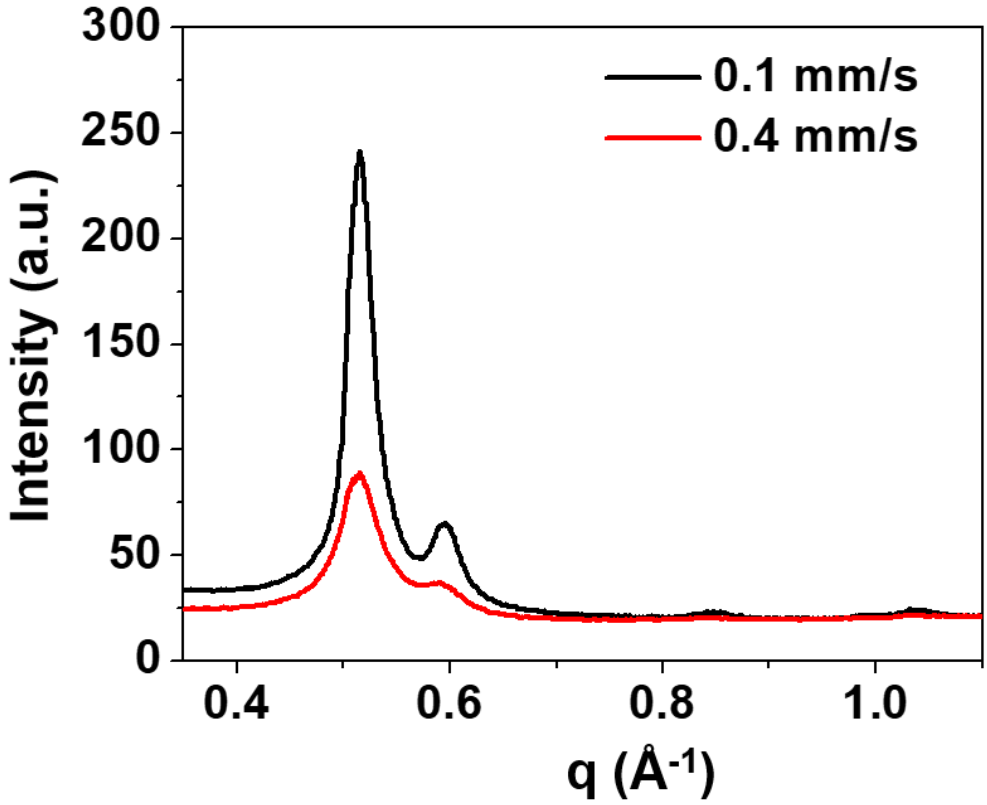

Figure A3. 2. Influence of blade speed on UiO-66 film synthesis. Films created using higher speeds show lower diffraction intensities from the (111) plane. Other conditions: DMF, 36.6% (v/v) acetic acid, 14.4 mM precursor concentration, 130 ºC temperature.

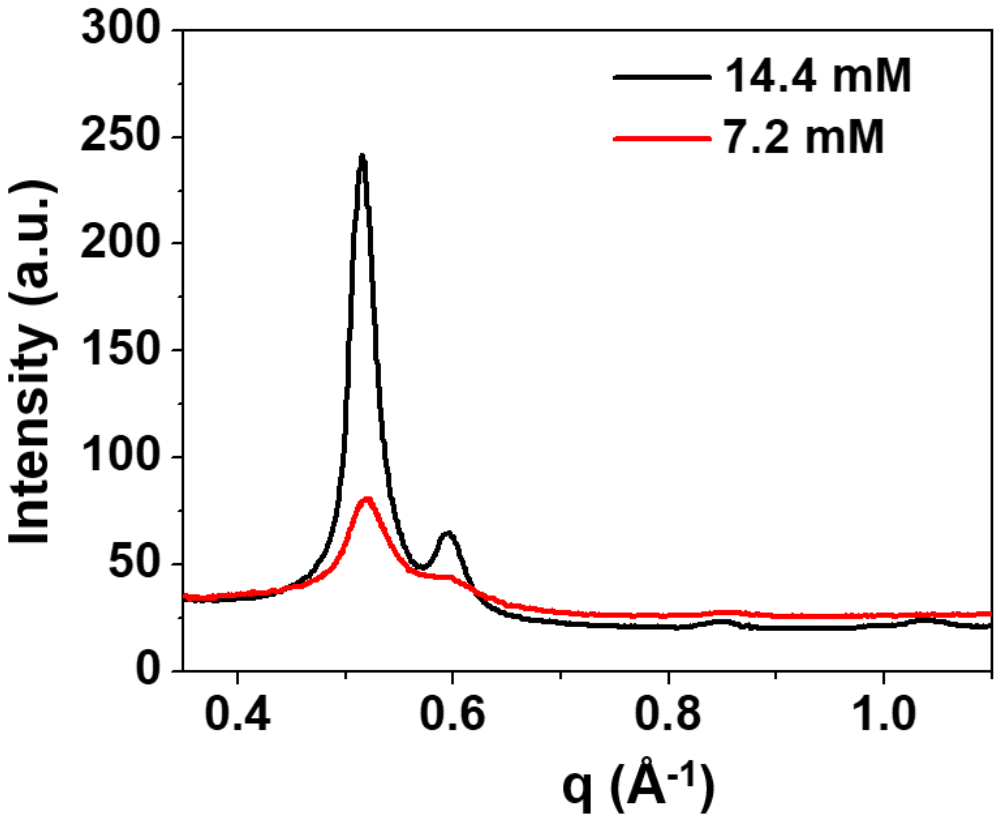

Figure A3. 3. Influence of Zr ion and linker concentration on UiO-66 film synthesis. Films created using higher concentration show higher diffraction intensities from the (111) plane. Other conditions: DMF, 36.6% (v/v) acetic acid, 130 ºC temperature, 0.1 mm/s blade speed.

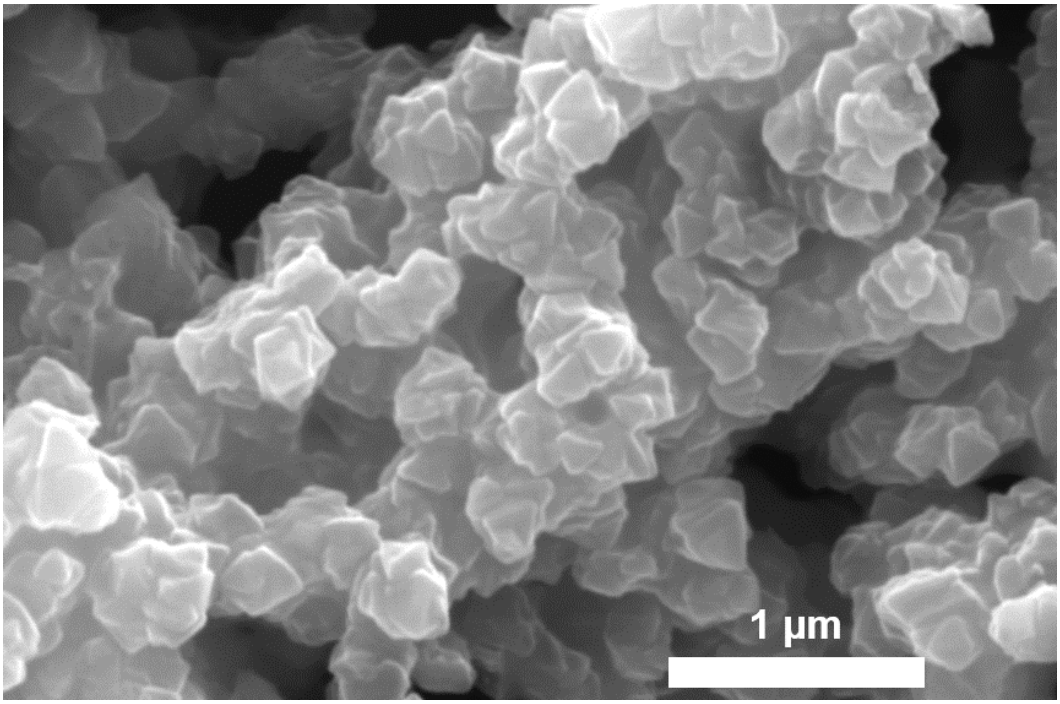

Figure A3. 4. SEM image of the UiO-66 film. Synthesis conditions: DMF, 36.6% (v/v) acetic acid, 14.4 mM precursor concentration, and drop casted at 130 ºC.

3.8 References

(1) Chen, M.; Peng, B.; Huang, S.; Chan, P. K. L. Understanding the Meniscus-Guided Coating Parameters in Organic Field-Effect-Transistor Fabrications. *Adv. Funct. Mater.* **2020**, *30* (1), 1905963. https://doi.org/10.1002/adfm.201905963.

(2) Worfolk, B. J.; Andrews, S. C.; Park, S.; Reinspach, J.; Liu, N.; Toney, M. F.; Mannsfeld, S. C. B.; Bao, Z. Ultrahigh Electrical Conductivity in Solution-Sheared Polymeric Transparent Films. *Proc. Natl. Acad. Sci.* **2015**, *112* (46), 14138–14143. https://doi.org/10.1073/pnas.1509958112.

(3) Shaw, L.; Hayoz, P.; Diao, Y.; Reinspach, J. A.; To, J. W. F.; Toney, M. F.; Weitz, R. T.; Bao, Z. Direct Uniaxial Alignment of a Donor–Acceptor Semiconducting Polymer Using Single-Step Solution Shearing. *ACS Appl. Mater. Interfaces* **2016**, *8* (14), 9285–9296. https://doi.org/10.1021/acsami.6b01607.

(4) Guthrie, S. M.; Smilgies, D.-M.; Giri, G. Controlling Polymorphism in Pharmaceutical Compounds Using Solution Shearing. *Cryst. Growth Des.* **2018**, *18* (2), 602–606. https://doi.org/10.1021/acs.cgd.7b01686.

(5) Park, S.; Pitner, G.; Giri, G.; Koo, J. H.; Park, J.; Kim, K.; Wang, H.; Sinclair, R.; Wong, H.-S. P.; Bao, Z. Large-Area Assembly of Densely Aligned Single-Walled Carbon Nanotubes Using Solution Shearing and Their Application to Field-Effect Transistors. *Adv. Mater.* **2015**, *27* (16), 2656–2662. https://doi.org/10.1002/adma.201405289.

(6) Jung, S.; Huelsenbeck, L.; Hu, Q.; Robinson, S.; Giri, G. Conductive, Large-Area, and Continuous 7,7,8,8-Tetracyanoquinodimethane@HKUST-1 Thin Films Fabricated Using Solution Shearing. *ACS Appl. Mater. Interfaces* **2021**, *13* (8), 10202–10209. https://doi.org/10.1021/acsami.1c00640.

(7) Ghorbanpour, A.; Huelsenbeck, L. D.; Smilgies, D.-M.; Giri, G. Oriented UiO-66 Thin Films through Solution Shearing. *CrystEngComm* **2018**, *20* (3), 294–300. https://doi.org/10.1039/C7CE01801K.

(8) Lee, J.-C.; Kim, J.-O.; Lee, H.-J.; Shin, B.; Park, S. Meniscus-Guided Control of Supersaturation for the Crystallization of High Quality Metal Organic Framework Thin Films. *Chem. Mater.* **2019**, *31* (18), 7377–7385. https://doi.org/10.1021/acs.chemmater.9b01996.

(9) Yao, B.-J.; Ding, L.-G.; Li, F.; Li, J.-T.; Fu, Q.-J.; Ban, Y.; Guo, A.; Dong, Y.-B. Chemically Cross-Linked MOF Membrane Generated from Imidazolium-Based Ionic Liquid-Decorated UiO-66 Type NMOF and Its Application toward CO_2 Separation and Conversion. *ACS Appl. Mater. Interfaces* **2017**, *9* (44), 38919–38930. https://doi.org/10.1021/acsami.7b12697.

(10) Yoo, D. K.; Woo, H. C.; Jhung, S. H. Removal of Particulate Matters with Isostructural Zr-Based Metal–Organic Frameworks Coated on Cotton: Effect of Porosity of Coated MOFs on Removal. *ACS Appl. Mater. Interfaces* **2020**, *12* (30), 34423–34431. https://doi.org/10.1021/acsami.0c08881.

(11) Ahmad, M. Z.; Navarro, M.; Lhotka, M.; Zornoza, B.; Téllez, C.; de Vos, W. M.; Benes, N. E.; Konnertz, N. M.; Visser, T.; Semino, R.; Maurin, G.; Fila, V.; Coronas, J. Enhanced Gas Separation Performance of 6FDA-DAM Based Mixed Matrix Membranes by Incorporating MOF UiO-66 and Its Derivatives. *J. Membr. Sci.* **2018**, *558*, 64–77. https://doi.org/10.1016/j.memsci.2018.04.040.

(12) Das, A.; Anbu, N.; Sk, M.; Dhakshinamoorthy, A.; Biswas, S. A Functionalized UiO-66 MOF for Turn-on Fluorescence Sensing of Superoxide in Water and Efficient Catalysis for Knoevenagel Condensation. *Dalton Trans.* **2019**, *48* (46), 17371–17380. https://doi.org/10.1039/C9DT03638E.
(13) Huelsenbeck, L.; Luo, H.; Verma, P.; Dane, J.; Ho, R.; Beyer, E.; Hall, H.; Geise, G. M.; Giri, G. Generalized Approach for Rapid Aqueous MOF Synthesis by Controlling Solution PH. *Cryst Growth Des* **2020**, 9.
(14) Le Berre, M.; Chen, Y.; Baigl, D. From Convective Assembly to Landau−Levich Deposition of Multilayered Phospholipid Films of Controlled Thickness. *Langmuir* **2009**, *25* (5), 2554–2557. https://doi.org/10.1021/la803646e.
(15) DeStefano, M. R.; Islamoglu, T.; Garibay, S. J.; Hupp, J. T.; Farha, O. K. Room-Temperature Synthesis of UiO-66 and Thermal Modulation of Densities of Defect Sites. *Chem. Mater.* **2017**, *29* (3), 1357–1361. https://doi.org/10.1021/acs.chemmater.6b05115.
(16) Jiang, Z. *GIXSGUI* : A MATLAB Toolbox for Grazing-Incidence X-Ray Scattering Data Visualization and Reduction, and Indexing of Buried Three-Dimensional Periodic Nanostructured Films. *J. Appl. Crystallogr.* **2015**, *48* (3), 917–926. https://doi.org/10.1107/S1600576715004434.
(17) Qiu, S.; Xue, M.; Zhu, G. Metal–Organic Framework Membranes: From Synthesis to Separation Application. *Chem Soc Rev* **2014**, *43* (16), 6116–6140. https://doi.org/10.1039/C4CS00159A.
(18) Chernikova, V.; Yassine, O.; Shekhah, O.; Eddaoudi, M.; Salama, K. N. Highly Sensitive and Selective SO $_2$ MOF Sensor: The Integration of MFM-300 MOF as a Sensitive Layer on a Capacitive Interdigitated Electrode. *J. Mater. Chem. A* **2018**, *6* (14), 5550–5554. https://doi.org/10.1039/C7TA10538J.
(19) Patterson, A. L. The Scherrer Formula for X-Ray Particle Size Determination. *Phys. Rev.* **1939**, *56* (10), 978–982. https://doi.org/10.1103/PhysRev.56.978.
(20) Giri, G.; Li, R.; Smilgies, D.-M.; Li, E. Q.; Diao, Y.; Lenn, K. M.; Chiu, M.; Lin, D. W.; Allen, R.; Reinspach, J.; Mannsfeld, S. C. B.; Thoroddsen, S. T.; Clancy, P.; Bao, Z.; Amassian, A. One-Dimensional Self-Confinement Promotes Polymorph Selection in Large-Area Organic Semiconductor Thin Films. *Nat. Commun.* **2014**, *5* (1), 3573. https://doi.org/10.1038/ncomms4573.
(21) Schaate, A.; Roy, P.; Godt, A.; Lippke, J.; Waltz, F.; Wiebcke, M.; Behrens, P. Modulated Synthesis of Zr-Based Metal-Organic Frameworks: From Nano to Single Crystals. *Chem. - Eur. J.* **2011**, *17* (24), 6643–6651. https://doi.org/10.1002/chem.201003211.
(22) Zhang, B.; Zhang, J.; Liu, C.; Sang, X.; Peng, L.; Ma, X.; Wu, T.; Han, B.; Yang, G. Solvent Determines the Formation and Properties of Metal–Organic Frameworks. *RSC Adv.* **2015**, *5* (47), 37691–37696. https://doi.org/10.1039/C5RA02440D.
(23) Chen, B.; Wang, X.; Zhang, Q.; Xi, X.; Cai, J.; Qi, H.; Shi, S.; Wang, J.; Yuan, D.; Fang, M. Synthesis and Characterization of the Interpenetrated MOF-5. *J. Mater. Chem.* **2010**, *20* (18), 3758. https://doi.org/10.1039/b922528e.
(24) Miyamoto, M.; Kohmura, S.; Iwatsuka, H.; Oumi, Y.; Uemiya, S. In Situ Solvothermal Growth of Highly Oriented Zr-Based Metal Organic Framework UiO-66 Film with Monocrystalline Layer. *CrystEngComm* **2015**, *17* (18), 3422–3425. https://doi.org/10.1039/C5CE00462D.
(25) Vo, T. K.; Le, V. N.; Yoo, K. S.; Song, M.; Kim, D.; Kim, J. Facile Synthesis of UiO-66(Zr) Using a Microwave-Assisted Continuous Tubular Reactor and Its Application for Toluene

Adsorption. *Cryst. Growth Des.* **2019**, *19* (9), 4949–4956. https://doi.org/10.1021/acs.cgd.9b00170.

(26) Liu, X.; Demir, N. K.; Wu, Z.; Li, K. Highly Water-Stable Zirconium Metal–Organic Framework UiO-66 Membranes Supported on Alumina Hollow Fibers for Desalination. *J. Am. Chem. Soc.* **2015**, *137* (22), 6999–7002. https://doi.org/10.1021/jacs.5b02276.

(27) Wu, W.; Li, Z.; Chen, Y.; Li, W. Polydopamine-Modified Metal–Organic Framework Membrane with Enhanced Selectivity for Carbon Capture. *Environ. Sci. Technol.* **2019**, *53* (7), 3764–3772. https://doi.org/10.1021/acs.est.9b00408.

(28) Xu, T.; Shehzad, M. A.; Wang, X.; Wu, B.; Ge, L.; Xu, T. Engineering Leaf-Like UiO-66-SO3H Membranes for Selective Transport of Cations. *Nano-Micro Lett.* **2020**, *12* (1), 51. https://doi.org/10.1007/s40820-020-0386-6.

4 Polymer incorporation into the solution sheared Zr-based MOF thin film

4.1 The work of this chapter is published as:

S. Jung, S. Robinson, Y. Baek, A. Dhakal, P. Verma, M. Stone, and G. Giri. "Fabrication of polymer incorporated UiO-66 metal-organic framework thin films using solution shearing." *In Preparation*, **2022**.

4.2 Abstract

In the previous chapter, we have shown the fabrication of the zirconium-based thin film, called UiO-66, using solution shearing, and discussed how the solution shearing parameters affect the crystallinity of the UiO-66 thin film. In this chapter, the pores of UiO-66 are incorporated by polymer molecules. A combination of both the polymer and the MOF properties can be achieved in this composite, called polyMOF. In this study, the thin film composite of piezoelectric polymer, known as poly(vinyl difluoride) (PVDF), and UiO-66 is fabricated using solution shearing. Initially, the PVDF solution is mixed with the linker solution so that PVDF chains and linker molecules are present in the same solution. Then, the node solution is added to the polymer and linker-containing solution so that PVDF chains can be entrapped inside the UiO-66 pores, indicating that the UiO-66 crystals grow around the polymer chains. With multiple shearing cycles, a large area and continuous thin film of PVDF@UiO-66 was fabricated within a minute. The film coverage is 100% up to the resolution of SEM, and the polymer incorporation inside the UiO-66 pores is confirmed by testing the piezoelectric performance of the PVDF@UiO-66 composite. Compared to the conventional polyMOF thin film fabrication technique, PVDF@UiO-66 thin film using solution shearing can reduce the synthesis time of the composite, and control the thin film properties such as coverage, crystallinity, flexibility, and thickness.

4.3 Introduction

In Chapter 3, solution shearing is used to fabricate the zirconium-based MOF, UiO-66, as a thin film and to control the crystal orientation and the film thickness. In this chapter, the fabrication of the polymer incorporated zirconium-based MOFs using solution shearing will be discussed. The porous nature of MOFs makes them well suited for making composite materials. Guest molecules can be integrated into the MOF structure by interacting with the open metal sites (OMS) inside the MOF pores chemically.[1–3] These interactions provide changes in the physical and chemical properties of the MOFs. Talin et al.[2] incorporated TCNQ molecules into the copper-based MOF, called HKUST-1, to endow an electrical conductivity into the HKUST-1 so that seven orders magnitude of higher electrical conductivity is realized. Hermann et al.[4] incorporated photochromic azobenzene into MOF-5, Gallium MIL-68, and Indium MIL-68, which resulted in improved photochromic reaction to light. The incorporation of guest molecules into MOF pores gives MOFs an extra dimension of tunability and expands potential applications.

An emerging type of MOF composites is polymer-MOF composite, called polyMOF. PolyMOF takes advantage of the properties of the polymer and MOFs so that flexible and highly porous composite can be synthesized.[5] This makes polyMOF particularly well suited for membrane-based separations for a wide range of applications. Guo et al.[6] created poly(styrene sulfonate) (PSS) with HKUST-1 composites to make membranes for lithium-ion separation in salt water brines. Shanahan et al.[7] made composites of polyaniline (PANI) with the zirconium oxide-based MOF (UiO-66 and UiO-66-NH_2), which created material with tunable semi-conductivity. Physical mixing is an extremely simple and straightforward technique of synthesizing MOF-polymer composites. With physical mixing, MOF particles

and polymer chains are mixed together in a solution. The mixture can then be deposited to fabricate a thin film.[8] Moghadam et al.[9] fabricated flexible membranes of poly(vinyl difluoride) (PVDF) and UiO-66 composite by mixing solvothermally grown UiO-66 particles with PVDF in solution and subsequently electrospinning the solution on a substrate. In their work, PVDF@UiO-66 composite shows higher piezoelectric performance than PVDF polymer itself. As the COOH-groups in UiO-66 promote hydrogen bonding with CF_2 in PVDF, the formation of β-phase PVDF, which has the strongest piezoelectric response, becomes probable. Furthermore, Lu et al.[10] also utilized electrospinning to make PVDF@UiO-66-NH_2 textiles from physically mixed UiO-66 particles and PVDF fibers in N,N-dimethylformamide (DMF) for use in detoxification of chemical warfare agents. With physical mixing, polymer loading into MOF pores can only be achieved through diffusion. Small guest molecules can easily diffuse into the MOF pores and bind to active sites. However, polymer chains are generally very large, which results in a low diffusivity into MOF pores.[5] This makes the polymer loading process in physical mixing very slow.

As opposed to physical mixing techniques, chemical mixing techniques involve mixing polymer chains with MOF components (linker and node separately) in solution. With chemical mixing, the desired polymer is dissolved into either a linker or node solution. Li et al.[11] synthesized PEDOT:PSS@HKUST-1 by first mixing negatively charged PEDOT:PSS with positively charged copper hydroxide nano strands (CHNs). Subsequent addition of acidic linker formed HKUST-1 with PEDOT:PSS entrapped in the pores. The same technique was employed by Guo et al.[6] to make PSS@HKUST-1. With chemical mixing, polymer loading is not limited by diffusion. Thus, reaction timescales are only limited by MOF formation and growth.

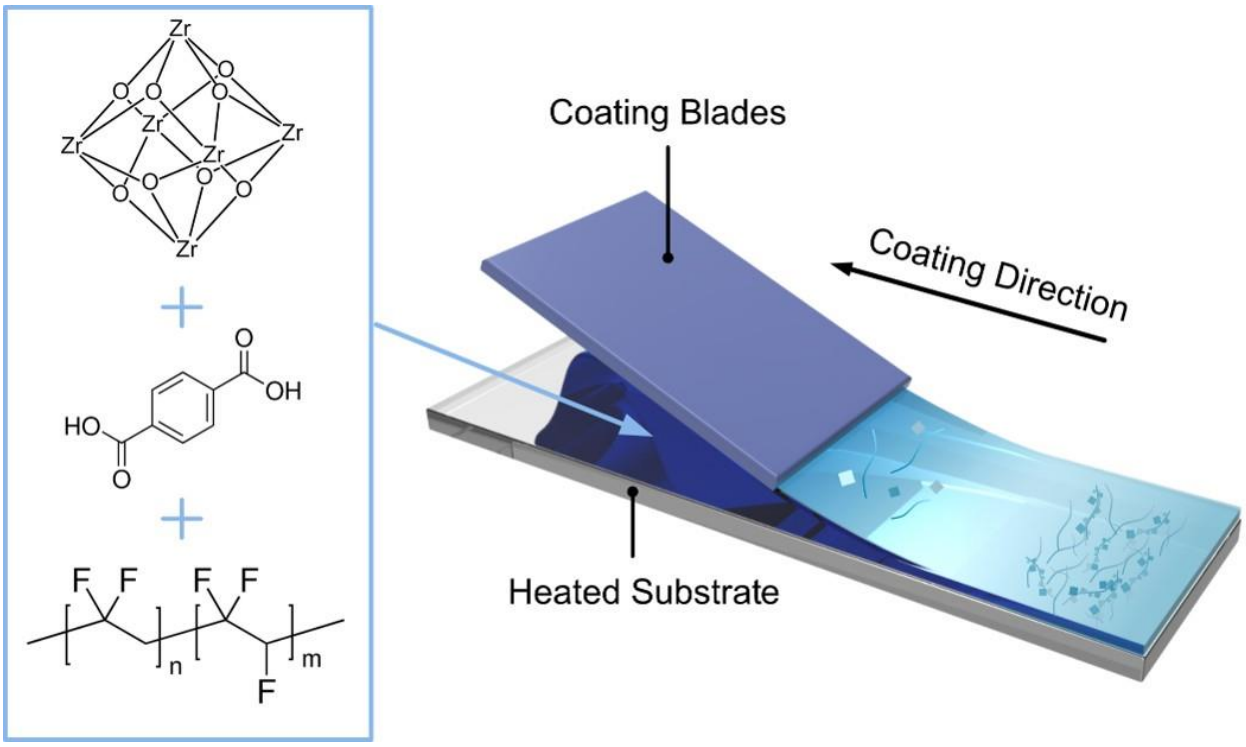

Figure 4. 1. Schematic of solution shearing. The precursor solution that contains node, linker and polymer is added into the gap between coating blades and heated substrates. As the coating blade move from one side to another side, solvent starts evaporating, and crystallization occurs.

In the previous chapter, we have shown the fabrication of UiO-66 thin films using solution shearing. In this chapter, we present a generalized approach to synthesize a composite of poly(vinyl difluoride) (PVDF) and UiO-66 using solution shearing. (**Figure 4. 1**) Both polymers[12] and MOFs[13–17] thin films have been fabricated using solution shearing and other meniscus guided coating techniques. However, there has been no publication showing the synthesis of a MOF-polymer composite using this method. By first mixing the PVDF solution with the linker followed by the node, the PVDF can be incorporated inside UiO-66 pores during crystallization. (**Figure 4. 2**) With multiple shearing cycles, we achieve large area, continuous thin films of PVDF@UiO-66. Using a combination of characterization techniques, including Fourier Transform Infrared Spectroscopy (FTIR), X-Ray Diffraction (XRD), Scanning Electron Microscopy (SEM), energy dispersive X-ray spectroscopy (EDS), and piezoelectric measurement, we confirm the presence of β phase-PVDF, the retention of UiO-66 crystallinity

and morphology in the composite. This generalized technique can be applied to other polymer-MOF systems to significantly improve the production timescale and quality of the thin films.

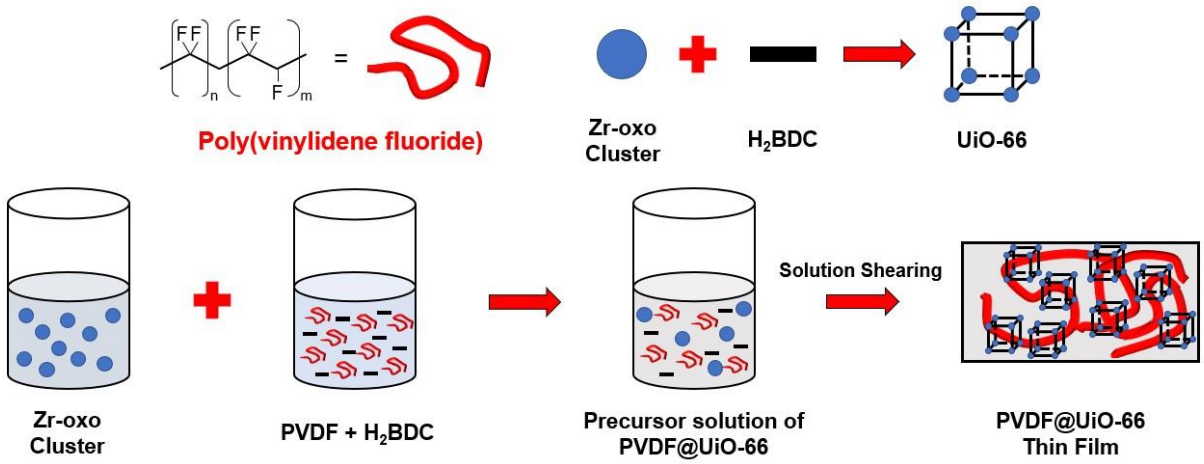

Figure 4. 2. Schematic of the polyMOF synthesis. PVDF is mixed with the linker solution and added to the node solution to synthesize the precursor solution of PVDF@UiO-66.

4.4 Materials and Methods

Materials. Acetone (99.9 %), toluene (99.9 %), trichloro(octadecyl)silane (OTS, ≥90%), methanol (≥99.9%), Zirconium (IV) propoxide solution (70 wt.% in 1-proponal) [$Zr(O\textit{n}Pr)_4$], acetic acid (AA, ≥99%), terephthalic acid (H_2BDC, 98%), solvene®250/P300, and N,N-dimethylformamide (DMF, 99.8%) were obtained from Sigma Aldrich. Glass substrates (1 mm thick), indium tin oxide (ITO) coated glass substrates (1.1 mm thick and 100 Ω/sq), and isopropyl alcohol were purchased from Fisher Scientific. Silicon wafers, with a 285 nm thick silicon dioxide layer, were obtained from University Wafer.

Substrate Preparation. Both glass and ITO-coated glass slides were cut into approximately 0.5" x 1" sized substrates. The glass substrates were sonicated in methanol for 10 minutes. The ITO-coated substrates were gently washed with isopropyl alcohol. Both substrates were dried using dry airflow. The glass slides were cleaned in the UV-ozone cleaner for around 10 minutes. Both glass slides and ITO-coated slides were placed on the solution shearing machine to be used as substrates.

Solution Shearing Blade Fabrication. Silicon wafer was used as the coating blade. The wafer was treated with UV-ozone for at least 10 minutes. The wafer was immediately placed on a crystallization dish that was filled with a 0.1 wt.% OTS in 50 mL toluene. The crystallization dish was covered with a glass lid, and the solution was kept stirring at 45 - 50 ℃ for at least 3 hours. Afterward, the wafer was sonicated in acetone for 5 minutes. A water contact angle should be within the range between 95 ° and 100 ° to use the substrate as the coating blade.

UiO-66 Precursor Solution Synthesis. Synthesis conditions were adapted from DeStefano et al.[19] In a 20 mL glass vial, 355 µL $Zr(O\textit{n}Pr)_4$ and 4 mL acetic acid were dissolved by 7 mL DMF. The node solution was sonicated for 5 minutes and heated at 130 ℃ for 2 hours.

The node solution was then cooled to room temperature. In a separated vial, 14.4 mM of the linker solution, H_2BDC, was dissolved by a 1:1 mixture of acetone and DMF. Then, the same amount of the node solution and the linker solution are mixed to be used for the thin film fabrication.

PVDF@UiO-66 Precursor Solution Synthesis. Synthesis conditions were adapted from Lu et al.[20] In a 20 mL glass vial, the different weight percentage of PVDF was dissolved by a 1:1 mixture of acetone and DMF. Once it is fully dissolved, 14.4 mM of H_2BDC is added to the solution. In a separate vial, 355 µL $Zr(O\textit{n}Pr)_4$ and 4 mL acetic acid were dissolved by 7 mL DMF. The node solution was sonicated for 5 minutes and heated at 130 ℃ for 2 hours. The node solution was then cooled to room temperature. Then, the solution that contains polymer and linker was mixed with the node solution by 1:1 weight ratio, and the precursor solution was used for the thin film fabrication.

UiO-66 Thin Film Fabrication. Solution shearing was used to fabricate the UiO-66 thin film. The coating blade was held under a top vacuum stage. Both glass and ITO substrates were placed on the bottom vacuum stage. The substrate stage was heated up to 100 ℃. The blade angle and its height were controlled based upon the horizontal substrate stage. Depending upon the size of the substrate, 10 µL of the UiO-66 and PVDF@UiO-66 precursor solution was injected into the gap between the coating blade and the heated substrate. The coating blade was set to 0.25 mm/s and moved along with the substrate, and the solvent evaporation occurs to deposit UiO-66 as well as PVDF@UiO-66 thin films.

Characterization. X-ray diffraction (XRD) patterns were used to observe the formation of UiO-66 on fabrics using PANalytical Empyrean diffractometer (Malven Panalytical) using Cu Kα radiation under 45 kV and 40 mA. Scanning electron microscopy (SEM) and energy dispersive spectroscopy (EDS) images were taken via a FEI Quanta 650 scanning electron microscope. FT-

IR spectra were measured via a Perkin Elmer Frontier MIR/NIR. Piezoelectric performance was measured via oscilloscope from Keysight DSOX3024T. The PVDF@UiO-66 thin film is deposited on the ITO substrate using solution shearing. The nickel tape was attached to the top of the thin film to measure its piezoelectricity.

4.5 Results and Discussion

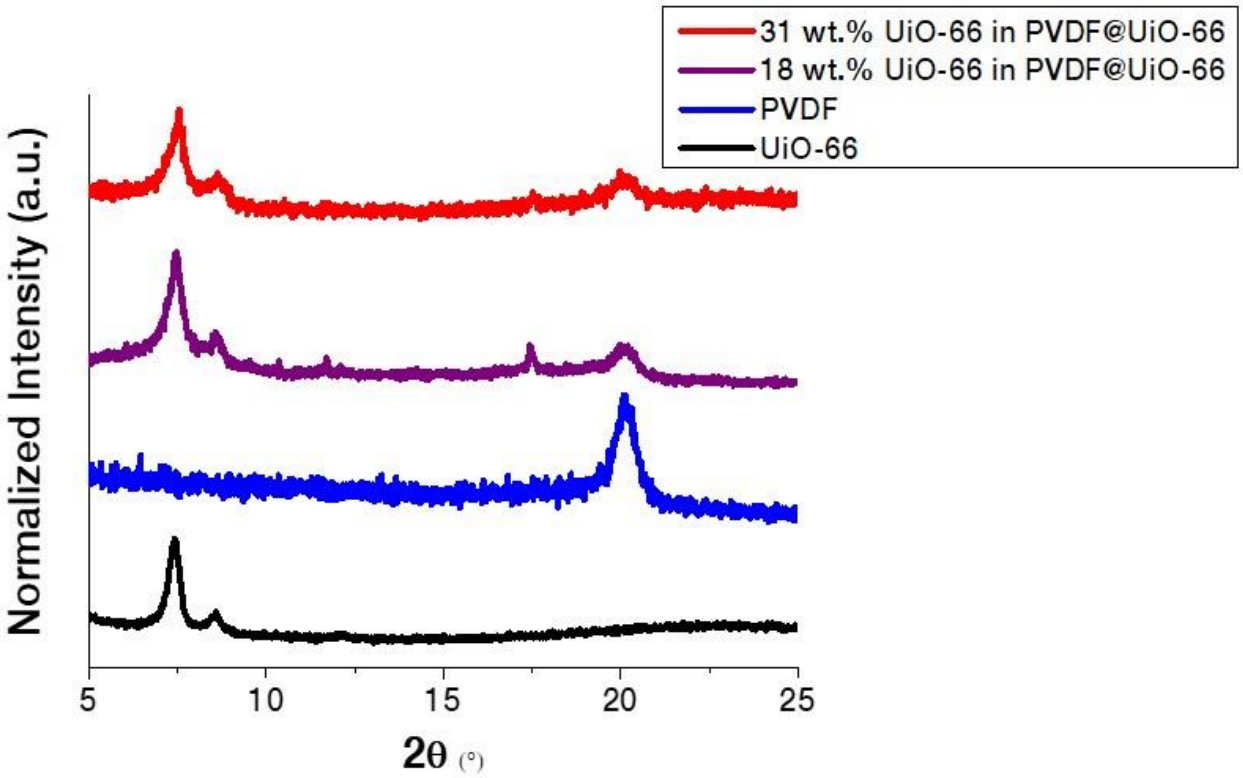

Figure 4. 3. X-ray diffraction (XRD) of 31 wt.% MOF contained PVDF@UiO-66, 18 wt.% MOF contained PVDF@UiO-66, PVDF and UiO-66, respectively. Both XRD pattern of 18 wt.% and 31 wt.% MOF contained PVDF@UiO-66 match well with that of their parent materials.

(**Calculation is shown in the appendix**) The PVDF@UiO-66 thin films are referred to as the mass fraction of the UiO-66 in the solid composite, after the solvent in the thin film is fully evaporated during deposition. The precursor solution is deposited to fabricate PVDF@UiO-66 thin film using solution shearing. During the solution shearing process, the PVDF@UiO-66 thin film was cast at 100 °C with a coating speed of 0.25 mm/s, and 14.4 mM DMF as the precursor concentration. These parameters are determined based upon the previous study in Chapter 3 because they provide high film coverage and well-oriented thin film. As can be seen in **Figure 4. 3**, the crystal structures of the different concentrations of PVDF@UiO-66 thin films match well with that of both PVDF and UiO-66. It confirms that solution shearing can rapidly fabricate the PVDF@UiO-66 thin film. In the previous studies, UiO-66 and its derivative were synthesized first

and added to the PVDF solution to form the PVDF@UiO-66 composite.[9,20] Since the crystallization of UiO-66 and the incorporation of PVDF may occur simultaneously in the solution shearing, the synthesis time of the PVDF@UiO-66 composite takes much shorter than that of previous studies. Interestingly, a single peak is observed at $2\theta = 20.5\ °$ in the XRD pattern of PVDF. This peak indicates the PVDF β-phase.

In addition, FT-IR spectra of the PVDF@UiO-66 thin film and its reactants were measured. (**Figure 4. 4**) The FT-IR spectrum of UiO-66 contains the spectrum of both Zirconium propoxide and terephthalic acid, confirming that UiO-66 is well-synthesized. (**Figure A4. 1**) FT-IR spectrum of PVDF@UiO-66 thin film also matches well with that UiO-66 and PVDF. In the spectrum of PVDF@UiO-66, the representative peaks of β-phase PVDF are shown. According to Abdullah et al.[21], 840 cm^{-1} represents CH_2 rocking, and C-C stretching is observed at 874 cm^{-1} and 1074 cm^{-1}. In addition, 1172 cm^{-1} and 1406 cm^{-1} is the wavelength that indicates CF_2 asymmetric stretching and CH_2 deformation, respectively.

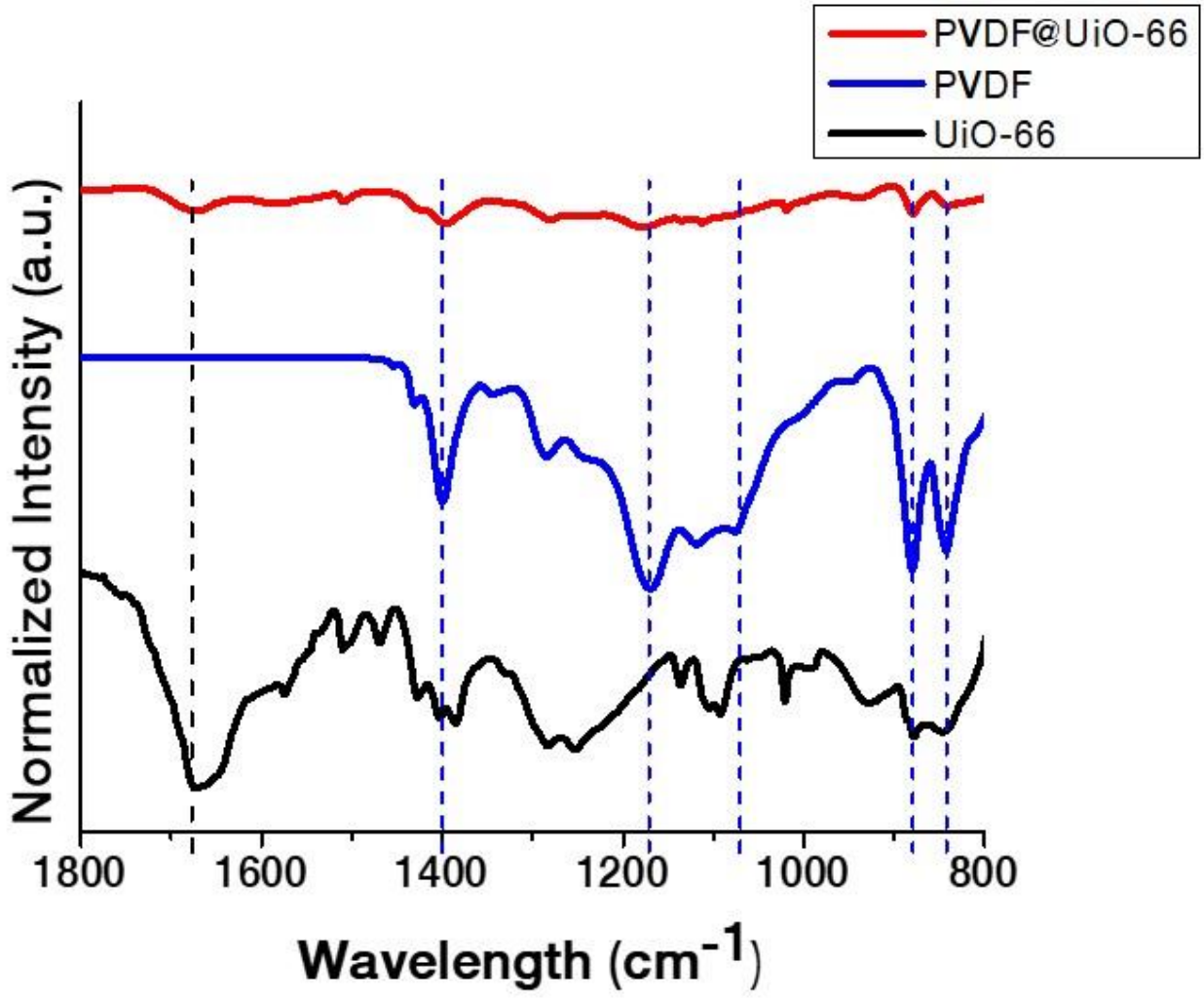

Figure 4. 4. FT-IR spectra of the PVDF@UiO-66 and its reactants. Black dot line represents the specific spectrum of UiO-66, and the blue dot lines indicate β-phase of PVDF.

As can be seen in **Figure 4. 5**, the scanning electron microscope (SEM) is used to observe the film coverage and pinholes. Compared to the pristine UiO-66 thin film, the film coverage of PVDF@UiO-66 thin film has better film coverage. As the polymer is incorporated into the UiO-66 thin film, the number of pinholes in UiO-66 is reduced. This indicates that PVDF contributes to enhancing the film coverage of PVDF@UiO-66 by reducing pinholes. As can be seen in Figure **4. 5. D**, there are some black dots on the film. These black dots are formed due to the multiple cycles of solution shearing. As the multiple cycles of solution shearing are performed, the film grows on the bare substrate as well as on the crystals from the previous solution shearing cycles.

The elemental composition of the black dots is shown in **Figure A4. 4 – 5**. No composition that represents the substrate is not observed.

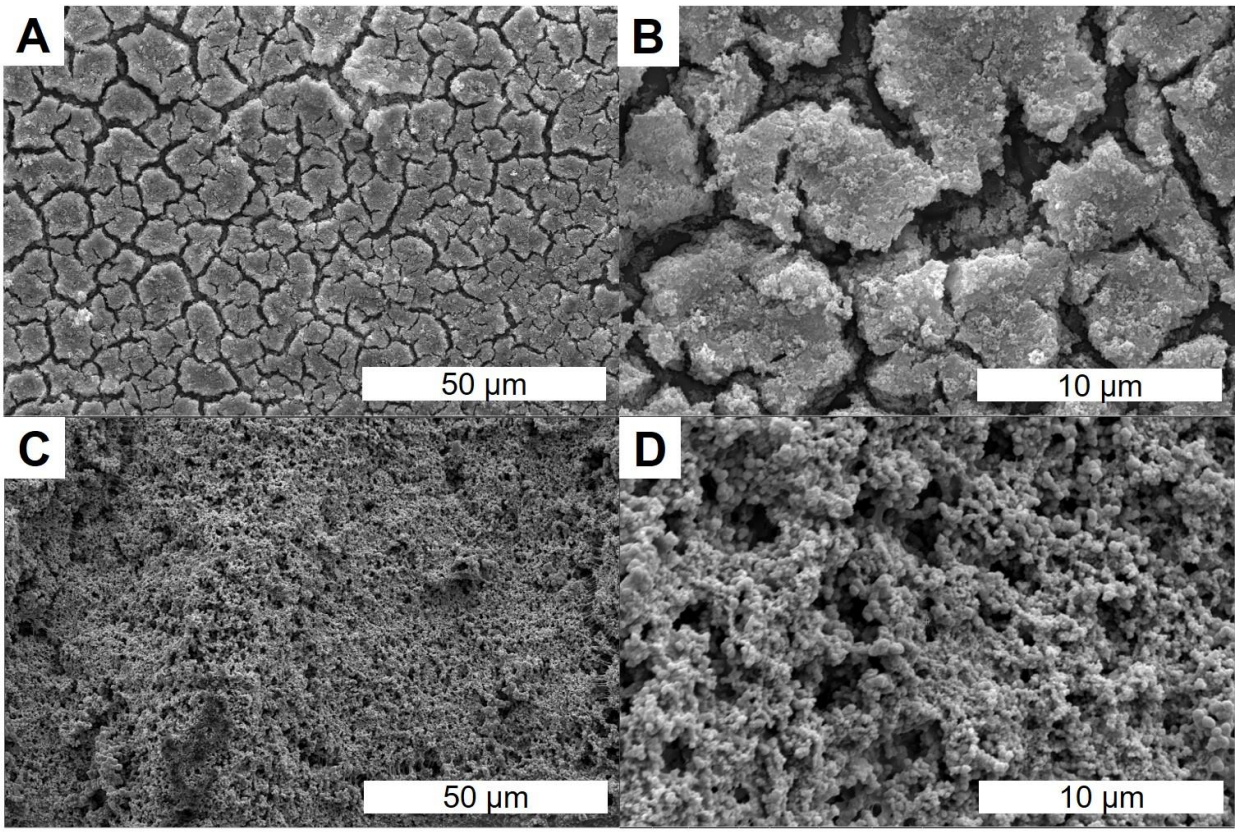

Figure 4. 5. SEM images of (**A**-**B**) UiO-66 (**C**-**D**) PVDF@UiO-66. Polymer incorporation enhances the film coverage and reduces pinholes.

In addition, energy-dispersive X-ray spectroscopy (EDS) was used to observe the elemental distribution of UiO-66, PVDF, and PVDF@UiO-66 thin film. (**Figure A4. 2 - 5**) In both PVDF@UiO-66 thin films, both zirconium from UiO-66 and fluorine from PVDF are well-distributed on the thin film, indicating that the PVDF molecules are well-distributed along with the UiO-66 thin film.

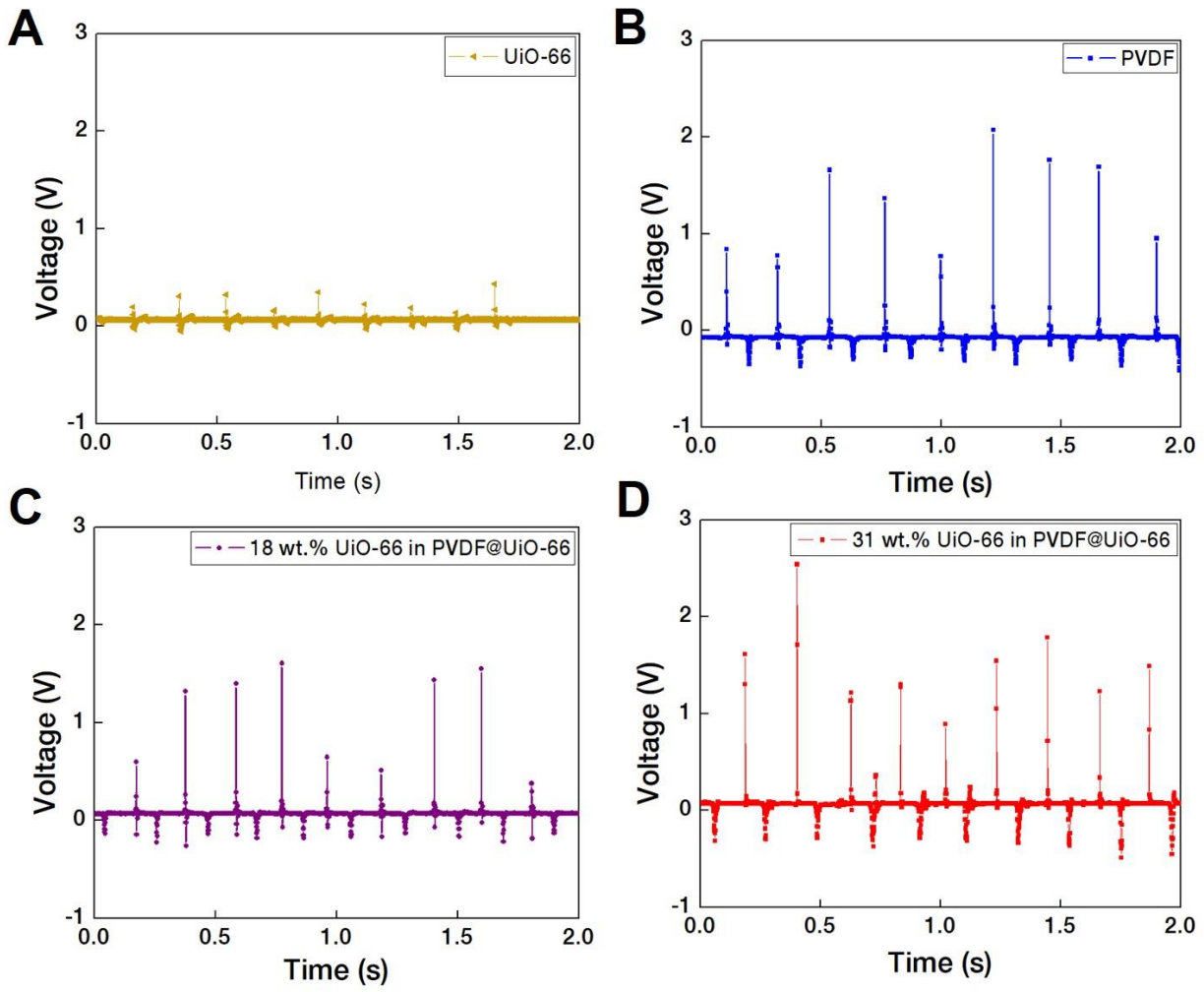

Figure 4. 6. Piezoelectric characteristic of UiO-66, PVDF, and PVDF@UiO-66 composite films. Generated voltages by pressure with finger tapping motion from the samples (A) UiO-66, (B) PVDF (C) 18 wt.% UiO-66 in PVDF@UiO-66, and (D) 31 wt.% UiO-66 in PVDF@UiO-66, respectively.

To confirm the PVDF incorporation, we have fabricated 18 wt.% and 31. wt.% UiO-66 in PVDF@UiO-66 with control samples (UiO-66 and PVDF) via the solution searing process on the ITO coated glass substrates. Then, the piezoelectric characteristic was investigated by measuring the voltage when the pressure was applied during finger tapping motions, where the higher piezoelectricity led to having higher voltage generation. **Figure 4. 6** shows the piezoelectricity of the fabricated films as a function of time, while the finger tapping motion repetitively applies pressure on the films. The positive voltages are generated when the pressure is applied to the film, followed by the negative voltage generation when the pressure is quickly removed. As shown in

Figure 4. 6 A-B, the UiO-66 film provides the smallest piezoelectricity of 200 mV under the pressure, and the PVDF film presents higher voltages around 2 V. The high voltages from the PVDF film corresponds to the results of the XRD and FTIR which confirmed the β-phase in the fabricated film. On the one hand, the piezoelectric characteristics of the composite films are shown in **Figure 4. 6 C-D**. As can be seen, the generated voltages are around 2 V which is similar to the voltages from the PVDF films. These results indicate that the chemical mixing method can fabricate the thin film that contains both the β-phase PVDF and the UiO-66 properties using solution shearing without any degradation.

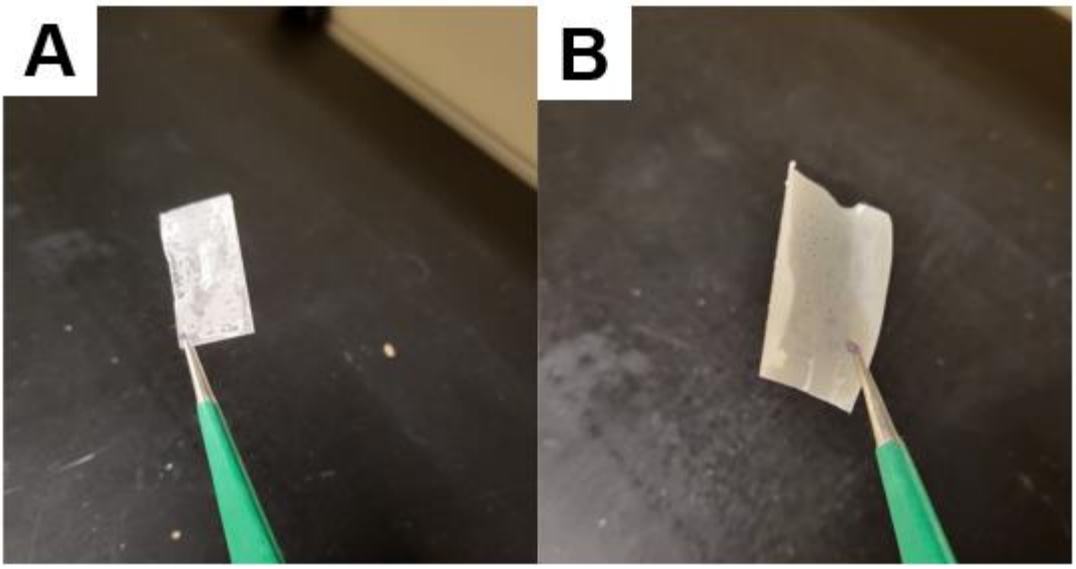

Figure 4. 7. The picture of UiO-66 thin film (A) and PVDF@UiO-66 thin film (B). Upon the incorporation of the polymer, the PVDF@UIO-66 becomes freestanding.

Furthermore, compared to the pristine UiO-66 thin film, PVDF@UiO-66 can be easily peeled off from the substrate. As shown in **Figure 4. 7**, PVDF@UiO-66 thin film becomes freestanding, showing that polymer incorporation into UiO-66 enhances the flexibility of the thin film. We expect that as the PVDF chains UiO-66 crystals, PVDF@UiO-66 thin film becomes flexible, leading to fabricating continuous, uniform, and crack-free thin film.

4.6 Conclusion

In this chapter, we demonstrated the fabrication of PVDF@UiO-66 composite thin film using solution shearing. In the PVDF solution, linker molecules are mixed initially, the node solution is added to the solution so that polymers can be entrapped in the UiO-66 pores. The synthesis of the PVDF@UiO-66 is confirmed by XRD and FT-IR. The peak of the composite matches well with that of the PVDF as well as UiO-66. The film coverage of the PVDF@UiO-66 on the substrate is determined by using SEM. We find that adding the polymer enhances the film coverage of the thin film by reducing the number of pinholes. Furthermore, the PVDF is well-distributed on the composite by observing the elemental distribution of the thin film and piezoelectric performance. This indicates that PVDF molecules are incorporated along with the UiO-66. Compared to the conventional polyMOF thin film fabrication technique, the fabrication of the thin film using solution shearing can dramatically save the synthesis time and control the film properties such as coverage, flexibility, and degree of piezoelectricity. The changes in thermal conductivity and surface area of the composite will be measured in the future so that the impact of PVDF on the thin film properties can be explored.

4.7 Chapter 4 Appendices

The calculation of the UiO-66 contents in the PVDF@UiO-66 thin film

Node solution Calculation

$$\frac{0.355\ \text{mL Zirconium Propoxide}}{} \left| \frac{0.7\ \text{Zirconium Propoxide}}{1\ \text{1-Propanol}} \right| \frac{1.044\ \text{g}}{\text{mL}} \left| \frac{\text{mol}}{327.57\ \text{g}} \right| \frac{1000\ \text{mmol}}{1\ \text{mol}} = 0.792\ \text{mmol}$$

Linker solution Calculation

$$\frac{240\ \text{mg Terephthalic acid}}{} \left| \frac{1\ \text{g}}{1000\ \text{mg}} \right| \frac{\text{mol}}{166.13\ \text{g}} \left| \frac{1000\ \text{mmol}}{1\ \text{mol}} \right. = 1.445\ \text{mmol}$$

UiO-66 Content Calculation (Assuming 100 % Conversion and 1:1 molar ratio between node and linker solution)

$$\frac{0.792\ \text{mmol Zirconium Propoxide}}{} \left| \frac{1\ \text{UiO-66}}{6\ \text{Zr-atom}} \right| \frac{1\ \text{mol}}{1000\ \text{mmol}} \left| \frac{1664.06\ \text{g}}{\text{mol}} \right. = 0.220\ \text{g UiO-66}$$

UiO-66 Weight percentage of the PVDF@UiO-66 Thin Film (ex. 10 wt. % PVDF@UiO-66)

$$\frac{5\ \text{g solvent}}{} \left| \frac{0.1\ \text{g PVDF}}{1\ \text{g solvent}} \right. + 0.220\ \text{g UiO-66} = 0.720\ \text{g PVDF@UiO-66}$$

$$\frac{0.220\ \text{g UiO-66}}{} \left| \frac{}{0.720\ \text{g PVDF@UiO-66}} \right| \frac{100\ \%}{} = 30.522\ \text{wt. \% UiO-66 in PVDF@UiO-66 Thin Film}$$

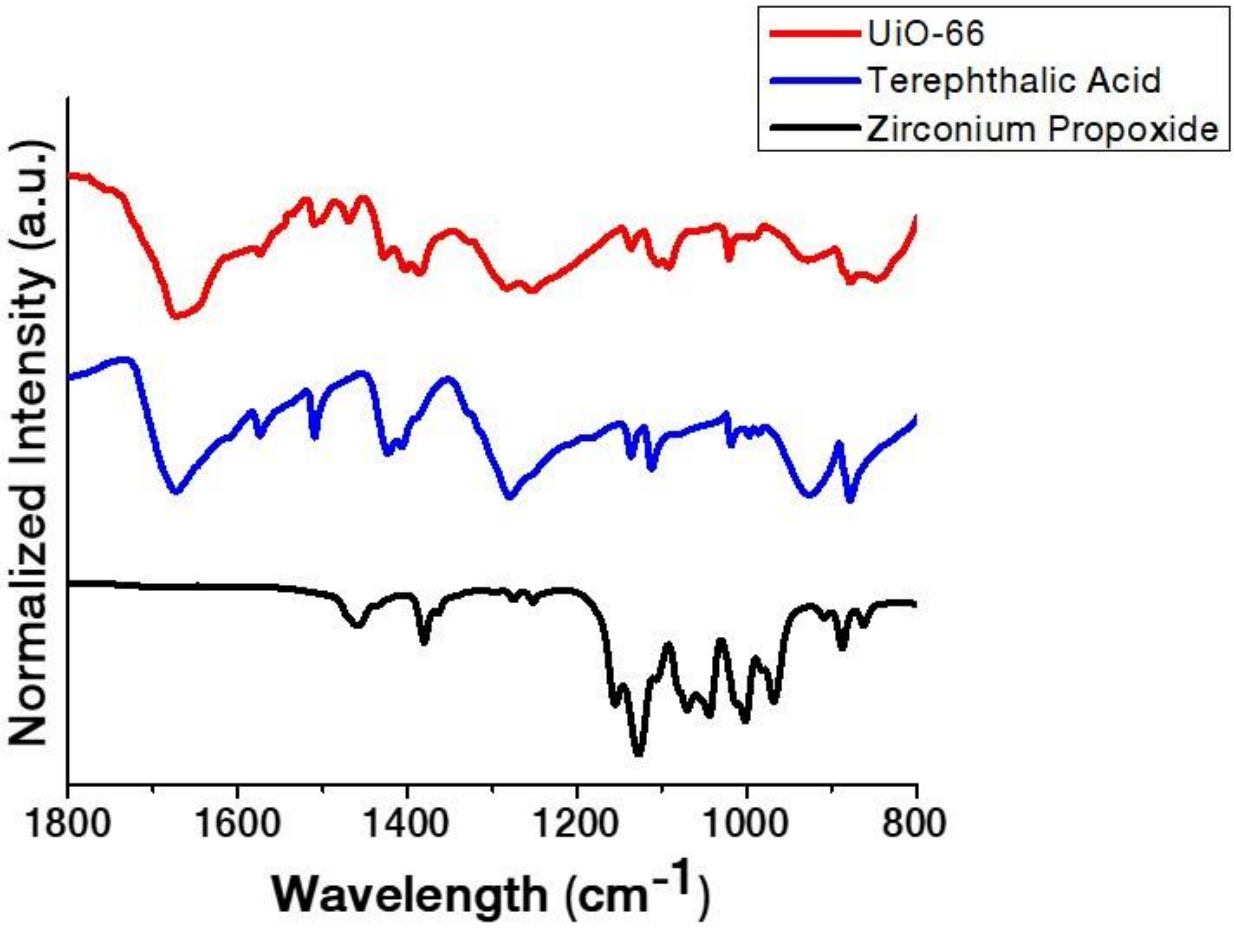

Figure A4. 1. FT-IR spectra of UiO-66 and its reactant.

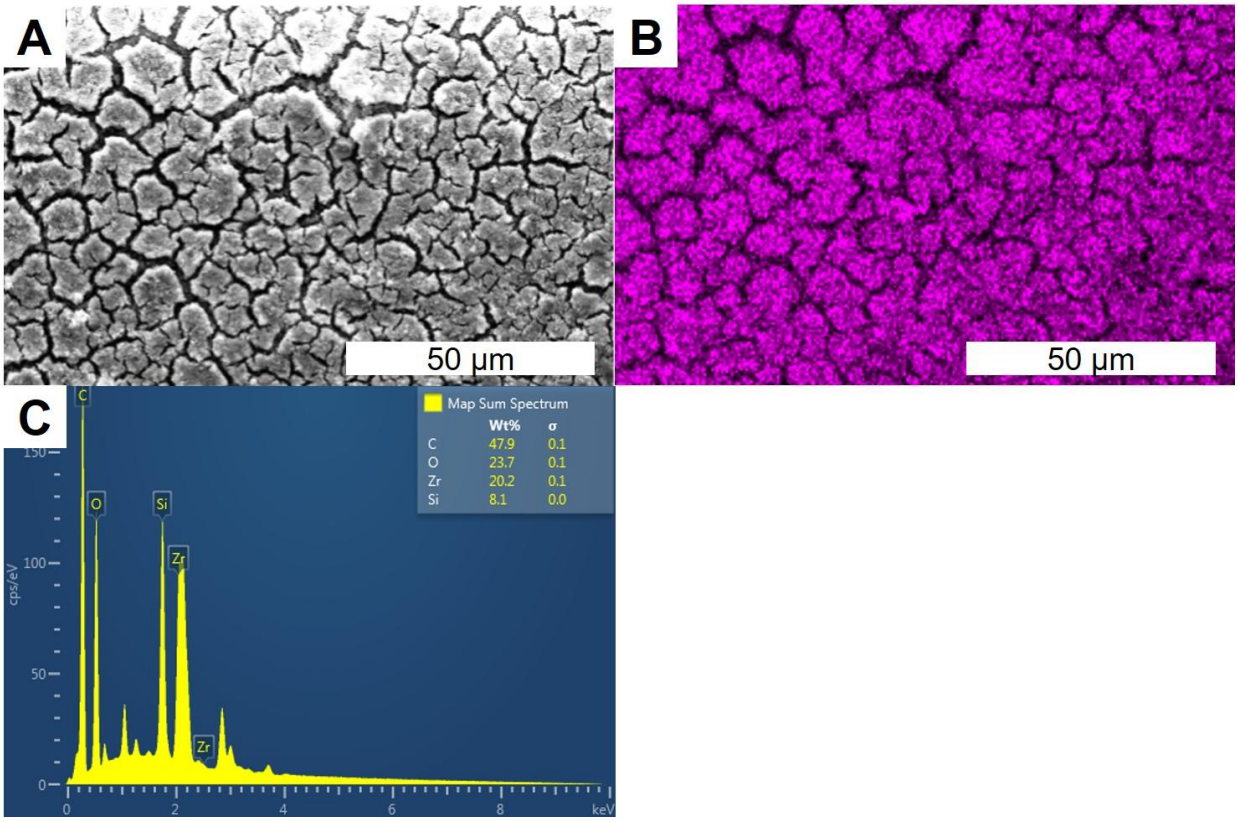

Figure A4. 2. (A) SEM image of UiO-66 thin film. **(B)** Zirconium (Zr) distribution in the UiO-66 thin film. **(C)** The elemental composition of the thin film.

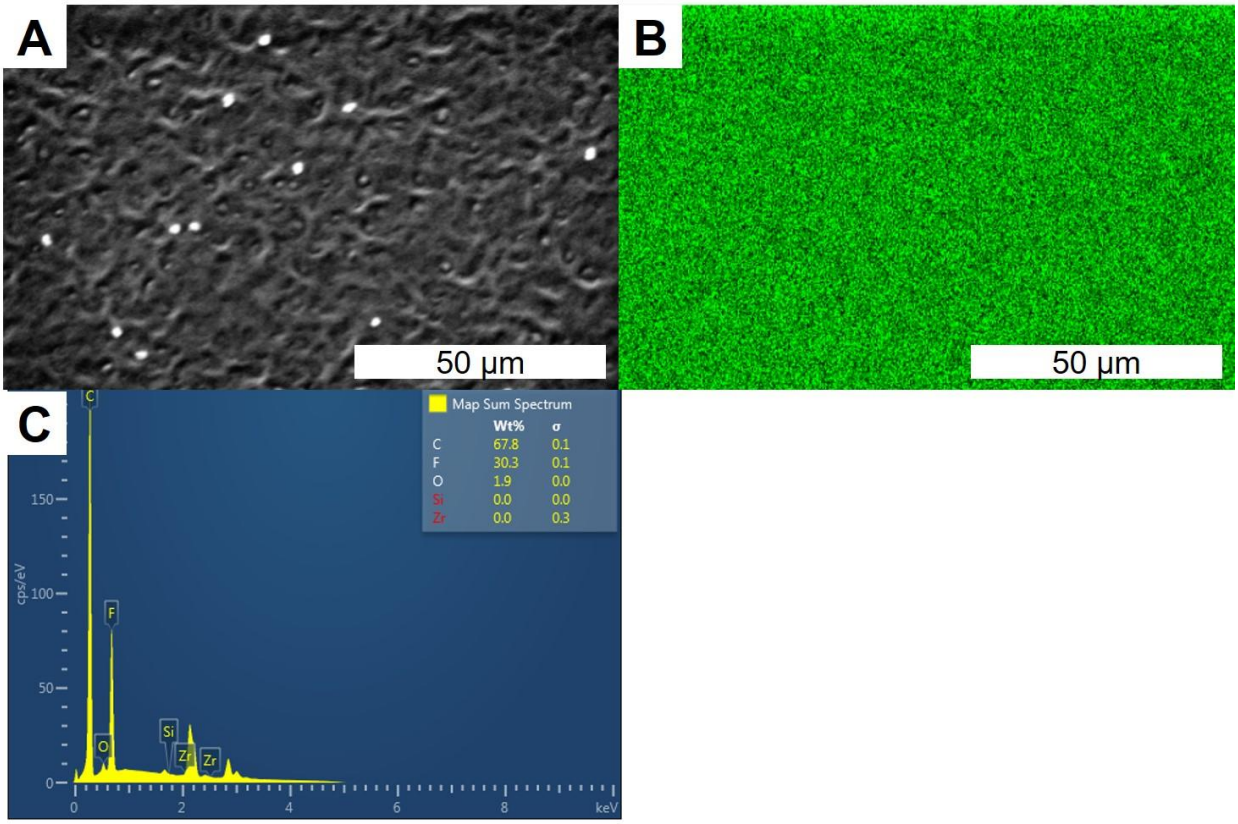

Figure A4. 3. (A) SEM image of PVDF thin film. **(B)** Fluorine (F) distribution in the PVDF thin film. **(C)** The elemental composition of the thin film.

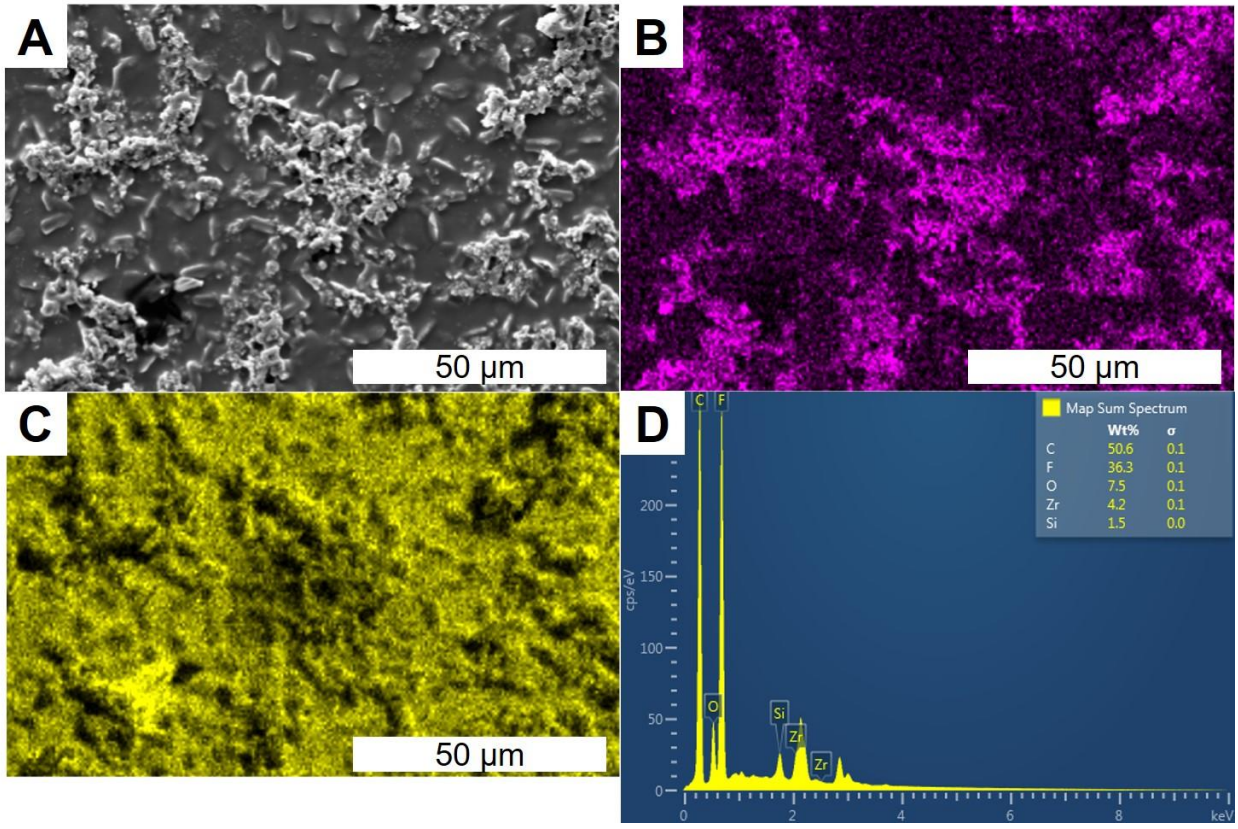

Figure A4. 4. (A) SEM image of 18 wt.% UiO-66 in PVDF@UiO-66. **(B)** Zirconium (Zr) and **(C)** fluorine (F) distribution in the PVDF@UiO-66 thin film. **(D)** The elemental composition of the thin film.

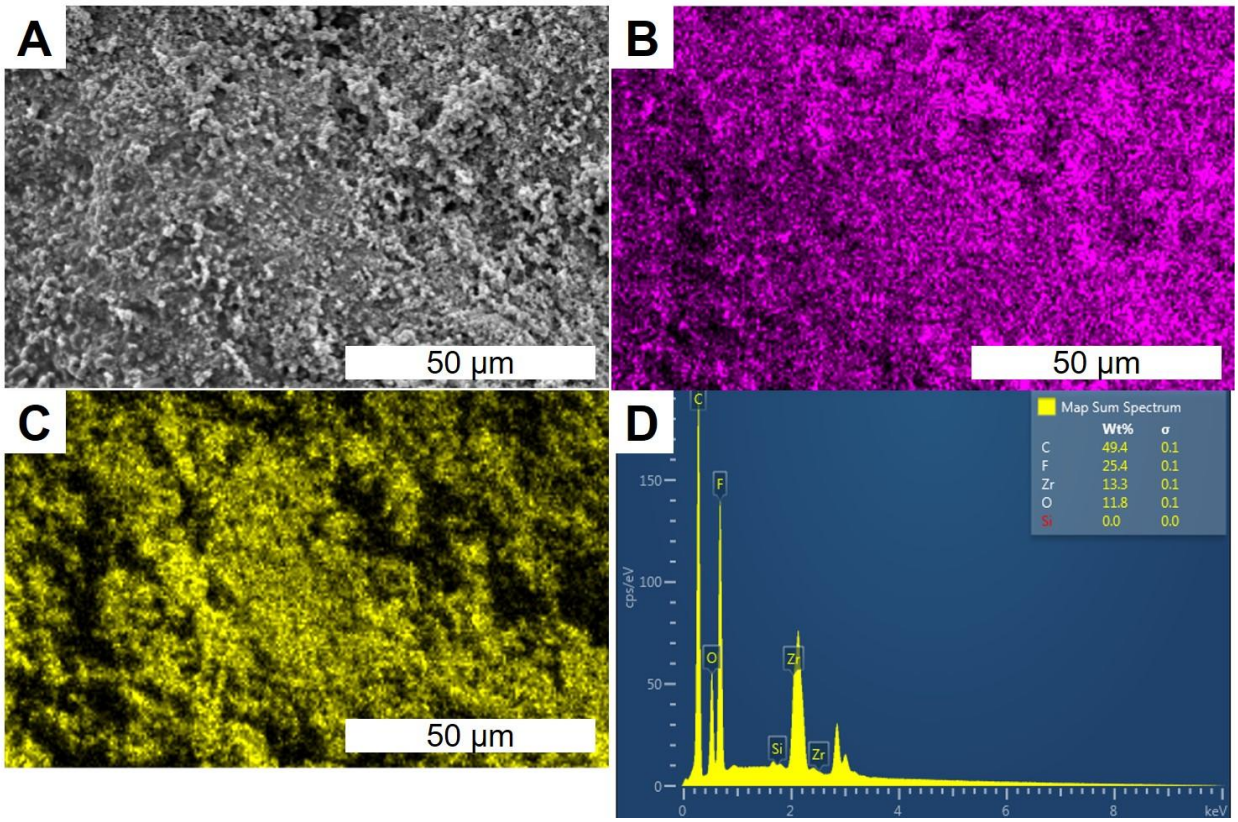

Figure A4. 5. (A) SEM image of 31 wt.% UiO-66 in PVDF@UiO-66. **(B)** Zirconium (Zr) and **(C)** fluorine (F) distribution in the PVDF@UiO-66 thin film. **(D)** The elemental composition of the thin film.

4.8 References

(1) Kim, H. K.; Yun, W. S.; Kim, M.-B.; Kim, J. Y.; Bae, Y.-S.; Lee, J.; Jeong, N. C. A Chemical Route to Activation of Open Metal Sites in the Copper-Based Metal–Organic Framework Materials HKUST-1 and Cu-MOF-2. *J. Am. Chem. Soc.* **2015**, *137* (31), 10009–10015. https://doi.org/10.1021/jacs.5b06637.

(2) Talin, A. A.; Centrone, A.; Ford, A. C.; Foster, M. E.; Stavila, V.; Haney, P.; Kinney, R. A.; Szalai, V.; El Gabaly, F.; Yoon, H. P.; Léonard, F.; Allendorf, M. D. Tunable Electrical Conductivity in Metal-Organic Framework Thin-Film Devices. *Science* **2014**, *343* (6166), 66–69. https://doi.org/10.1126/science.1246738.

(3) Schneider, C.; Mendt, M.; Pöppl, A.; Crocellà, V.; Fischer, R. A. Scrutinizing the Pore Chemistry and the Importance of Cu(I) Defects in TCNQ-Loaded $Cu_3(BTC)_2$ by a Multitechnique Spectroscopic Approach. *ACS Appl. Mater. Interfaces* **2020**, *12* (1), 1024–1035. https://doi.org/10.1021/acsami.9b16663.

(4) Hermann, D.; Emerich, H.; Lepski, R.; Schaniel, D.; Ruschewitz, U. Metal–Organic Frameworks as Hosts for Photochromic Guest Molecules. *Inorg. Chem.* **2013**, *52* (5), 2744–2749. https://doi.org/10.1021/ic302856b.

(5) Kitao, T.; Zhang, Y.; Kitagawa, S.; Wang, B.; Uemura, T. Hybridization of MOFs and Polymers. *Chem. Soc. Rev.* **2017**, *46* (11), 3108–3133. https://doi.org/10.1039/C7CS00041C.

(6) Guo, Y.; Ying, Y.; Mao, Y.; Peng, X.; Chen, B. Polystyrene Sulfonate Threaded through a Metal–Organic Framework Membrane for Fast and Selective Lithium-Ion Separation. *Angew. Chem. Int. Ed.* **2016**, *55* (48), 15120–15124. https://doi.org/10.1002/anie.201607329.

(7) Shanahan, J.; Kissel, D. S.; Sullivan, E. PANI@UiO-66 and PANI@UiO-66-NH2 Polymer-MOF Hybrid Composites as Tunable Semiconducting Materials. *ACS Omega* **2020**, *5* (12), 6395–6404. https://doi.org/10.1021/acsomega.9b03834.

(8) Kitao, T.; Bracco, S.; Comotti, A.; Sozzani, P.; Naito, M.; Seki, S.; Uemura, T.; Kitagawa, S. Confinement of Single Polysilane Chains in Coordination Nanospaces. *J. Am. Chem. Soc.* **2015**, *137* (15), 5231–5238. https://doi.org/10.1021/jacs.5b02215.

(9) Moghadam, B. H.; Hasanzadeh, M.; Simchi, A. Self-Powered Wearable Piezoelectric Sensors Based on Polymer Nanofiber–Metal–Organic Framework Nanoparticle Composites for Arterial Pulse Monitoring. *ACS Appl. Nano Mater.* **2020**, *3* (9), 8742–8752. https://doi.org/10.1021/acsanm.0c01551.

(10) Lu, A. X.; McEntee, M.; Browe, M. A.; Hall, M. G.; DeCoste, J. B.; Peterson, G. W. MOFabric: Electrospun Nanofiber Mats from PVDF/UiO-66-NH2 for Chemical Protection and Decontamination. *ACS Appl. Mater. Interfaces* **2017**, *9* (15), 13632–13636. https://doi.org/10.1021/acsami.7b01621.

(11) Li, Z.; Guo, Y.; Wang, X.; Ying, W.; Chen, D.; Ma, X.; Zhao, X.; Peng, X. Highly Conductive PEDOT:PSS Threaded HKUST-1 Thin Films. *Chem. Commun.* **2018**, *54* (98), 13865–13868. https://doi.org/10.1039/C8CC07591C.

(12) Worfolk, B. J.; Andrews, S. C.; Park, S.; Reinspach, J.; Liu, N.; Toney, M. F.; Mannsfeld, S. C. B.; Bao, Z. Ultrahigh Electrical Conductivity in Solution-Sheared Polymeric Transparent Films. *Proc. Natl. Acad. Sci.* **2015**, *112* (46), 14138–14143. https://doi.org/10.1073/pnas.1509958112.

(13) Park, S.; Pitner, G.; Giri, G.; Koo, J. H.; Park, J.; Kim, K.; Wang, H.; Sinclair, R.; Wong, H.-S. P.; Bao, Z. Large-Area Assembly of Densely Aligned Single-Walled Carbon Nanotubes Using Solution Shearing and Their Application to Field-Effect Transistors. *Adv. Mater.* **2015**, *27* (16), 2656–2662. https://doi.org/10.1002/adma.201405289.
(14) Chen, M.; Peng, B.; Huang, S.; Chan, P. K. L. Understanding the Meniscus-Guided Coating Parameters in Organic Field-Effect-Transistor Fabrications. *Adv. Funct. Mater.* **2020**, *30* (1), 1905963. https://doi.org/10.1002/adfm.201905963.
(15) Lee, J.-C.; Kim, J.-O.; Lee, H.-J.; Shin, B.; Park, S. Meniscus-Guided Control of Supersaturation for the Crystallization of High Quality Metal Organic Framework Thin Films. *Chem. Mater.* **2019**, *31* (18), 7377–7385. https://doi.org/10.1021/acs.chemmater.9b01996.
(16) Ghorbanpour, A.; Huelsenbeck, L. D.; Smilgies, D.-M.; Giri, G. Oriented UiO-66 Thin Films through Solution Shearing. *CrystEngComm* **2018**, *20* (3), 294–300. https://doi.org/10.1039/C7CE01801K.
(17) Jung, S.; Huelsenbeck, L.; Hu, Q.; Robinson, S.; Giri, G. Conductive, Large-Area, and Continuous 7,7,8,8-Tetracyanoquinodimethane@HKUST-1 Thin Films Fabricated Using Solution Shearing. *ACS Appl. Mater. Interfaces* **2021**, *13* (8), 10202–10209. https://doi.org/10.1021/acsami.1c00640.
(18) Cai, X.; Lei, T.; Sun, D.; Lin, L. A Critical Analysis of the α, β and γ Phases in Poly(Vinylidene Fluoride) Using FTIR. *RSC Adv.* **2017**, *7* (25), 15382–15389. https://doi.org/10.1039/C7RA01267E.
(19) DeStefano, M. R.; Islamoglu, T.; Garibay, S. J.; Hupp, J. T.; Farha, O. K. Room-Temperature Synthesis of UiO-66 and Thermal Modulation of Densities of Defect Sites. *Chem. Mater.* **2017**, *29* (3), 1357–1361. https://doi.org/10.1021/acs.chemmater.6b05115.
(20) Lu, A. X.; McEntee, M.; Browe, M. A.; Hall, M. G.; DeCoste, J. B.; Peterson, G. W. MOFabric: Electrospun Nanofiber Mats from PVDF/UiO-66-NH_2 for Chemical Protection and Decontamination. *ACS Appl. Mater. Interfaces* **2017**, *9* (15), 13632–13636. https://doi.org/10.1021/acsami.7b01621.
(21) Abdullah, I. Y.; Jumali, M. H. H.; Yahaya, M.; Shanshool, M. Facile Formation of β Poly (Vinylidene Fluoride) Films Using the Short Time Annealing Process. **2015**, 9.

5 Conclusion and Future Work

The pore utilization of MOF thin film using solution shearing is discussed as the fabrication of the high-quality MOF thin film in a rapid time scale is necessary for applying MOF thin films into a wide range of applications. In this dissertation, we have approached to explore the feasibility of large-area and continuous MOF thin films using solution shearing and the incorporation of either redox-active or polymer molecules into the pores. Therefore, we synthesized two well-known MOF thin films (HKUST-1 and UiO-66) using solution shearing and incorporated either 7,7,8,8-Tetracyanoquinodimethane (TCNQ) or poly(vinyl difluoride) (PVDF) so that the application of MOF thin films can be extended such as a chemi-resistive sensor or flexible membrane.

5.1 Fabrication of Large-area and continuous TCNQ@HKUST-1 thin film using solution shearing

In Chapter 2, solution shearing is used to fabricate a large area and continuous HKUST-1 thin film using solution shearing. The film coverage was determined by varying multiple solution shearing parameters. However, it was limited to fabricating a continuous thin film using one cycle of solution shearing. Thus, multiple solution shearing cycles were performed so that the initial solution shearing cycle was regarded as the deposition of HKUST-1 seed crystals and subsequent solution shearing cycles were induced the secondary crystallization, enhancing film coverage. To confirm the continuous film coverage, a redox-active molecule, called TCNQ, was incorporated along with the HKUST-1 crystals, leading to form a TCNQ@HKUST-1 composite. Since the electrical conductivity of the pristine HKUST-1 thin film is insulating, impregnation of TCNQ into HKUST-1 pores increases the electrical conductivity of HKUST-1 thin film. Therefore, seven orders of magnitude of electrical

conductivity were increased after TCNQ formed coordination bonding with HKUST-1 thin film. Future work could explore the feasibility that the TCNQ@HKUST-1 thin film could be fabricated by directly adding TCNQ molecules into the precursor solution of HKUST-1.

5.2 Exploration of the solution sheared Zr-based MOF thin film crystallization

In Chapter 3, we have shown the crystallization of the zirconium-based MOF, UiO-66, thin film using solution shearing. Multiple solution shearing parameters (substrate temperature, coating blade speed, precursor solution concentration, type of solvent, and the number of cycles) were varied to observe the effect of crystallinity, coverage, and thickness. Furthermore, we demonstrated that using dimethylformamide as a solvent enhances the orientation of the UiO-66 crystals on the substrate. For the future, solution sheared UiO-66 will be tested its separation ability against the particulate matters on the porous substrate such as anodic alumina oxide (AAO) so that the application of the large-area and continuous UiO-66 thin film can be explored.

5.3 Polymer incorporation into the solution sheared Zr-based MOF thin film

Chapter 4 demonstrated the characterization of polyMOF, which is the combination between poly(vinyl difluoride) (PVDF) and UiO-66, as a thin film that is fabricated by using solution shearing. Compared to the conventional polyMOF synthesis, PVDF is pre-mixed with the precursor solution of UiO-66 and deposited as a thin film using solution shearing. This leads to reducing the synthetic time of the polyMOF significantly. Since solution shearing was used to fabricate large-area and continuous thin film, the thin film properties, including crystallinity, coverage and thickness can also be controlled. Furthermore, polyMOF contains

both properties of polymer and MOF, so that flexible, free-standing large-area and continuous polyMOF thin film is grown on the substrate. In the future, the correlation between the changes in thermal conductivity and piezoelectricity upon polymer incorporation will be explored. Moghadam et al.[1] show that the piezoelectricity of PVDF@UiO-66 is higher than that of PVDF, itself. Since the hydrogen bonding is formed between PVDF and organic linkers, the probability of β-phase formation of PVDF increases. In addition, according to DeCoster et al.[2], the thermal conductivity of HKUST-1 can be controlled by filling up pores with the guest molecules, such as TCNQ, F_4-TCNQ, and H_4-TCNQ. Depending upon the changes in electrical conductivity that comes from the guest-host interaction, the thermal conductivity decreases by a factor of 4 upon the infiltration with guest molecules. However, to the best of our knowledge, no studies have been performed that describe the relationship between piezoelectricity and thermal conductivity in the PVDF@UiO-66 system. Therefore, depending upon the weight percentage of PVDF inside the polyMOF, the changes in piezoelectricity with respect to the temperature of the thin film will be explored.

5.4 Final Remarks

The work presented here is intended to show the utilization of solution shearing as one of the MOF thin film fabrication techniques. Compared to the number of new MOFs that are discovered, their corresponding applications are still at an early stage. In this dissertation, we have shown the possibility that scalable and high-quality MOF thin film can be fabricated using solution shearing. With the continuous development of the solution shearing, the application of scalable and high-quality MOF thin films can be explored.

5.5 References

(1) Moghadam, B. H.; Hasanzadeh, M.; Simchi, A. Self-Powered Wearable Piezoelectric Sensors Based on Polymer Nanofiber–Metal–Organic Framework Nanoparticle Composites for Arterial Pulse Monitoring. *ACS Appl. Nano Mater.* **2020**, *3* (9), 8742–8752. https://doi.org/10.1021/acsanm.0c01551.

(2) DeCoster, M. E.; Babaei, H.; Jung, S. S.; Hassan, Z. M.; Gaskins, J. T.; Giri, A.; Tiernan, E. M.; Tomko, J. A.; Baumgart, H.; Norris, P. M.; McGaughey, A. J. H.; Wilmer, C. E.; Redel, E.; Giri, G.; Hopkins, P. E. Hybridization from Guest–Host Interactions Reduces the Thermal Conductivity of Metal–Organic Frameworks. *J. Am. Chem. Soc.* **2022**, jacs.1c12545. https://doi.org/10.1021/jacs.1c12545.